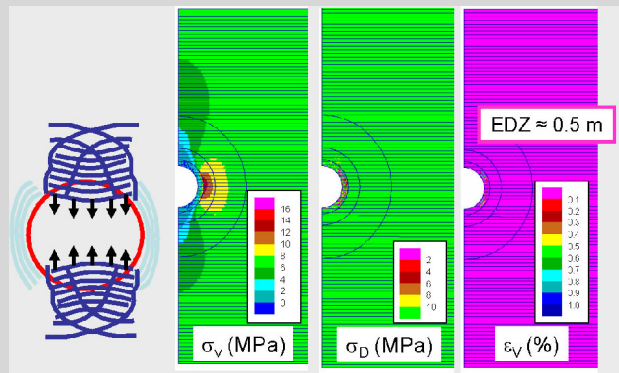


Untersuchung der komplexen mechanischen und hydraulischen Eigenschaften von Tongesteinen unter besonderer Berücksichtigung der Foliation

Ergebnisbericht zum
BMBF-Forschungsvorhaben
02 E 9874



Institut
für
Gebirgsmechanik
GmbH

Kurzfassung

Tonformationen werden aktuell neben anderen Gesteinen bezüglich ihrer Eignung zur Errichtung eines Endlagers für radioaktive Abfälle zur Vermeidung einer daraus resultierenden Gefährdung untersucht. Da die Transporteigenschaften des Tons letztlich die Barrierenintegrität bestimmen, ist bei geschichteten Tonsteinen insbesondere der Einfluss von Schichtflächen zu berücksichtigen, da diese als hydraulische Wegsamkeiten und mechanische Schwächeflächen wirken können. Bezogen auf diese zwei Themenkomplexe, wurden im Rahmen dieses Projektes umfangreiche Laboruntersuchungen und, darauf basierend, numerische Modellrechnungen durchgeführt.

Die in diesem Bericht vorgestellten Untersuchungen wurden sowohl von der Europäischen Kommission im Rahmen des internationalen 6. EU-Rahmenprogramms (2002-2006) als auch vom Bundesministerium für Bildung und Forschung (BMBF) unter dem Förderkennzeichen 02 E 9874 gefördert.

Der Laborteil beinhaltet die Durchführung und Auswertung von Verformungsexperimenten in einer "echt-drei-axialen" Verformungsapparatur und einer konventionellen triaxialen Kármán-Zelle. Dabei wurden für einen relevanten Verformungsbe- reich wichtige Informationen zur Ausbildung von Schädigung mittels der gleichzeitigen Messung der Ultraschallgeschwindigkeiten (V_p , V_s), der Gas-Permeabilität und der Volumenverformung erhalten. Zusätzlich wurde die Scherfestigkeit und die dabei entstehende Aufweitung von Rissflächen mittels eines direkten Schergeräts bestimmt.

Die experimentellen Ergebnisse liefern eine umfangreiche Datenbasis zur Ableitung von Modellparametern zur numerischen Modellierung. Davon ausgehend wurde abschließend ein neuer Modellansatz, u. a. zur Beschreibung der Ausbildung der ALZ, entwickelt, der auf einer getrennten Beschreibung der Matrix- und Schichtflächeneigenschaften mittels am IfG entwickelter Stoffgesetze basiert. Die Leistungsfähigkeit dieses neuen Ansatzes wurde durch Rückrechnung der ALZ-Entwicklung um eine kreisförmige Strecke am Standort Mont Terri (CH) demonst-riert, wobei sowohl die phänomenologischen Rissstrukturen (Zugrisse in der Firste bzw. Schichtflächenversagen am Stoss) wie auch die Ausdehnung der ALZ abge- bildet wurden.

Die Verantwortung für den Inhalt dieser Veröffentlichung liegt bei den Autoren.



NF-PRO

(Contract Number: F16W-CT-2003-02389)

WP 4.2

- EDZ Initial phase characterization and modelling -

Influence of bedding planes (IfG)

FINAL REPORT

Deliverable D4.2.15

Author(s): Till Popp, Klaus Salzer (IfG)

Reporting period: 01/01/05 – 31/12/07

Date of issue of this report: **01/10/07**

Start date of project: **01/01/04**

Duration: 48 Months

Project co-funded by the European Commission under the Euratom Research and Training Programme on Nuclear Energy within the Sixth Framework Programme (2002-2006)

Dissemination Level

PU	Public	
RE	Restricted to a group specified by the partners of the NF-PRO	
CO	Confidential, only for partners of the NF-PRO project	

DISTRIBUTION LIST

Name	Number of copies	Comments

Table of Contents

1	INTRODUCTION	5
2	DILATANCY CHARACTERISATION IN A MULTI-ANVIL APPARATUS	8
2.1	INTRODUCTION – LAB INVESTIGATION TOOLS FOR QUANTIFYING DILATANCY	8
2.2	MATERIAL ORIGIN / TEST DEVICE	11
2.2.1	<i>Material description and rock fabric</i>	<i>12</i>
2.2.2	<i>Test device and procedure</i>	<i>14</i>
2.3	EXPERIMENTAL RESULTS	15
2.3.1	<i>Hydrostatic loading</i>	<i>15</i>
2.3.2	<i>Deviatoric loading / evaluation of strength data</i>	<i>17</i>
2.3.3	<i>Crack patterns</i>	<i>22</i>
2.3.4	<i>Discussion</i>	<i>22</i>
3	COUPLED HYDRAULICAL AND MECHANICAL PROPERTIES DURING TRIAXIAL LOADING	23
3.1	INTRODUCTION	23
3.1.1	<i>Sampling and preparation of cylindrical clay samples</i>	<i>23</i>
3.1.2	<i>Triaxial pressure device – volumetric strain measurement</i>	<i>24</i>
3.1.3	<i>Simultaneous measurements of ultrasonic wave velocities and gas-permeability</i>	<i>25</i>
3.2	EXPERIMENTAL RESULTS	27
3.2.1	<i>Gas injection tests at various compaction states</i>	<i>27</i>
3.2.2	<i>Hydrostatic loading</i>	<i>32</i>
3.2.3	<i>Deviatoric loading</i>	<i>34</i>
3.3	EVALUATION OF THE PERMEABILITY / POROSITY RELATIONSHIP	38
3.4	EVALUATION OF THE STRENGTH DATA	39
3.5	EVALUATION OF THE DEFORMATION INDUCED-VELOCITY CHANGES	40
3.6	APPLICATION OF THE DILATANCY CONCEPT IN ARGILLACEOUS CLAY - DISCUSSION.....	42
4	DIRECT SHEAR TESTS ON BEDDING PLANES.....	44
4.1	TEST ARRANGEMENT.....	44
4.2	EXPERIMENTAL RESULTS	46
4.3	EVALUATION OF SHEAR TEST RESULTS.....	49
4.3.1	<i>The Minkley-shear model</i>	<i>51</i>
4.3.2	<i>Application to shear strength of bedding planes.....</i>	<i>54</i>

5	MODELLING	56
5.1	OBJECTIVES AND MODELING CONCEPT	56
5.2	THE (VISCO-)ELASTO-PLASTIC CONSTITUTIVE MINKLEY-MODEL – DERIVATION OF PARAMETERS	58
5.3	APPLICATION.....	61
5.3.1	<i>Model assumptions and parameters</i>	61
5.3.2	<i>Main results from the preliminary model</i>	63
5.3.3	<i>Summary</i>	65
6	CONCLUSIONS	66
6.1	INITIAL SAMPLE STATE AND TRANSPORT PROPERTIES.....	66
6.2	DEFORMATION BEHAVIOUR AND DILATANCY BOUNDARY CONCEPT:	67
6.3	MODELLING OF FAILURE MODES AND EDZ-STRUCTURES:.....	67
	LITERATURE	68

1 Introduction

In the assessment of a multi-barrier system the geological and hydrogeological features of the repository site are crucial as the safe confinement of the radioactive waste and its isolation from the biosphere has to be guaranteed for a period of up to one million years. Due to their favourable transport and geochemical properties different argillaceous rocks are being under investigation as potential host rock formations for an underground repository, e.g. the Opalinus Clay as an indurated clay in the Swiss waste disposal program.

Mining of underground galleries and cavities generally results in development of an excavation disturbed/damaged zone (EDZ), which affects the efficiency of geological barrier systems at least while operation and closing phases. Concerning the EDZ evolution in argillaceous rocks and their fundamental understanding in both, field and laboratory investigations, an extensive knowledge is available due to longstanding investigation. However, a prognosis of the EDZ initiated by mining activities is only possible if suitable material laws are evolved corresponding to respective host rock that allow a numerical simulation of the complex hydro-mechanical behaviour of the surrounding host rocks associated with the contrasting processes of brittle deformation and healing while operating the repository. Therefore, the basic demands for sufficient realistic numerical simulations are identification, understanding and quantitative description of the main geomechanical and hydraulic mechanisms and processes.

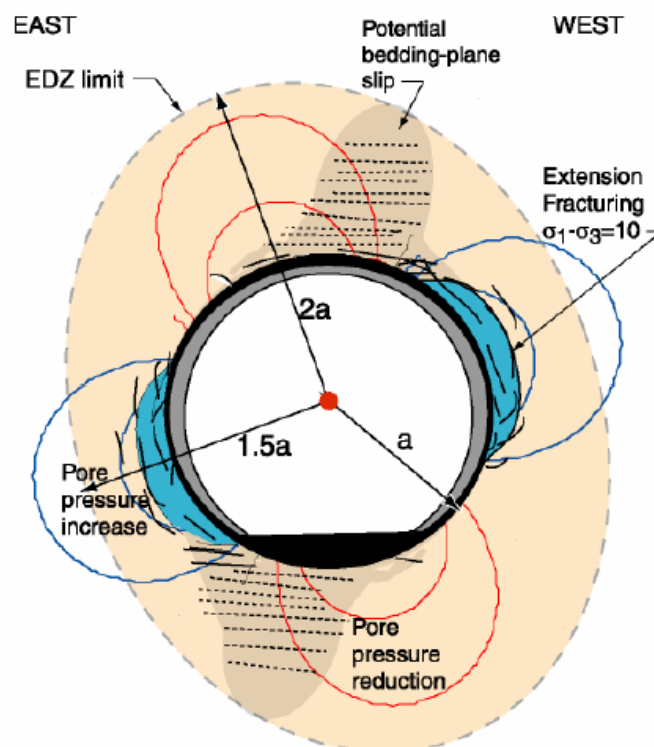


Figure 1-1. Summary of the extent of the EDZ around the New gallery at Mont Terri (taken from MARTIN et al., 2003).

With respect of interpreting the rock mechanical and related hydraulical properties it has to be taken into account that in contrast to other rocks (e.g. salt or granite) argillaceous rocks are inherently anisotropic, namely, transversely isotropic in their strength, stress-strain relations, dilatancy characteristics, and their failure patterns due to the developed bedding during sedimentary and tectonical history.

The causal bedding plane anisotropy is achieved by both macroscopic and microscopic layering of clay minerals or lithologically different rock units (e.g. sand-shale sequences). In a micro-structural scale anisotropy of indurated clay deposits is considered to be divided into two components, namely, inherent fabric anisotropy due to preferred mineral orientation (LPO) and intensified by pore space effects or micro cracking, which all may be stress and pore pressure affected during excavation.

As a consequence initiation of inelastic deformation and the relative dilatation are clearly a function of bedding plane properties and the spatial stress geometry. In addition, bedding planes can act as preferential flow paths. These overlapping effects are particularly important during rock stress redistribution in the EDZ.

Thus, it can be anticipated that experimental studies following a material science approach are essential, combining appropriate laboratory experiments with numerical modelling to enlarge the scale of investigation. Amongst others, this laboratory study will focus on the impact of mechanical properties of argillaceous rocks on the transport properties with respect to the bedding plane. Supplementary, mineralogical investigations of the rock structure are being performed to understand the influence of the textural sample characteristics.

The work done by IfG is allocated to the following three tasks subdivided to the applied methods and investigated parameters:

(1) *EDZ characterization in the lab - How is dilatancy created and controlled?*

- ⇒ In general, is the “dilatancy concept” in indurated clay applicable?
 - Short-term strength behaviour of Opalinus clay
 - Shear strength of Opalinus Clay

In the lab the amount of brittle deformation of rocks is generally described by the parameter dilatancy, i.e. the development of micro-fractures, which depends on the state of stress (stress field geometry and deviator). The determination of the stress dependent onset of dilatancy, described by the criteria dilatancy boundary, is, therefore, of predominant importance for an appraisal of barrier properties of solid rocks. Here, we present results obtained with two different experimental setups, i.e. a multi-anvil apparatus and a conventional triaxial Kármán cell, that both allow detection of onset microcracking by monitoring ultrasonic wave velocities.

In addition, because underground observations in clay formations (e.g. Mont Terri) clearly indicate that shear failure parallel to the bedding is an important feature direct shear tests were performed on large sample blocks (of approx. 100 mm x 100 mm x 200 mm). The obtained experimental results cover a wide range of applied confining respectively normal

stresses and displacement rates and delivered a reliable estimate of rock mechanical properties (i.e. strength and dilatancy angle).

(2) Relationship between transport properties and dilatancy in Opalinus Clay?

- ⇒ Coupling hydro-mechanical properties (HM-properties)
 - Permeability/ porosity relationship
 - Gas-pressure induced dilatancy
 - Sealing / (Healing)

Since the transport properties of argillaceous rocks are responsible for the demanded integrity, knowledge of the relationship between the development of damage (dilatancy) and hydraulic properties is of utmost importance.

(3) Mechanical modelling of EDZ properties – How are to handle both matrix and bedding plane properties with respect to a prognosis of the EDZ evolution?

- ⇒ Development of an alternative modelling concept of excavations in bedded clay formations
 - Evaluation of the model-parameters from strength and shear tests
 - 2D-modeling of the excavation of a gallery

Based on the experimental data base a new modelling approach has been developed consisting of two parts, i.e. of a (visco-)elasto-plastic constitutive model comprising the hardening/softening behaviour and dilatancy effects of the rock mass and a specific shear friction model, which describes displacement- and velocity-dependent shear strength softening for the bedding planes. Its usability is demonstrated simulating a simple 2D-drift situation at the Mont Terri site.

During the course of the 4-years NF-PRO-duration preliminary lab test results were already reported in three deliverables focusing on the following issues:

D4.2.2 (IFG, 2005a): Interims Report 1: State of the art report / Test plan for shear testing (2005-01-15).

D4.2.6 (IFG, 2005b): Interims Report 2: First results of shear tests (laboratory tests) (2005-01-15).

D4.2.8 (IFG, 2006): Interims Report 3. Interim report on results on shear tests / Triaxial compression tests (2006-02-10).

In addition, partial results were presented at the following meetings respectively published:

POPP, T. & K. SALZER, 2005. Anisotropy of seismic and mechanical properties of Opalinus clay during triaxial and shear deformation. 2nd International meeting "Clays in Natural & Engineered Barriers for Radioactive Waste Confinement", Tours, 14-18 March 2005, P/THMN/03, Poster.

POPP, T. & K. SALZER, 2006. Investigation of the influence of bedding planes to coupled HM properties of the damaged rock. Third NFPRO-Workshop, El Escorial, Spain, Nov 14-16 2006. Poster.

POPP, T. & K. SALZER, 2007. Anisotropy of seismic and mechanical properties of Opalinus clay during triaxial deformation in a multi-anvil apparatus. Physics and Chemistry of the Earth, 32, 879-888.

2 Dilatancy characterisation in a multi-anvil apparatus

2.1 Introduction – lab investigation tools for quantifying dilatancy

The determination of the dilatancy respectively damage boundary is of predominant importance for an appraisal of barrier properties of solid rocks. Generally, the amount of dilatancy describes the intensity of brittle deformation of rocks, i.e. the generation of micro-fractures. Such processes – resulting in the development of an EDZ – are immediately connected to mining activities.

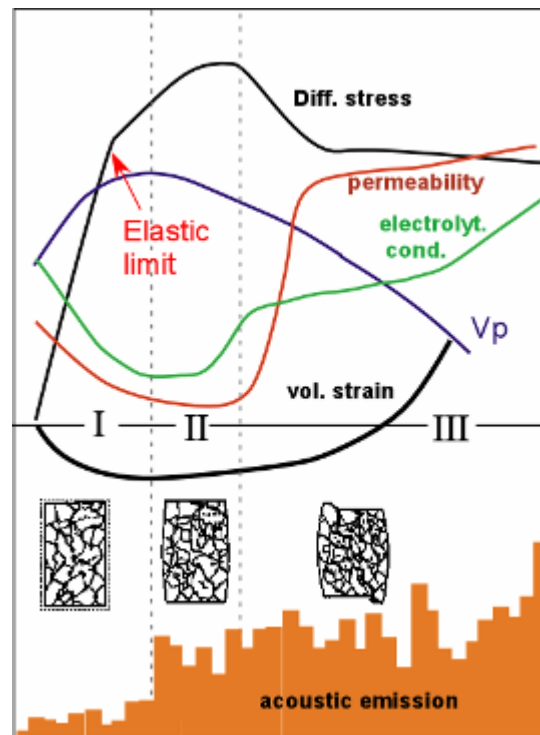


Figure 2-1. Schematics illustrating changes of physical properties during deformation. Volume change, acoustic emission, permeability, and ultrasonic wave velocity are used to monitor dilatancy (modified after SCHULZE et al., 2001).

Therefore, in particular, the influence of dilatancy on the mechanical and hydraulical properties must be known for the design of safe excavations in deep underground and for the assessment of the long-term integrity of the rock surrounding a repository.

As a basis for a successful attempt investigating experimentally such complex relationships Figure 2-1 compiles property changes of a hypothetical rock during strength testing ($\dot{\epsilon} = \text{const.}$) in a synoptic diagram:

- Stage 1 appears essentially under low confining pressures and is attributed to the closing of pre-existing cracks or dilated grain boundaries. The initial elastic loading is followed by inelastic deformation whereby it remains unclear if at that stress level damage already starts.

- Exceeding a certain differential stress causes the transition from non-dilatant to dilatant behaviour. Progressive onset of dilatancy (between domains I and II in Figure 2-1) is associated with acoustic emission, increase of volumetric strain and permeability, and decrease of ultrasonic wave velocities but not simply to identify. Consequently, simultaneous monitoring of several physical parameters in relation to confining pressure and stress offers a more detailed insight into the complex coupling of transport and mechanical properties.
- Stage 3 corresponds to the post failure stage and is associated with a significant weakening respectively localized shear.

For detection and quantification of micro-fracturing due to deviatoric stresses various methods are available but relative sensitiveness of the respective measured parameters has to be taken into account, as came out by extensive laboratory investigations on salt rocks (e.g. POPP et al., 2001; SCHULZE & POPP, 2002):

- *Direct measurement of test sample volume* (e.g. ZHANG & ROTHFUCHS, 2005) or of *various strain displacements via strain gauges*, (e.g. VALES ET AL., 2004) – The minimum test sample volume which is reached while a strength test is defined as damage boundary. Due to the superimposition of deformation-relation volume increase due to microfracturing and still existing local compaction (e.g. in areas of in front of the pistons: stress shadow).
- *Measurement of permeability*, e.g. WANG & PARK (2002) – *clay rocks*; KERN & POPP (2001) - *salt rocks* – The initiation of dilatancy is detected by a measurable increase of permeability. This procedure is not useful as a standard method of dilatancy verification due to difficulties in continuous measurements at low-permeable samples. Concomitantly, stress-induced fractures have to be interconnected, i.e. local fractures can not be observed.
- *Measurement of ultrasonic wave velocities*, e.g. POPP et al. (2001) – This method is well-suitable and capable in laboratory and in-situ test to detect fractures via simultaneous determination of P- and S-wave velocities. However, the results are not directly related with pore space parameters like permeability or porosity.

Comparison of these methods results in variations regarding the stress-dependent initiation of dilatancy. Judging already existing information about onset of dilatancy in indurated clay (e.g. BLÜMLING, 2nd NFPRO-Workshop, Cardiff (GB), 2005) may indicate that better understanding of the relevance of the respectively measured parameters is necessary.

Therefore, we used two experimental approaches concerning the detection of stress dependent onset of micro-cracking respectively quantification of gas transport properties under non-hydrostatic conditions, as schematically indicated in Figure 2-2.

- **Triaxial multi-anvil apparatus:** Deformation tests on well oriented sample cubes facilitated a precise detection of the onset of micro-cracking respectively dilatancy as indicated by seismic velocity measurements in the three directions (respectively V_p , V_{s_1} and V_{s_2} for determination of shear wave splitting but represent an open system which impedes hydraulical measurements.

- **Triaxial Kármán cell:** Most results concerning the impact of bedding to coupled HM properties of the pre-dilated indurated clay samples were obtained by short term triaxial tests with simultaneous monitoring of p- and s-wave velocities supplemented by permeability and volumetric strain measurements on Opalinus clay loaded parallel and perpendicular to the bedding, whereby only one preferred measuring direction exists.

Because both experimental setups have individual pros and cons the experimental test procedures and results will be presented separately in two chapters. Firstly test results, obtained in the multi-anvil-triaxial pressure apparatus at the University of Kiel (Germany) will be reported. Here, the crack-sensitivity of ultrasonic wave velocities can be used to monitor the in-situ state of the microstructure and to identify the onset of dilatancy (e.g. POPP et al., 2001). Based on the results the so-called "dilatancy concept" respectively the reliability of the term "dilatancy" regarding its importance for the EDZ in indurated clays is discussed.

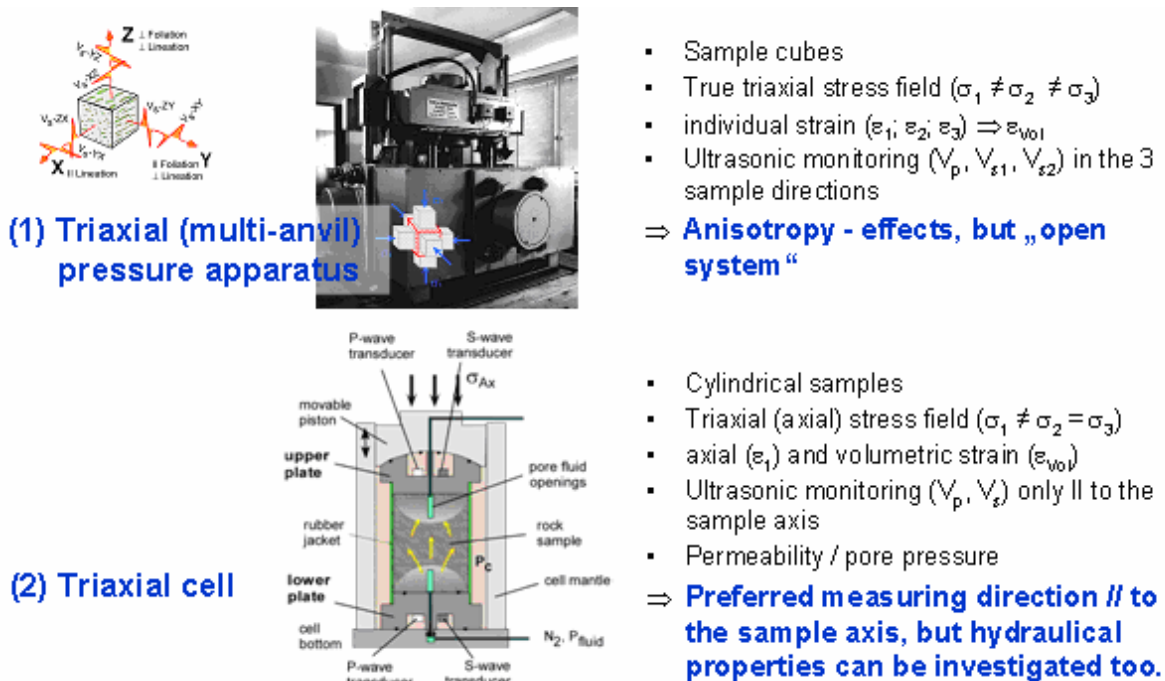


Figure 2-2. Investigation of dilatancy - two experimental setups with specific measuring capabilities of determining petrophysical properties related to respective sample geometry.

2.2 Material origin / test device

The material was recovered from two bore holes at the Mont Terri site in Switzerland: BLT 1 and BLT 2, which were drilled in January 2001 during the drilling campaign 6 of the Mont Terri project.

The underground lab is placed in the Opalinus Clay, a rock formation consisting mainly of incompetent, silty and sandy shales, deposited around 180 Ma (Aalenien). The Opalinus Clay formation can be characterised as an overconsolidated shale formation (present overburden 300 m, estimated overburden in the past at least 1000 m).

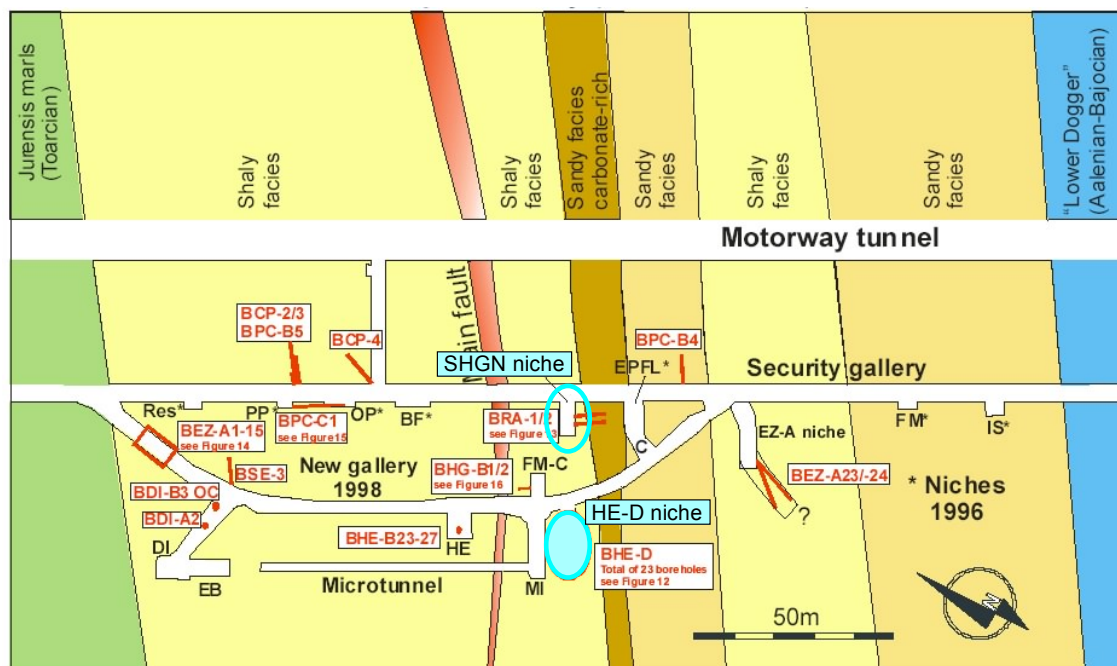


Figure 2-3. Geological map of Mont Terri rock laboratory - Opalinus Clay (Lower Aalenian). Note the positions of the sample recovery.

A simplified geologic map of the Mont Terri rock laboratory is shown in Figure 2-3. The main tectonic structure of the considered area is the Mont Terri anticline. The Opalinus Clay has a thickness of 160 m and is divided – from bottom to top – into five lithostratigraphic sub-units (e.g. MONT TERRI PROJECT, 2004):

- Sub-unit 1: 80 m of argillaceous and marly shales with micas and nodular, bioturbated layers of marls (tunnel metres 902–1024).
- Sub-unit 2: 5–10 m of calcareous sandstones intercalated with bioturbated limestone beds, the latter showing a high detrital quartz content (tunnel metres 888–902).
- Sub-unit 3: 10–15 m of marly shales with layers of sandstones and bioturbated limestones (tunnel metres 869–888).
- Sub-unit 4: 20 m of argillaceous and marly shales with mm-thick layers of sandstones (tunnel metres 835–869).

- Sub-unit 5: 40 m of marly shales with lenses of grey, sandy limestones and mm-thick layers of white sandstones with pyrite, as in the sequence below. At the top, dm layers of biogenic limestones and sandstones were found (tunnel metres 781–835).

These five Opalinus Clay sub-units can be grouped into three main facies, which are illustrated in Figure 2-3: a shaly facies (sub-units 1, 4), a sandy facies (sub-units 3, 5) and a carbonate-rich, sandy facies (sub-units 2).

The average mineral composition is given in Table 2-1.

Table 2-1. Average mineralogical composition of Opalinus Clay.

Rock (Origin)	Clay content	Clay minerals	Other minerals	Porosity / Water cont. /	Literature
	(%)	(%)	(%)	(%)	
Opalinus Clay (Mont Terri, CH)	50 - 70	15–25% illite 20–37% kaolinite 5–20% mixed layers 4-18% chlorite	4-29% calcite 0 -7.5 Siderite, dolomite, ankerite 10-27% quartz <3% accessories	~15 6 - 7	After Bock (2001)

2.2.1 Material description and rock fabric

The mouths of the sampling bore holes are located in the SHGN niche at position SG 905.54 (BLT-1: 10.10 m length) 0.97 m above bottom resp. at position SG 905.60 (BLT-2: 14.0 m length) 0.65 m above bottom. The holes with a diameter of 131 mm were horizontally drilled with a double core barrel in WSW direction (236°).

The investigated material was cored with a 101 mm diameter tungsten carbide bit and cooled with dried air. The samples were cut in the shaly facies at a distance of 2.90 - 8.40 m from the gallery to provide mechanical data of non disturbed media. All samples were sealed in aluminium coated foil.

The core samples were carefully machined with a fine band saw by the BGR staff into 11 cubic specimens of 43 mm edge length.

The bulk density of the specimens was observed to be 2438 ± 10 kg/m with a porosity of ~15% and a water content of ~6.0%. The general mineralogy of the rock is summarized in Table 2-1.

The prepared samples showed thin bedded dark grey clay minerals with a typical anisotropic texture of clay particles parallel to the bedding surface, which was created during sedimentation and tectonic induced compaction processes as schematically shown in Figure 2-4. According to the observed lithological and textural heterogeneity all measured properties have to be related to the textural framework. Foliation and lineation (if visible) provide the framework for the standard reference system of the sample cubes, as illustrated schematically in Figure 2-5 according to VALES et al. (2004):

[Z] is normal to foliation, [Y] is perpendicular to lineation within the foliation, and [X] is parallel to lineation. For the regional assignment the angle θ is defined as the angle between the bedding plane [x, y] and the vertical axis.

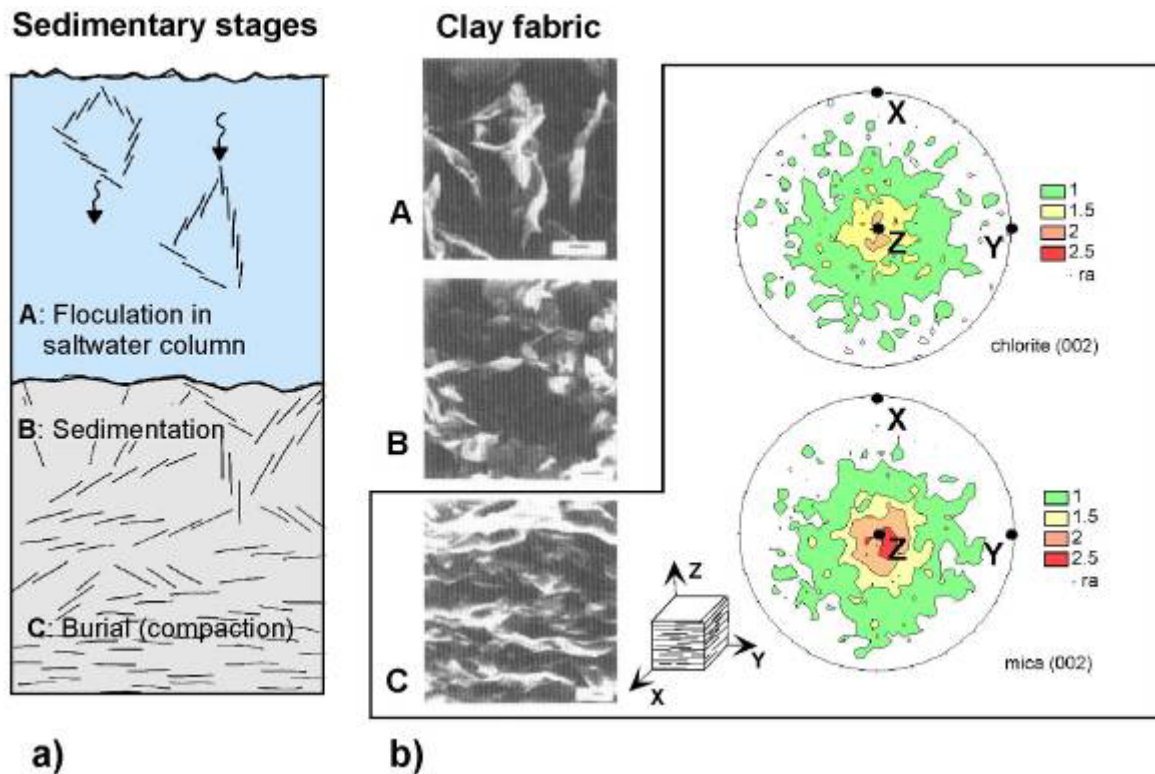


Figure 2-4. Microstructure of the Opalinus Clay. a) Texture development of a sedimentary deposited clay in course of three stages of fabric development (modified after O'BRIEN & SLATT (1990). b) Pole figures and reference system.

The strong shape orientation of the various platy clay minerals was characterized by X-ray diffraction texture measurements performed on sample cylinders with 20 mm in diameter which were cored perpendicular to the macroscopically visible foliation (Analyst: G. BRAUN, University of Kiel). Characteristic lattice planes (hkl) of various clay minerals were measured (00x) with a diffraction goniometer in reflection mode using $\text{Cu}(k\alpha)$ and necessary intensity corrections were made (e.g. BRAUN, 1994). The pole figures are given in equal area projection (upper hemisphere) corresponding to the reference system.

Figure 2-4b shows the pole figures for (002) of chlorite and a mica mineral of the virgin material. They indicate development of marked preferred orientation of the clay aggregates. The sharp maximum of (002) axes are concentrated normal to the bedding plane and the symmetry of the clay fabric is nearly perfect axial symmetric.

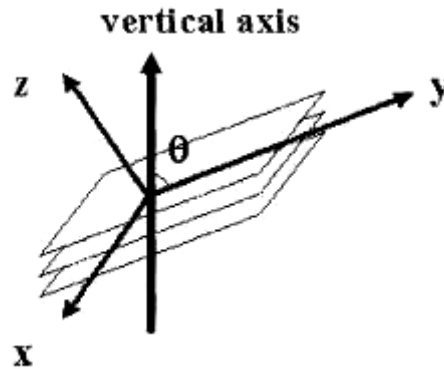
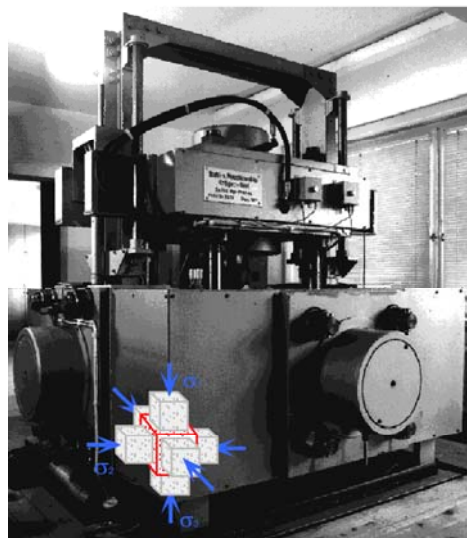


Figure 2-5. Coordinate system associated to the shale bedding structure (compare Figure 2-6).

2.2.2 Test device and procedure

The true 3D test frame of the University of Kiel (e.g. KERN et al., 1997) was used to perform the deformation tests on the cubic specimens of Opalinus Clay. In this testing device, stress or deformation can be controlled independently in all three principal directions (Figure 2-6).

Starting from hydrostatic conditions ($\sigma_1 = \sigma_2 = \sigma_3$) non-hydrostatic stresses are obtained by increasing or lowering the various principal stresses. Linear strain ($\varepsilon_1, \varepsilon_2, \varepsilon_3$) and the volumetric strain, ε_v , are determined by the measurement of the piston displacements, using two sensors on each prism side. Estimated precision of the displacement measurement is about 10^{-2} mm. The applied principal stresses σ_i were calculated and automatically corrected for deformation-related changes of the cross sections.

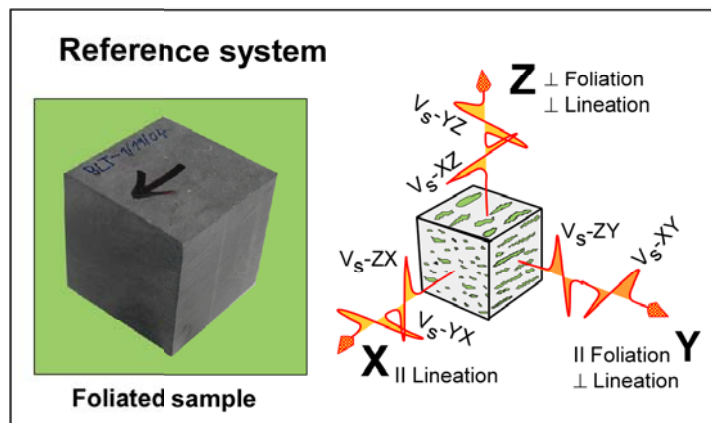


a

- 6 hydraulic rams with 2000 kN load capacity -

Sample size: 43mm edge length;

$T_{\max} = 750^\circ\text{C}$, $\sigma_{\max} = 600\text{MPa}$



b

Figure 2-6. Equipment to investigate mechanical and seismic rock properties at elevated stress and temperature conditions. a) Triaxial (multi-anvil) pressure apparatus for direct measurements of P and S-wave travel times. b) Reference system of a clay sample with regard to the polarisation directions of the various shear waves.

The special arrangement of the apparatus allows simultaneous measurements of compressional and orthogonally polarised shear wave velocities (V_{s_1} , V_{s_2}) in the three structural directions X, Y, and Z. In our experiments, the shear wave transducers were oriented such that the predominant s_1 and s_2 particular motions were parallel and perpendicular to foliation and lineation, respectively (see Figure 2-6b).

Using the ultrasonic pulse transmission technique with transducers operating at 2 and 1 MHz for P and S waves, respectively, P and S wave velocities are measured simultaneously during loading along the three directions X, Y, Z of the sample cubes. Each set of results is composed of nine velocities: three P wave velocities and six S wave velocities. Splitting of shear waves is obtained for each direction of propagation by two sets of oriented transducers with perpendicular planes. The precision of the timing measurement is ± 5 ns, and the relative timing accuracy is believed to be better than $\pm 0.5\%$.

During the loading tests, the six pistons with a plate diameter of ~ 40 mm seal only 87% of the specimen surface. This allows pore liquids to drain into air filled pores or leave the specimen, keeping the pore fluids unconfined. However, the fluid transport should be restricted due to the low permeability of the rock (HUNSCHE et al., 2004). This prevented any measurable water loss from the specimens during the short tests. The pore pressure itself could not be measured.

After initial calibration of the frame, normal stress was applied to the specimen until the desired compressive load was reached. The material was then consolidated at this constant stresses for 2 h. Thereafter, the samples effective shear stress was raised by controlled changes of the individual stresses at 0.5 MPa/min, while keeping the minimum stress constant. Upon reaching the failure as indicated by a lowered stress increase, the stresses were decreased. The minimum stresses vary between 5 and 50 MPa.

2.3 Experimental results

In this section we present results from ultrasonic measurements of p- and s-waves in the three orthogonal directions X, Y and Z of the sample cube during differential loading to characterize the dilatancy behaviour of Opalinus material. 11 cubic samples were investigated during various loading cycles in the triaxial (multi-anvil) pressure apparatus. The sample cubes have edge lengths of 43 mm. Before the experiments graphite is sprayed on the end faces of the sample cubes to minimize friction.

2.3.1 Hydrostatic loading

After fixing the rock cube in the apparatus and calibrating the system the sample was hydrostatically loaded by simultaneously increasing the load for each loading axis until the desired level is reached. During a waiting period of 1 h the sample was compacted. Due to practical reasons (e.g. coupling effects) the lowest pressure value where velocity measurements can be performed is 7.5 MPa. In Figure 3-10 p-wave velocity data are summarized as a function of hydrostatic pressure.



Remarkably, velocities measured in the foliation are nearly equal and nearly 30% higher than perpendicular to the foliation. Increase of confining pressure gives rise to a non-linear increase of p and s -wave velocities (here not shown for s -waves). Because velocity data at lower pressure are not available, we indicated for comparison the mean data range of Opalinus Clay, measured at atmospheric pressure conditions as well parallel and perpendicular to foliation (BOCK, 2001). Both velocity data sets show a remarkable scattering of the data, obviously due to lithological effects but, in average, the slope of our data measured at increased pressure corresponds nicely to the literature data.

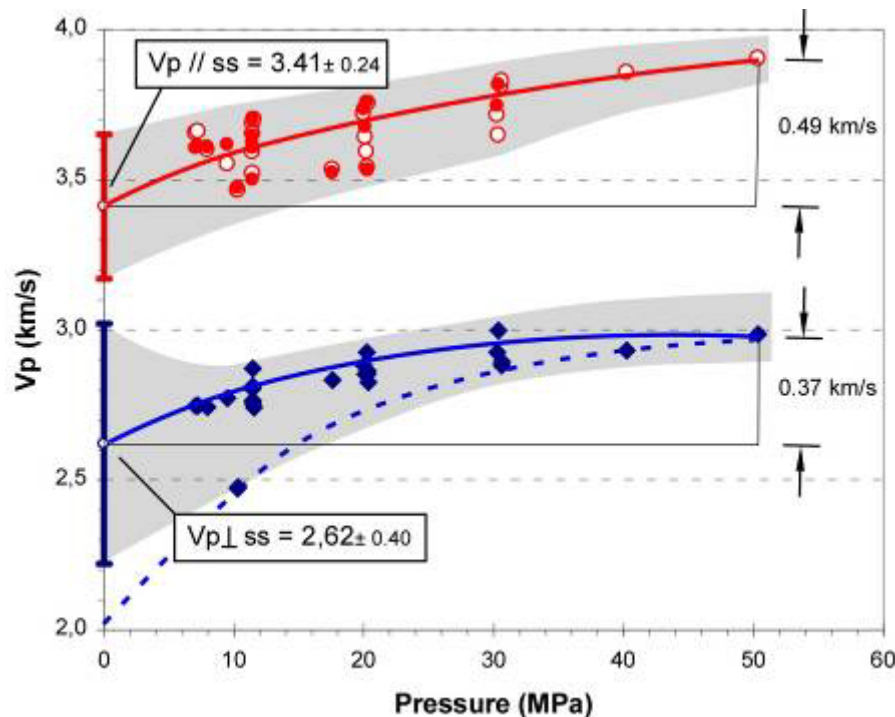


Figure 2-7. P-wave velocity variation during hydrostatic loading measured both \parallel and \perp to the bedding plane. In addition, the data ranges given in BOCK (2001) are included. The dotted line indicates the hypothetical pressure effect on velocities measured perpendicular to the bedding.

The p -wave velocities measured in the foliation are in the order of 3.41 ± 0.24 km/s and perpendicular to the foliation in the order of 2.62 ± 0.40 km/s resulting in an average p -wave anisotropy (A - V_p) of around 25% (the corresponding shear wave anisotropy is in the order of 30 to 40%).

$$A-V_p = (V_{p_{\max}} - V_{p_{\min}}) / (V_{p_{\text{mean}}}) \cdot 100 \quad (\%)$$

The pressure dependent velocity increase is more pronounced for velocity measurements parallel to the foliation ($\Delta V_p \parallel ss = 0.49$ km/s / 50 MPa) than perpendicular to it ($\Delta V_p \perp ss = 0.37$ km/s / 50 MPa) although the reverse should be more typical. As a consequence, the p -wave anisotropy remains nearly constant. This is surprising because as pointed out by many authors (for details see IFG, 2005a), in rocks with sheet minerals, the most effective cracks

[NF-PRO]



are open grain boundaries which are oriented more or less parallel to the bedding and these cracks should be progressively closed with pressure.

However, note that the scattering of the velocity data measured perpendicular to the foliation at atmospheric conditions is higher than those measured in the foliation, and also significantly higher, than that, that was measured at increased pressures. From our feeling, velocity measurements perpendicular to the foliation are much more critical (due to the high absorption due to open grain boundary cracks) and often impossible. Therefore, the data sets seem to represent more or less relatively higher velocities from intact material whereby the lower spectrum is not enough represented. However, for solving this problem regarding the compaction induced velocity variation in various sample orientations one needs a complete pressure cycle starting at very low pressure.

2.3.2 Deviatoric loading / evaluation of strength data

After hydrostatic compaction, the samples were deformed perpendicular to bedding in triaxial compression ($\sigma_1 > \sigma_2 = \sigma_3$) by increasing σ_1 with a loading rate of 0.2 MPa/min. The investigations were supplemented by some deformation experiments at extensional conditions and also by some test with sample orientations with 90° resp. 45° to the bedding. The applied confining pressure varied between 7.5 and 50 MPa.

Figure 2-8 presents a partial set of experimental data for two experiments deformed at 7.5 and 10 MPa confining pressure. P-wave velocities together with the stress curve are plotted as a function of axial strain. For the experiment performed at $\sigma_2 = \sigma_3 = 20$ MPa the corresponding curves of s-wave variation and the linear strains are shown in Figure 2-10.

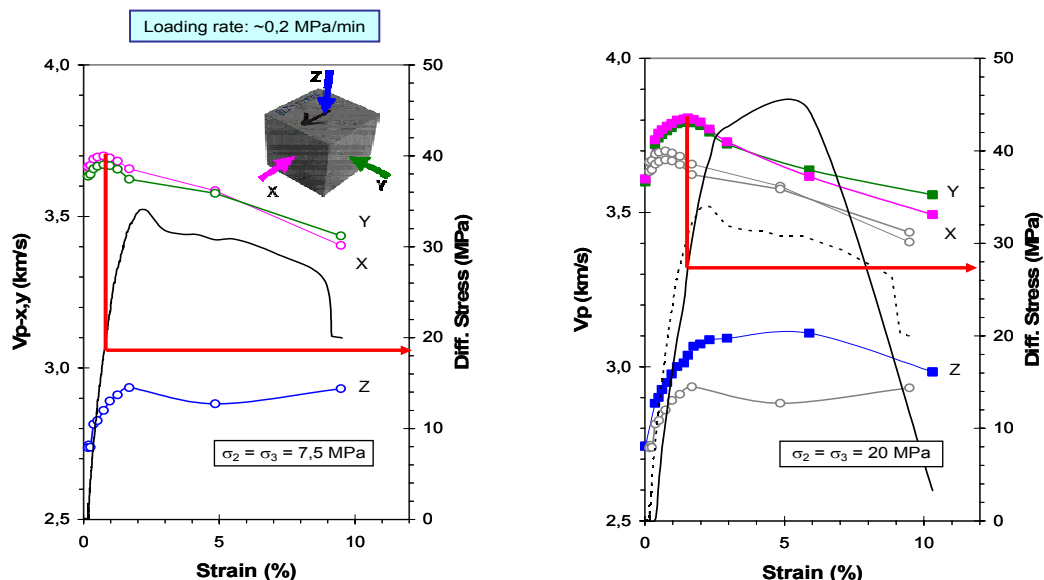


Figure 2-8. Differential loading of Opalinus Clay (perpendicular to the bedding) with simultaneous monitoring of Vp with $\sigma_1 \gg \sigma_2 = \sigma_3$ ($\sigma_1 \parallel Z$; $\sigma_2 \parallel Y$; $\sigma_3 \parallel X$): p-wave velocities (for the three axis) and differential stress vs. axial strain. (left) $\sigma_2 = \sigma_3 = 7.5$ MPa; (right) $\sigma_2 = \sigma_3 = 20$ MPa.

[NF-PRO]



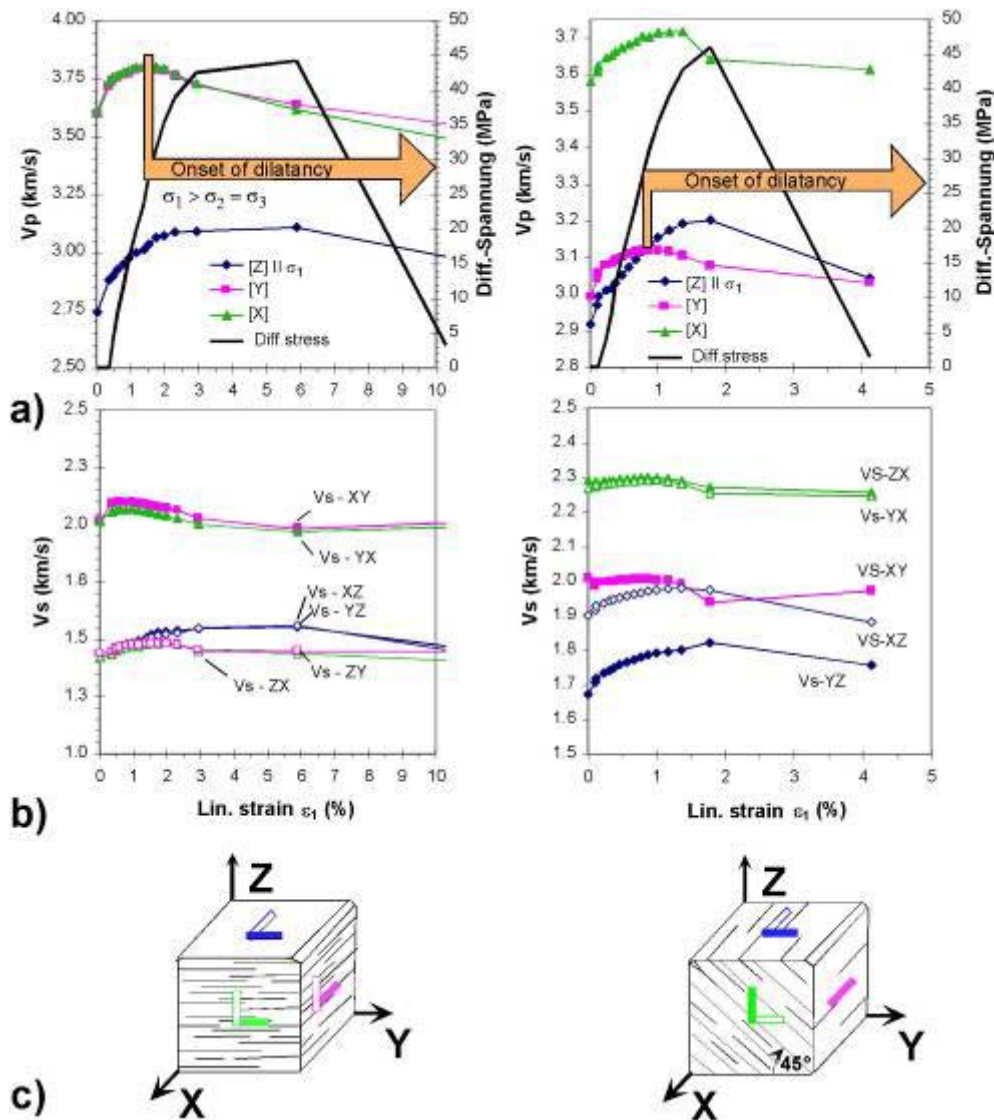


Figure 2-9. Relationships between Vp and Vs as a function of deformation at room temperature during deformation of Opalinus Clay: loading direction normal (left) and 45° to bedding (right); compression test $\sigma_1 > \sigma_2 = \sigma_3 = 20$ MPa; stepwise loading increase. a) Vp and Diff. stress ($\Delta\sigma_{\text{diff}} = \sigma_1 - (\sigma_2 + \sigma_3)/2$), b) Vs, and c) Reference system.

Starting from hydrostatical conditions the axial load (referred to the actual sample diameter as σ_1) was increased, while keeping the radial stresses constant. The slope of the stress-strain curve shows the characteristic transition from initial quasi-elastic (linear) behaviour to a curve with relatively large radius indicating typical strain hardening until failure at a strain 3 resp. 6 %.

As evident from both experiments, the initial stage of deviatoric loading is characterized by a significant increase of p- (and s-wave velocities) due to initial compaction. Further triaxial deformation gives rise to marked changes of the physical properties, in most cases in the opposite direction whereby the directional behaviour is strongly related to the bedding planes.

[NF-PRO]

Report – Deliverable 4.2.15

Dissemination level : PU

Date of issue of this report : 01/10/07



Generally, all experiments show the same physical parameter signature related to the measuring direction with strain: p-wave and s-wave velocities measured parallel to the deformation axis (in these experiments perpendicular to the bedding) still increases whereas all velocities measured in the other directions start to decrease due to the onset of dilatancy. Opening of cracks perpendicular to the stress axis is indicated by velocity decrease of radially measured p-waves or s-waves (oscillation direction \perp to bedding). The initial sharp velocity drop associated with a sharp increase of deformability is followed by a period of a more or less directly strain related velocity decrease.

It should be mentioned that the overall measured directional velocity signature is directly related to the quasi-hexagonal symmetry of the clay samples. Figure 2-9 compares the velocity behaviour of two samples where the deformation axis is oriented 90° resp. 45° to the bedding plane. Note that both measurements confirm transversal anisotropy with the symmetry axis normal to bedding plane. It is clear that velocities measured in the foliation are approximately 30% faster than perpendicular to the bedding. In addition, only in the foliation a shear wave splitting occurs, whereby shear wave with oscillation directions \parallel bedding are nearly 40% higher than \perp . Measurements at off-axis angles (nominally 45°) are between these extreme values. In particular, the shear waves measured in X-direction, which are equal, confirm the quasi-hexagonal symmetry (Figure 2-9a).

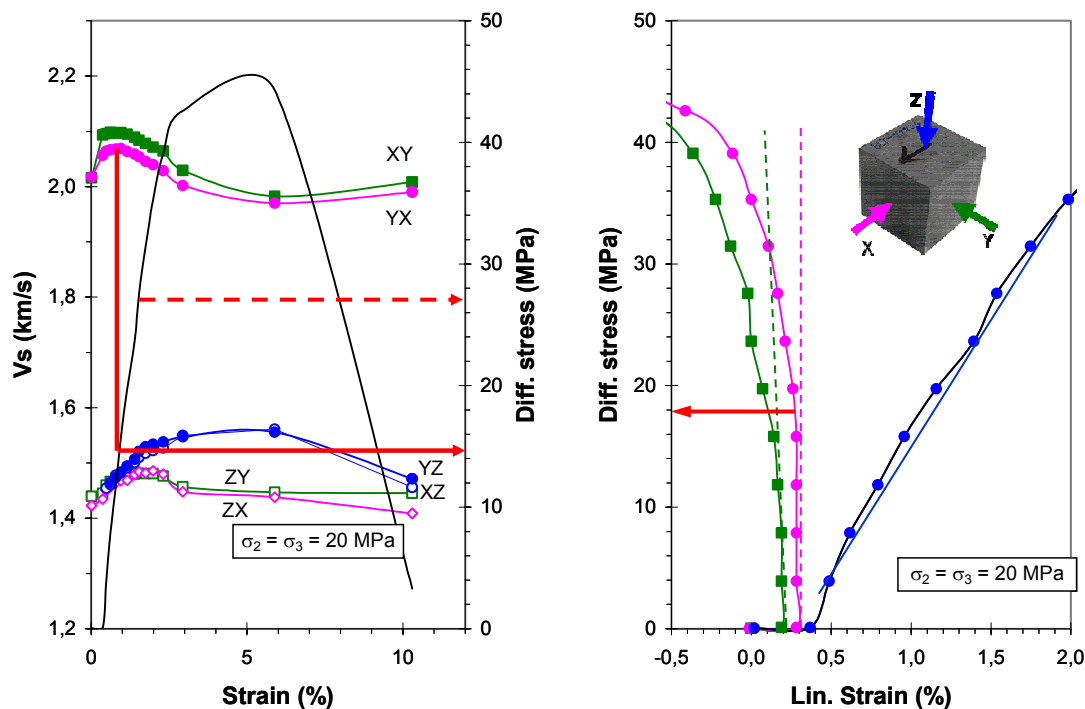


Figure 2-10. Differential loading of Opalinus Clay at (perpendicular to the bedding) with simultaneous monitoring of Vs with $\sigma_1 \gg \sigma_2 = \sigma_3 = 20$ MPa ($\sigma_1 \parallel Z$; $\sigma_2 \parallel Y$; $\sigma_3 \parallel X$):

(left) s-wave velocities (for the three axis) and differential stress vs. axial strain. Note, that the stress limit obtained from the p-wave maximum of Figure 3-11 is indicated by the dotted line.

(right) linear strain (for the three axis) vs. axial strain.

In order to investigate the dilatancy behaviour we also evaluated the linear strain in the three directions and calculated the volumetric strain (Figure 2-10 right). However, comparing the lateral strain parallel to the bedding with the axial strain it is obvious that the compression behaviour of the sample is dominated by the axial compression in direction perpendicular to the bedding plane resulting in an overall compaction. Some authors observed onset of dilatancy (increase of volume) during triaxial deformation of various clay rocks prior to failure, but only at confining pressures of some MPa (e.g. ZHANG & ROTHFUCHS, 2005; VALES et al., 2004).

The stress level of the pronounced shear wave velocity decrease corresponds with the coeval significant increase of deformability whereas the Vp-maximum is shifted to significantly higher stress values (Figure 2-10).

Remarkable, the reversals of the various parameters are strongly pressure dependent, e.g. as can be seen by comparing both experiments in Figure 2-8. In addition, also the failure strength increases with increasing pressure.

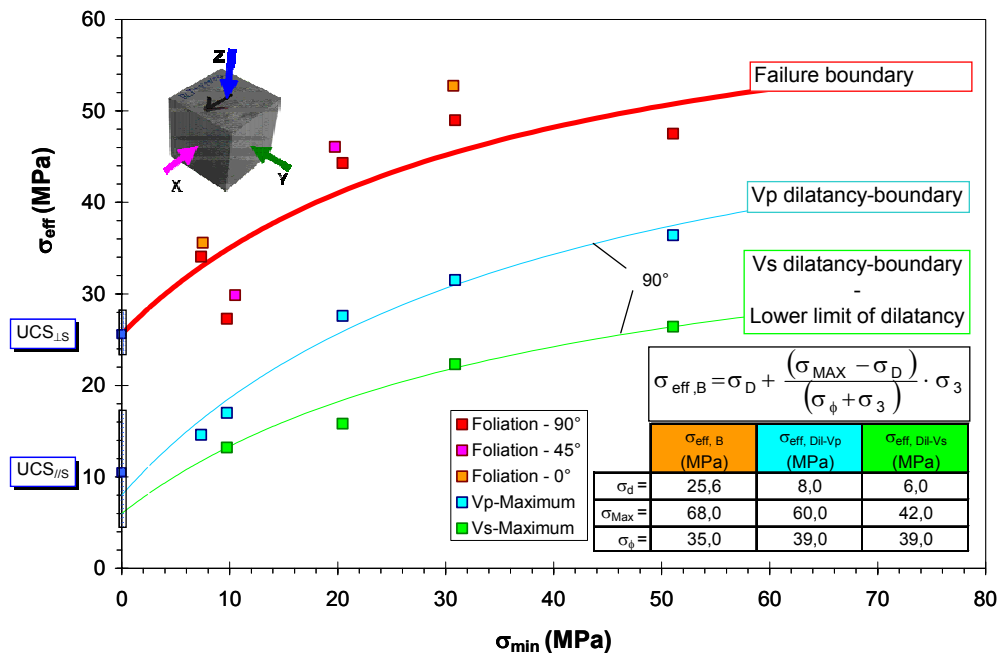


Figure 2-11. Preliminary failure and dilatancy resp. damage boundary curves obtained by the characteristic behaviour of various measured parameters: short-term triaxial compression tests on sample cubes with bedding planes oriented mostly in deformation direction. For comparison the mean uniaxial strength ranges (UCS), parallel and perpendicular to the bedding, are indicated (taken from BOCK, 2001). In addition, the parameter sets for the various curves, following the MINKLEY-formalism, are included. Note: that a revised version of this diagram is given in Figure 3-12.

Figure 2-11 summarizes the results of the failure strength values from the various tests. Remarkable, the data show some scattering but no significant difference is observed between samples loaded parallel or perpendicular to the foliation, although this is clearly indicated by the UCS-values. However, after the experiment the specimens of both loading geometries

show nearly the same failure type with a complex shear plane oriented at around 45° to the deformation axis as indicated by the frac pattern example shown in Figure 2-12. This effect is obviously due to the cubic shape of the samples which favours frictional effects between sample surfaces and the pistons. In consequence, the lithological effects of the bedding plane are overlapped by the sample geometry, which means that this investigation technique is not useful for determining the strength parallel to the bedding. In contrast, experiments on sample cubes, oriented 45° to the deformation axis show a significantly lower failure stress.

For data evaluation we used a non-linear failure criterion on the basis of a modification of the MOHR-COULOMB model which is describe in detail by MINKLEY et al. (2001):

$$\sigma_{1,B} = \sigma_D + \left(1 + \frac{\sigma_{MAX} - \sigma_D}{\sigma_\phi + \sigma_3} \right) \sigma_3 \quad (2-1)$$

respectively

$$\sigma_{eff,B} = \sigma_D + \frac{\sigma_{MAX} - \sigma_D}{\sigma_\phi + \sigma_3} \sigma_3 \quad (2-2)$$

Where σ_3 = minimum principal stress, $\sigma_{1,B}$ = maximum principal stress at failure, $\sigma_{eff,B} = \sigma_{1,B} - \sigma_3$ = maximum effective stress at failure, $\sigma_D(\varepsilon^P)$ = uniaxial compressive strength, $\sigma_{MAX}(\varepsilon^P)$ = maximum effective strength, $\sigma_\phi(\varepsilon^P)$ = curvature parameter for strength surface, $\sigma_D(\varepsilon^P)$ = uniaxial compressive strength and ε^P = plastic shear deformation.

As σ_D -value we used the uniaxial strength for samples loaded perpendicular to the bedding.

Table. 2-2. Results from triaxial deformations tests in the multi-anvil apparatus.

Exp. No.	Sample	density (g/cm ³)	Foliation (°)	Type	$\sigma_2 = \sigma_3$ (MPa)	$\sigma_{Diff_{max}}$ (MPa)	$\sigma-Dil_{min}$ V_s (MPa)	$\sigma-Dil_{max}$ V_p (MPa)
1019	BGR-BLT 1/19/03	2.439	0	Compr.	7.5	35.6	-	14.8
1022	BGR-BLT 1/19/05	2.439	0	Compr.	30.7	52.7	-	39.0
999	BGR-BLT 2/13/02	2.441	45	Compr.	10.5	29.8	17.5	21.4
998	BGR-BLT 2/14/02	2.415	45	Compr.	19.8	46.1	27.4	35.2
1018	BGR-BLT 1/19/02	2.439	90	Compr.	7.3	34.1		14.6
1017	BGR-BLT 1/19/01	2.434	90	Compr.	9.7	27.3	13.2	17.0
1000	BGR-BLT 2/13/03	2.439	90	Compr.	20.4	44.3	15.8	27.6
1021	BGR-BLT 1/19/04	2.441	90	Compr.	30.9	49.0	22.3	31.5
1023	BGR-BLT 1/16/02	2.451	90	Compr.	51.1	47.5	26.4	36.4
1024	BGR-BLT 1/16/03	2.442	90	Extens.	10.4	36.4	-	30.0
1026	BGR-BLT 1/16/05	2.443	90	Extens.	20.6	32.4	15.2	25.1

2.3.3 Crack patterns

Comparison of the microstructures of the deformed material gives evidence for widespread occurrence of microcracking and thus supports the assumption that the observed changes of velocities are mainly caused by microfracturing. Figure 2-12 shows typical crack structures of a specimen deformed at 10 MPa confining pressure. Three types of cracks can be distinguished.

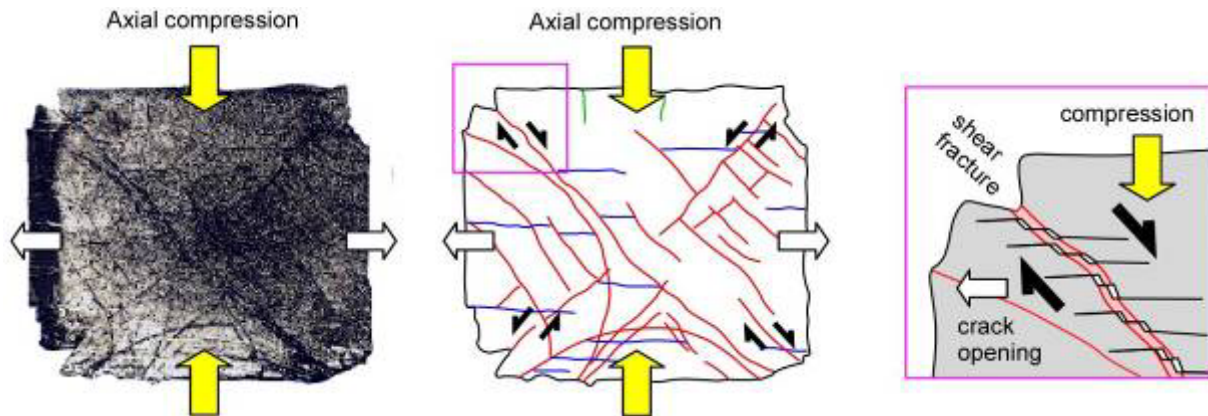


Figure 2-12. Photographs of macroscopical cracks of a deformed sample cube: BLT 1/19/02 $\sigma_2 = \sigma_3 = 7.5$ MPa; $\sigma_{\max} = 34.1$ MPa

(left) sample surface. (middle) schematic crack patterns: blue – bedding plane fractures; red – shear fractures; green – tension fissures. (right) schematic example of en-echelon tension fractures in the shear zones

In axial compression a central shear plane is developed by sets of narrow-spaced open cracks which are aligned 45° to the axis of maximum stress. Due to movement along the shear planes en-echelon tension gashes are opened oblique to the shear direction so that local crack opening tends to align preferably parallel to the principal compressive strain axis.

Opened bedding planes (blue) are due to the general decompaction after unloading the sample. In the contact zone between piston and sample additional tensional fractures occur due to frictional effects.

2.3.4 Discussion

The investigated Opalinus Clay with its well-developed bedding planes exhibits the characteristic behaviour of a bedded rock with quasi-hexagonal symmetry:

- Elastic wave propagation in indurated clay is significantly effected by the bedding planes, e.g. seismic anisotropy and shear-wave splitting: $A-V_p \approx 25\%$.
- Increase of stress decreases significantly velocity anisotropy and shear-wave splitting in the prefailure stage due to compaction processes of the bedding.

Based on the spatially measured velocity variations of both p- and s-waves onset of microfracturing is clearly identified whereby anisotropy and overlapping compaction effects have to be considered. A complete discussion of the dilatancy related phenomena respectively derivation of the damage and dilatancy boundary corresponding to the results of the investigations performed in the multi-anvil apparatus and the triaxial cell is given in chapter 3.6.

[NF-PRO]

3 Coupled hydraulic and mechanical properties during triaxial loading

3.1 Introduction

In this section we present results from triaxial testing with simultaneous monitoring of ultrasonic wave velocities (V_p , V_s), dilatancy and gas permeability to characterize the coupled hydraulic-mechanical behaviour of Opalinus material at hydrostatic and deviatoric conditions using cylindrical clay samples (4 parallel and two perpendicular to the bedding).

3.1.1 Sampling and preparation of cylindrical clay samples

For core recovery the central heater borehole (BHE-D0) of the HE-D Experiment was used which is located in homogeneous shaly layers of the sandy facies (see Figure 2-3). The drill-hole was drilled by the French drilling company COREIS with the double core barrel techniques, using compressed air as drilling medium in spring 2004 (Figure 3-1). The technical borehole data are summarized in Table 3-1.



Figure 3-1. Sampling at the Mont Terri site. (left) drilling equipment from COREIS, (right) core samples with individual length of around 1.5 to 2.5 m (core diameter: 26 cm)

Finally 10 core segments with a total core length of around 4 m were sampled between 2 and 7 m depth and immediately sealed with aluminium foil to avoid humidity loss (before sealing the foil tubes were evacuated). At the IfG in Leipzig the sealed samples were stored in a cellar at average conditions of 16°C and around 80% r.h.

From the large cores cylindrical samples were drilled very carefully with a special core drilling set (tube end equipped with hard metal crumble) in a modified lathe (automatic slow transmission of the drilling tube) with continuous extraction of the drilling dust by an integrated vacuum cleaner. Because the cylinder surfaces are sufficiently smooth, only the cylinder

ends were flattened and polished in a lathe. However, despite all care, due to the core disturbances generated during sampling the cylindrical samples contain sometimes some pre-existing fractures oriented parallel to the bedding planes (Figure. 3-2).

Table 3-1. Technical data of the BHE-D0 borehole (taken from Mont Terri project, 2004)

Borehole	Drilling technique	“Drilling fluid”	Tunnel metre NG	Length (m)	Azimuth of dip (°)	Dip angle* (°)	Diameter (mm)	Location Bm*	Remarks
BHE-D0	DC ⁺	Air	HE-D niche	13	240	0	300/260	Front wall	• Heater bore-hole

* Abbreviations: DC – Double core drilling; Bm - borehole mouth (m) at tunnel wall; Dip angle: + up; - down

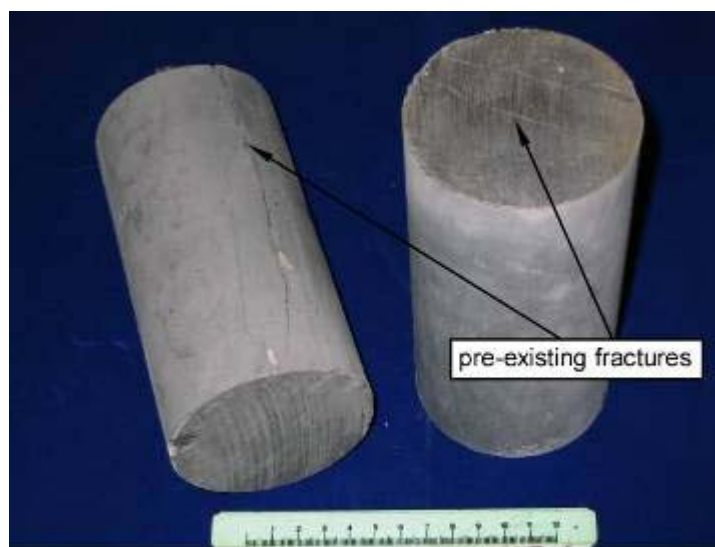


Figure. 3-2. Cylindrical samples – 80 mm diameter and 160 mm length (cored parallel to the bedding).

According to the structural findings presented in chapter 2.2.1 the prepared samples show thin bedded dark grey clay minerals with a typical anisotropic texture of clay particles parallel the bedding surface. Tectonic and artificial stressing during core recovery and sample preparation sometimes result in fracture development mostly parallel the bedding. Further, it is not excluded that a secondary crack system with oblique fracture or shear planes occurs. Samples showing these types of failure were generally rejected.

3.1.2 Triaxial pressure device – volumetric strain measurement

The experiments were performed in a standard Karman-cell (e.g. KÁRMÁN, 1911) in the servo-hydraulic testing machine (RBA 2500, Schenk/Trebel Germany – using the MTS-Teststar software) allowing independent control of the radial ($\sigma_2 = \sigma_3 = p_c$) and axial stresses ($\sigma_{Ax} = \sigma_1$). In addition, using the updated piston sets acoustic velocities (V_p and V_s) and gas-permeability were measured parallel to the cylinder axis in compression ($m = -1$). The cylindrical samples are sealed with rubber tubes and oil is used as confining medium. Outside the

[NF-PRO]



vessel three LVDT transducers are mounted between the piston and the load frame near the sample for the measurement of the axial strain. The axial load is determined from an external load cell.

Axial deformation experiments (Δh resp. the deformation $\varepsilon_1 = \Delta h / h_0$) in compression or extension mode can be performed at various confining pressures (p_c up to 100 MPa) and at temperatures up to 100°C within a deformation rate range of $\dot{\varepsilon}_1 = 10^{-5} - 10^{-7}$ 1/s to chosen values of ε_1 . As a standard technique during the experiments the sample volume changes ΔV are determined by a volume balance of the mantle oil volume changes as measured via the pressure intensifier and the axial piston displacement in the cell:

$$\Delta V = \Delta h \cdot A_{PP} - \Delta S_{PI} \cdot A_{PI} \quad (3-1)$$

with ΔS_{PI} = displacement of the cylinder within the pressure intensifier

A_{PI} = cross section of the piston within the pressure intensifier

Δh = displacement of the piston of the triaxial cell

A_{PP} = cross section of the piston of the triaxial cell.

$$\varepsilon_V = \frac{\Delta V}{V_0} \quad (3-2)$$

In calculation of the stress difference ($\sigma_1 - \sigma_3$) deformation induced variation of the cross section of the specimen is considered.

The leakage-freeness of the oil volume measurement equipment is tested before beginning of each measuring cycle over a waiting period of ca. 1 hour. However, the accuracy of the volume measurement depends on the constancy of the oil temperature within the triaxial cell and within the pressure intensifier.

3.1.3 Simultaneous measurements of ultrasonic wave velocities and gas-permeability

As shown in the schematic drawing of the triaxial pressure cell (depicted in Figure 3-3) ultrasonic wave velocities and permeability can be measured simultaneously parallel to the sample cylinder axis (dimensions: 80 mm in diameter and 160 mm long). To maintain access of the gas to the sample, a central hole exists in the plates whereby the specimens additionally will be prepared with small boreholes on their axial ends (diameter 5 mm, length 40 mm) to minimize end effects during straining. For the velocity measurements, two sets of transducers for generating and receiving p and s waves are mounted on the back side of the piston platens in the free area outside of the central part (for details see Figure. 3-4).

Compressional and shear waves are generated by means of PZT piezoceramic transducers (1 MHz), and velocity measurements are done with an ultrasonic-receiver (Krautkrämer USD 10 NF) using the ultrasonic pulse transition technique with the transducers placed in the two opposite pistons. The wave velocities are calculated by dividing the length of the sample by the actual travel times. Calibration of the device for the p and s-wave velocity measurements is based on steel samples as a reference standard. The accuracy of the ultrasonic measurements is better than 1%.

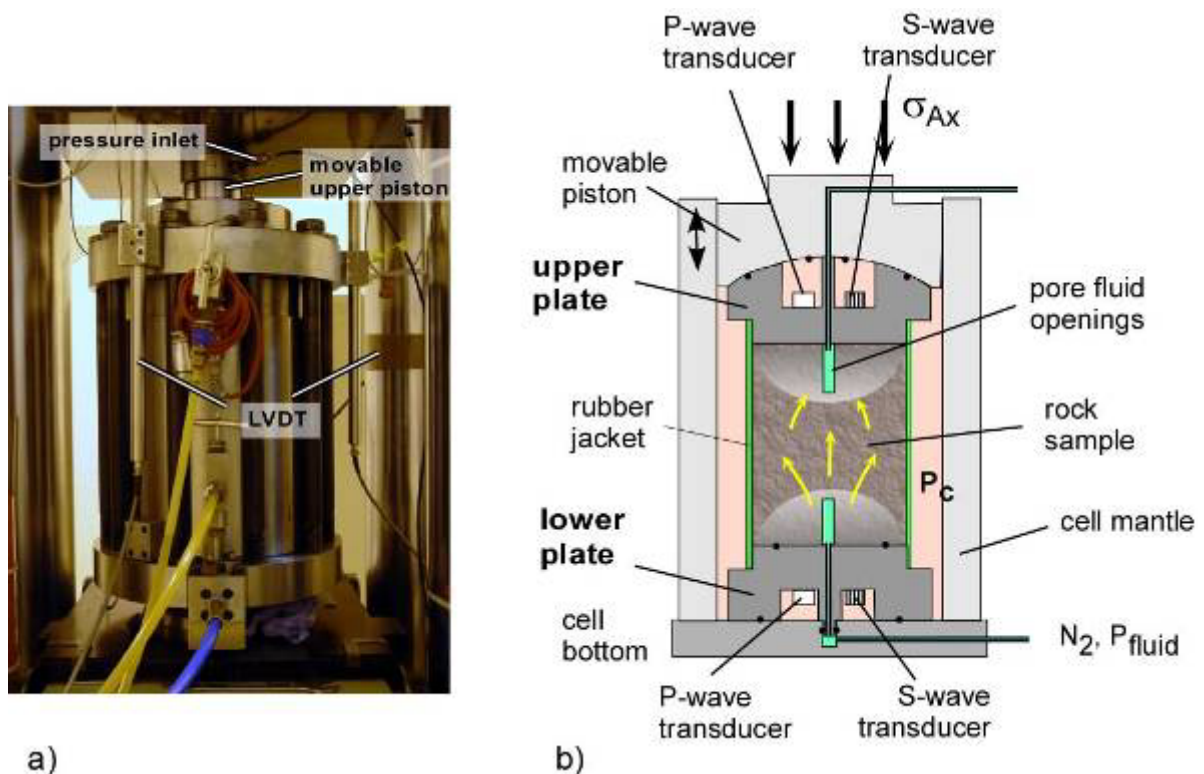


Figure 3-3. (a) The triaxial cell of the RBA 2500 and (b) the scheme of the pressure vessel. Note the new plates for simultaneous measurements of P and S wave velocities and gas permeability.



Figure. 3-4. New constructed end plates of the pistons for simultaneous measurements of P- and S-wave velocities and permeability.

Gas-permeability is measured using nitrogen with an equipment similar to that described by PEACH & SPIERS (1996), allowing both transient and stationary permeability measurements.

Two methods are used to determine the gas flow (q) through the samples. To perform the permeability measurement the primary gas pressure p_1 is applied. Its value depends on the test specimen's permeability and on the measurement range of the gas flowmeter (0 - 10 resp. 0 - 500 cm^3/min ; manufacturer: BRONKHORST; model: F-230M).

[NF-PRO]

Report – Deliverable 4.2.15

Dissemination level : PU

Date of issue of this report : 01/10/07



Alternatively, using a defined gas volume on the in- (V_1) and outlet (V_2) and measuring the pressure increase, Δp_2 resp. $\dot{p}_2 = \frac{\Delta p_2}{\Delta t}$ is verified to determine $\dot{V}_2 = V_2 \cdot \dot{p}_2$, whereby $q \hat{=} \dot{V}_2$.

At a given injection pressure, gas enters into the assumed relatively large pores and displaces the pore water. This process is regarded as two-phase flow. After reaching a stationary flow through the specimen, the amount of gas flow over a defined period of time is recorded (q).

The intrinsic permeability is calculated by the modified Darcy's law for compressive media:

$$k = \frac{2\eta \cdot l}{A} \cdot \frac{q \cdot p_L}{(p_1^2 - p_2^2)} \quad (3-3)$$

with η = dynamical viscosity
 $l = (h - t)$ = effective length of the flow path through the sample
 h = height of the sample
 A = cross section of the sample
 p_L = pressure at gas flow measurement
 t = sum of the length of both holes in the sample
 p_1 = injection pressure
 p_2 = outlet pressure

The absence of leakage of the permeability equipment is tested before each measuring cycle using a steel sample over a waiting period of around 1 hour.

3.2 Experimental results

3.2.1 Gas injection tests at various compaction states

The gas-permeability and seismic characteristics of the cylindrical clay samples were investigated directly after sampling and preparation without any pre-compaction. Therefore, some sample disturbances resulting in interconnected pore space should be expected. Nevertheless, this material should be used as representative for material in the EDZ. The internal humidity content was estimated to be in the order of 5 – 6 wt.-% corresponding to literature data, resulting in a partially or, depending on the degree of the applied compaction, nearly saturated pore space.

Due to the presence of water in the rock matrix two-phase flow will occur during the injection of gas which is associated with capillary effects. Fluid transport is then controlled by the interfacial tension of the fluids involved, the wettability of the solid surface (wetting angle) with respect to the fluids, and the structure of the pore system. According to the Washburn equation (WASHBURN, 1921) intrusion of a non-wetting fluid into a cylindrical capillary of radius r only occurs if the capillary pressure p_c (i.e. the pressure difference between the two immiscible fluids with p_1 and p_2) within a pore is exceeded:

$$p_c = p_2 - p_1 = -\frac{2 \cdot \gamma \cdot \cos \theta}{r} \quad (3-4)$$

Here γ is the interfacial tension [N/m], and θ the wetting angle [degrees] and r is the radius [m] of the ideal cylindrical pores.

As schematically depicted in Figure 3-5 the capillary sealing efficiency of a porous medium with a heterogeneous pore system (i.e. a given pore-size distribution) is characterised by the “break through” or “threshold pressure” (p_T). This term refers to the excess pressure in the non-wetting phase at which the wetting phase is displaced to an extent that the percolation threshold is exceeded and continuous flowpaths of nonwetting phase form across the pore system. These flowpaths will comprise the largest interconnected pores, which offer the least resistance to capillary displacement. At this stage the flow of the non-wetting phase will be focused and restricted to a small portion of the interconnected pore system. If the excess pressure increases further, additional fluid flow pathways will develop across the porous medium, thus increasing the effective permeability to the non-wetting phase and the non-wetting phase saturation.

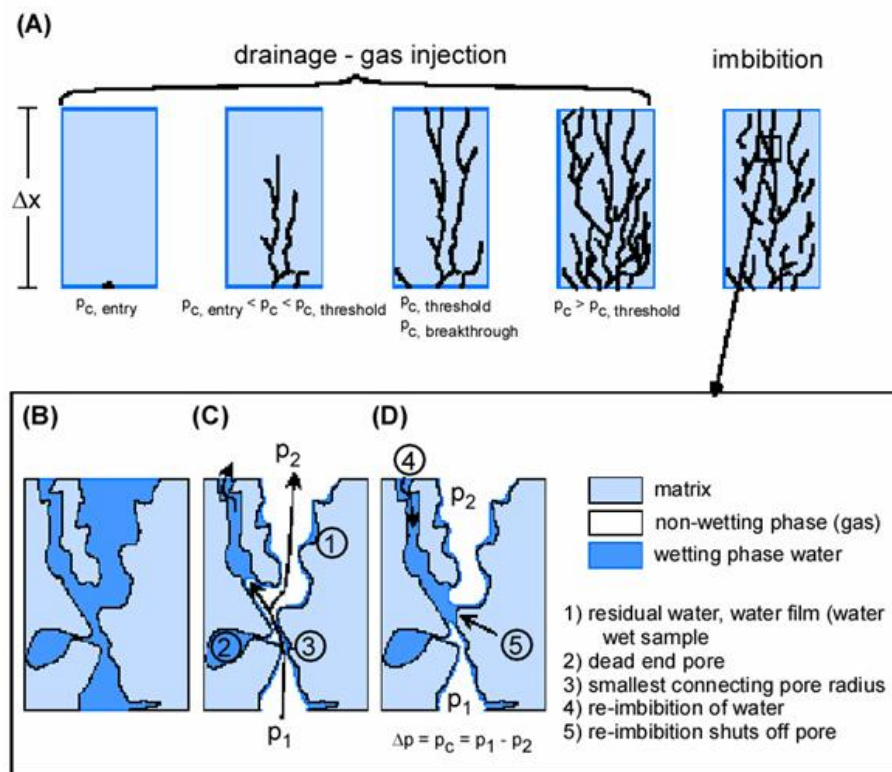


Figure 3-5. (a) Stages of capillary gas breakthrough (drainage) and re-imbibition process in fine-grained rocks (schematic); (b) initially water-saturated sample; (c) gas breakthrough, (d) re-imbibition (modified after HILDENBRAND, 2003).

In this study gas breakthrough experiments on 5 clay samples are being performed by step-wise gas injection with increasing gas pressures and monitoring of the gas outflow resulting in different stages of 2-phase flow. Sample parameters are shown in Table 3-2. During each

gas injection step constant single-phase flow (N_2) was registered for an extended period of time and then the experiment continued.

Table 3-2. Sample parameters for the various injection tests.

Sample	Height h (mm)	\varnothing d (mm)	Density ρ (g/cm^3)	Injection direction referred to the bedding	Remarks ^{*)}
307 / OPA 1	181,58	90,32	2,439	0°	Sinter plates
307 / OPA 2	180,81	90,17	2,442	0°	hole
307 / OPA 4	160,14	80,08	2,450	0°	hole / US ^{**)}
307 / OPA Kon 1	150,45	73,59	2,366	90°	hole / US ^{**)}
307 / OPA 11	140,99	80,16	2,438	90°	hole / US ^{**)}

^{*)} Application of the pore fluid to the sample.

^{**)} Simultaneous crack monitoring with measuring V_p and V_s .

Exemplary, results from two gas injection cycles perpendicular to the bedding of sample OPA 307/Kon1 measured before and after sample compaction are presented. The investigations are mainly aiming on gas-transport properties depending on the gas-pressure and the hydrostatic confinement. The experiment consist of two stages, before and after compaction, whereby the first test series was performed in two steps:

- (1) Hydrostatically loading of the sample up to 1 MPa and stepwise increasing the gas pressure up to 9 bar
- (2) At constant gas pressure (~ 9 bar) stepwise increasing the confining pressure up to 3 MPa.

In the first stage we did not observe a remarkable influence of the height of gas pressure on the gas flow resp. on the resulting permeability which may indicate that in the highly dilated sample only single-phase transport occurs according to the particular saturation and porosity conditions. However, at constant pressure conditions we observed a discontinuous decrease and later recovery of gas flow which is interpreted as intermittent gas transport due to alternating re-displacement processes of the 2-phases in the pore space.

In the second stage at constant gas pressure we observed in accordance to Figure 3-9 a stepwise decrease of gas flow due to the progressive compaction of the pore space depending on the confining pressure. This process is obviously overlaid by time dependence.

After compacting the sample during a deformation cycle, which results in a very low permeability, e.g. below the detection of the gas-flow meter which corresponds to a permeability of $< 10^{-20} m^2$, the gas-injection test was repeated at $p_c = 3 MPa$. During stepwise increase of the gas pressure from 10 to 30 bar we observed an associated increase of the flow rate, respectively stepwise enhance of the permeability of one order of magnitude. At the 25 bar gas pressure step we observed a delayed increase of flow rate reaching a constant level according to a permeability of around $3 \cdot 10^{-19} m^2$. This behaviour was attributed to the subsequent displacement of pore fluid by gas which corresponds to the gas threshold pressure.

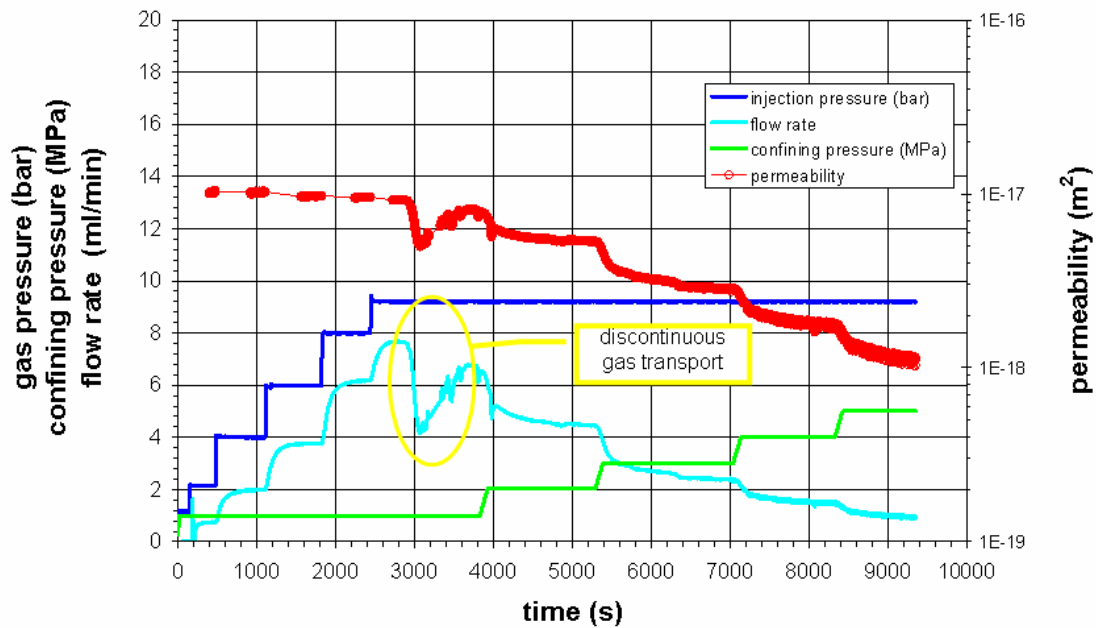


Figure 3-6. Gas-injection test on the Opalinus sample OPA 307/Kon1 with hydrostatic loading without any pre-compaction: injection \perp to the bedding with two experimental stages: (1) $p_c = 1$ MPa with stepwise increasing p_{Gas} : 1 bar \Rightarrow 9 bar; (2) $p_{\text{Gas}} = \text{const} = 9$ bar with increasing p_c : 1 MPa \Rightarrow 5 MPa.

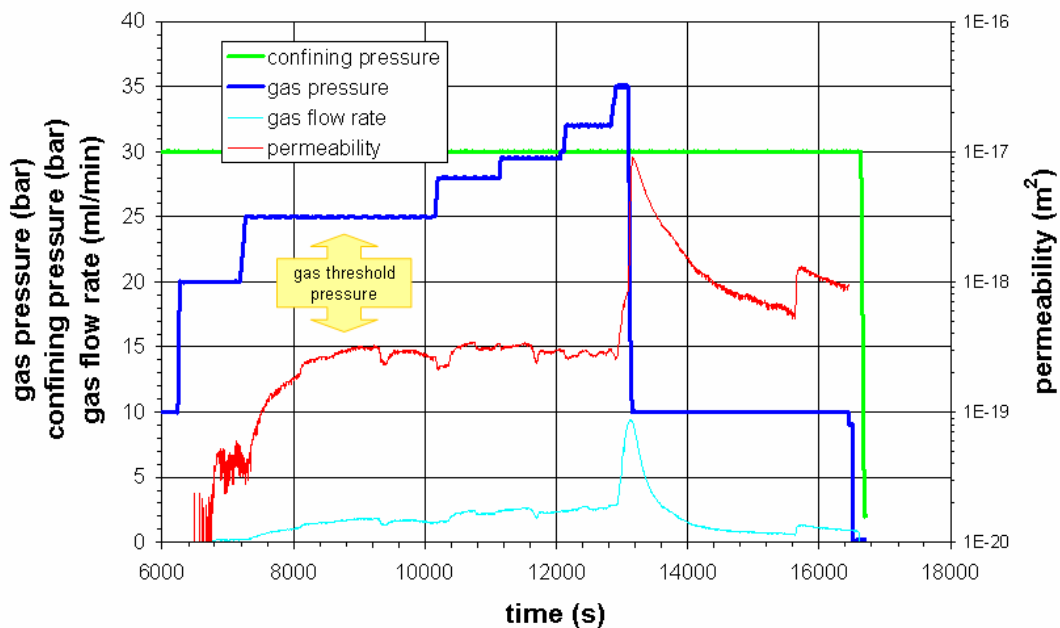


Figure 3-7. Repetition of the gas-injection test on the Opalinus sample OPA 307/Kon1 after pre-compaction due to deviatoric loading: injection \perp to the bedding at $p_c = 3$ MPa with stepwise increase of the gas-pressure.

During the further increase of gas pressure the permeability remains nearly constant, but after passing the minimal stress ($p_c = 3$ MPa) of the confinement the gas pressure ($p_p > 32.5$ bar) increases drastically up to 10^{-17} m^2 which is attributed to gas-pressure driven microfrac-

[NF-PRO]

turing (e.g. dilatancy) resulting in an expansion of the gas flow paths (e.g. MARSHAL et al., 2005). Lowering of the gas pressure to a level of 10 bars restores temporarily the initial tightness.

The results from both injection tests are included in Figure 3-8, which shows a compilation of laboratory data for the relationship between gas entry pressure and (intrinsic) permeability from various authors for different lithologies, and, in addition, of the results from Mont Terri and Benken. Regarding the term intrinsic permeability, it has to be mentioned that this term refers only to the crack free clay matrix property due to ultimate compression whereby in the case of high-porosity rocks as Opalinus Clay some remaining porosity concentrated in pores is still there but not interconnecting (e.g. KERN, 1982).

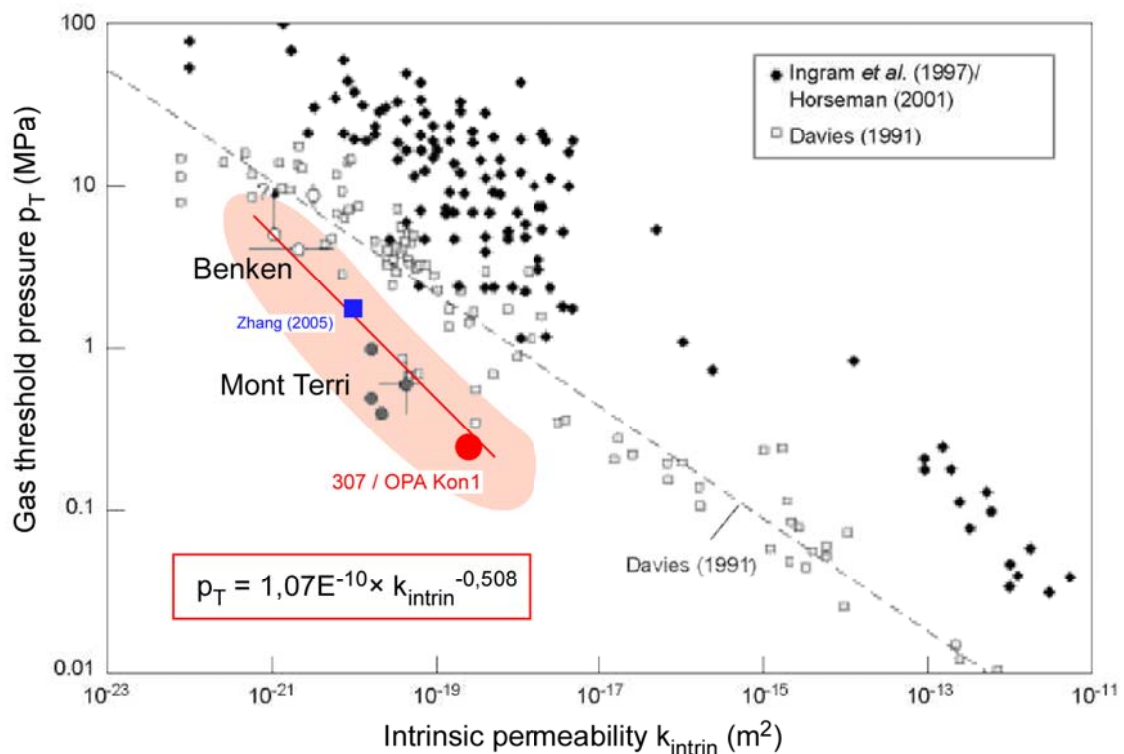


Figure 3-8. Relationship between gas threshold pressure and intrinsic permeability for various low permeability rock formations (claystones, shales, sandstone) (modified after MARSHAL et al., 2005 – for the various references see the later authors). The results obtained here are added to those from Benken and Mont Terri.

As concluded by MARSHAL et al. (2005) a clear trend between threshold pressure and so-called intrinsic permeability is seen for the different lithologies, but the spread of the data is enormous. Referring to our data, which represent high permeable clay samples, it should be noted that they correspond reasonably well to the published data of highly compacted Opalinus Clay (for details of experimental conditions of the latter samples, see MARSHAL et al., 2005) and extend, therefore, the available data base. In a first approximation, the relationship between permeability and gas pressure threshold for the Opalinus Clay corresponds in a double-logarithmic diagram to a linear trend as presented in Figure 3-8.

However, the threshold pressures determined for the Mont Terri Rock Laboratory are significantly below the various relationships from the other authors, shown in Figure 3-8. For explanation it can be argued that movement of gas along interconnected microcrack networks associated with rock dilatation may be responsible for the low entry pressure values observed for Opalinus Clay.

3.2.2 Hydrostatic loading

The hydrostatic loading was performed stepwise with $\Delta p_c \approx 1$ MPa and a loading rate of around 0.1 MPa / min in the pressure ranges 1 - 10 MPa. After each step the measurement of velocities and permeability, in particular, lasted up to several hours to receive a constant gas flow through the sample. However, it has to be mentioned that these short term experiments are always overlapped by time dependent compaction processes depending on confining pressure. In addition, as can be seen from Figure 3-8 the applied gas pressures of usually several bars are obviously higher than the necessary gas threshold pressures.

The pressure dependence of permeability and wave velocities are shown in Figure 3-9 and Figure 3-10, respectively.

Initial permeabilities vary around 3 orders of magnitude from $<10^{-17}$ m² to $<10^{-14}$ m², whereby permeabilities measured parallel to the bedding are in average two orders higher than perpendicular to it, however, the scattering of the various samples in both sample categories is also up to 2 orders of magnitude.

Depending on loading geometry to the bedding an increase of hydrostatic load from 1 to 10 MPa causes the permeability to decrease by up to 2 orders of magnitude, with linear trends in the semi-logarithmic permeability versus pressure diagram (Figure 3-9). The pressure sensitivity of permeability can be described by the relationship

$$k = k_0 \exp(-\chi * p_e) \quad (3-5)$$

where k is permeability, k_0 is the initial permeability and $p_e = (p_c - p_p)$ is the effective pressure (p_p , pore pressure; p_c , confining pressure). The parameter χ was found to be in the range of 0.13 to 0.54 MPa⁻¹, whereby the pressure effect perpendicular to the foliation is nearly two times higher than parallel to it (Table 3-3). The pressure induced compaction is only partial reversible.

In Figure 3-10 P-wave velocity data are summarized as a function of hydrostatic pressure in comparison to data measured in the multi-anvil apparatus. Depending on the measuring direction referred to the sample bedding two velocity ranges are indicated. At low- or atmospheric pressure conditions P-velocities measured \parallel to the bedding are in the range 3.15 - 3.65 km/s, and P-wave velocities measured \perp to the bedding vary between 2.15 and 3.05 km/s, and are, therefore in accordance to the literature data of BOCK (2001) resulting in an average p-wave anisotropy (A-Vp) of around 25%. Both velocity data sets show a remarkable scattering of the data, obviously due to lithological effects, but, in average, the slope of the data measured in the new IfG-cell at increased pressure corresponds nicely to the literature data.

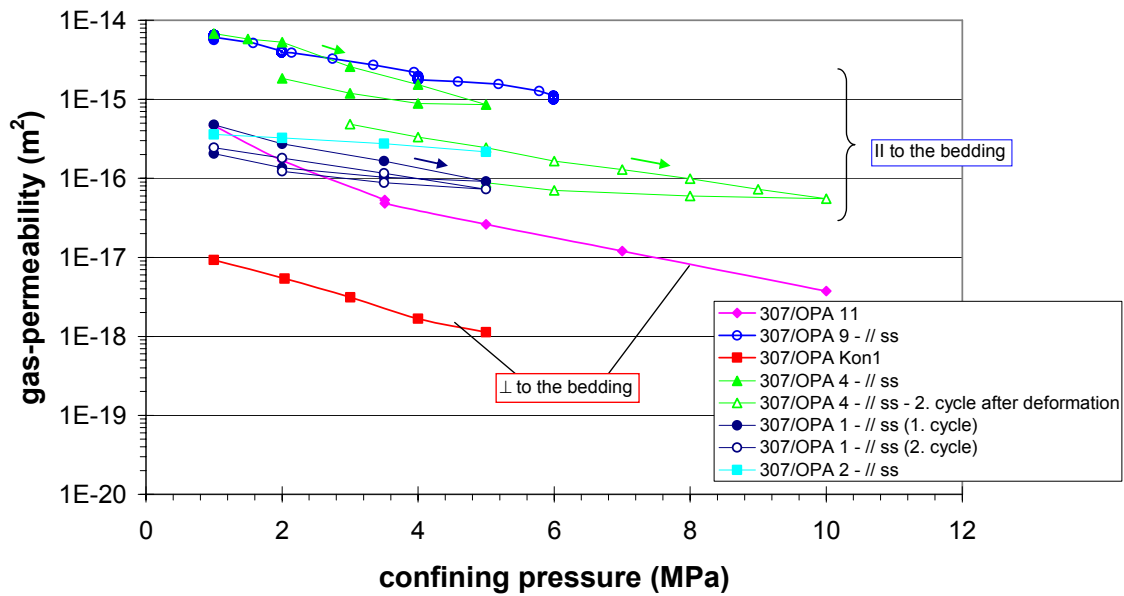


Figure 3-9. Gas-permeability change of Opalinus Clay as a function of hydrostatic pressure. The material was investigated directly after sampling and preparation without any pre-compaction.

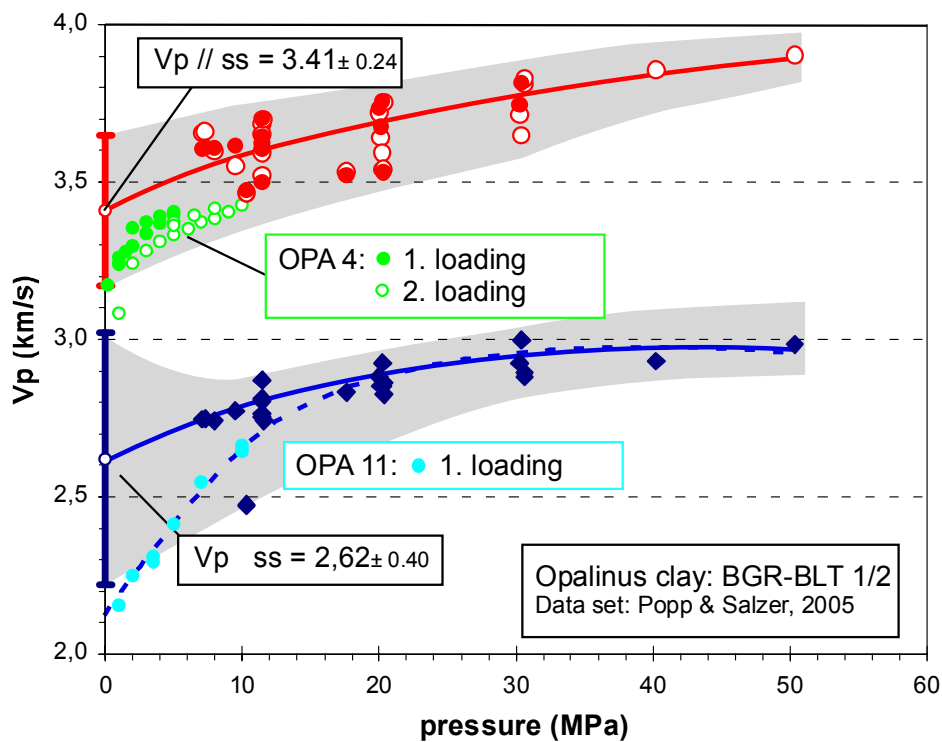


Figure 3-10. P-wave velocity variation during hydrostatic loading measured || (sample OPA4) and ⊥ to the bedding plane (sample OPA11) of Opalinus Clay, measured on cylindrical samples in the triaxial IfG-cell. For comparison the data obtained in the multi-anvil-apparatus are shown as dark blue and red symbols (Figure 2-7). In addition, the data ranges for low pressure measurements, given in Bock (2001), are included.



Table 3-3. Data sets from hydrostatic loading tests on Opalinus Clay with permeability measurements.

injection \perp to bedding		pressure range (MPa)	k_0 (m ²)	χ (1/MPa)
307/OPA Kon1	1. cycle	0 - 5	1,58E-17	0,54
307/OPA 11	1. cycle	0 - 10	4,27E-16	0,51
				0,52 ±0,02
injection \parallel to bedding				
307/OPA 1	1. cycle	0 - 5	6,68E-16	0,40
	2. cycle	0 - 5	3,32E-16	0,30
307/OPA 2	1. cycle	0 - 5	4,16E-16	0,13
307/OPA 4	1. cycle	0 - 5	1,30E-14	0,54
	2. cycle	0 - 10	1,14E-15	0,31
				0,33 ±0,15

Compared to permeability, P wave velocities are affected by hydrostatic pressure in the opposite direction. The velocity/pressure relations (Figure 3-10) exhibit a significant increase at pressures up to 10 MPa approaching a less steep almost linear trend at high pressures. The nonlinear part must be attributed to progressive closure of microcracks or pores whereas the quasi-linear trend is interpreted to reflect elastic matrix compaction (BIRCH, 1960; KERN, 1982).

Remarkably, as came out by the new measurements, the pressure dependent velocity increase is more pronounced for velocity measurements perpendicular to the foliation compare OPA 11) than parallel to it (compare OPA 4 both 1. and 2. cycle). This corresponds with the higher compaction resp. with the more efficient sealing processes as indicated by the pressure dependent permeability decrease observed in Figure 3-9.

3.2.3 Deviatoric loading

In order to investigate the effect of dilatant deformation on the hydraulic integrity we performed six compression tests at a constant strain rate ($\dot{\varepsilon} = 10^{-5} \text{ s}^{-1}$) after the hydrostatic compaction cycle. The applied confining pressures varied between 2.5 and 10 MPa, whereby four of the experiments were performed on samples with loading orientation 0° to the bedding and only two perpendicular to it (for details see Table 3-4).

Figure 3-11 presents a complete set of experimental data, which can be obtained during optimal measuring conditions (see discussion below) of a clay sample deformed at 3 MPa confining pressure with the loading direction parallel to the foliation. Therefore, the initial permeability is very high, in the order of 10^{-15} m^2 , which is obviously also due to some core disturbances during sample recovery and preparation.

Starting from hydrostatic conditions the deviatoric stress increases to ensure constant rate deformation. The slope of the stress-strain curve exhibits the characteristic transition from initial quasi-elastic (linear) behaviour to a curve with relatively large radius indicating typical strain hardening until failure at a strain of only $\sim 0.6\%$.

Table 3-4. Results from triaxial deformations tests in the Karman-cell of the IfG ($\dot{\epsilon} = 1 \cdot 10^{-5}$ 1/s).

Sample	Loading direction referred to foliation	p_c (MPa)	ϵ_{Bruch} (%)	$\sigma_{Diff-max}$ (MPa)	ϵ_{Dil}^{**} (%)	$\epsilon_{Vol-Min}^{**}$ (%)	σ_{Dil}^{**} (MPa)
307 / OPA 9	0 / US	10.0	0.77	39.8	0.79	-0.39	39.4
307 / OPA 2	0°	5.0	0.55	30.5	0.55	-0.24	30.5
307 / OPA 4	0° / US ^{*)}	3.0	0.55	28.2	0.51	-0.18	27.2
307 / OPA 1	0°	2.0	0.48	23.2	0.42	-0.11	22.6
307 / OPA 11	90° / US ^{*)}	10.0	1.60	28.3	1.56	-0.29	28.3
307 / OPA Kon 1	90° / US ^{*)}	3.0	1.48	23.7	1.44	-0.29	23.3

^{*)} Simultaneous crack monitoring with measuring V_p and V_s .

^{**)} Parameters (ϵ_{Dil} , $\epsilon_{Vol-Min}$; σ_{Dil}) referred to the minimum of the volumetric strain measurements, respective its relevancy as dilatancy indicator see discussion in the text

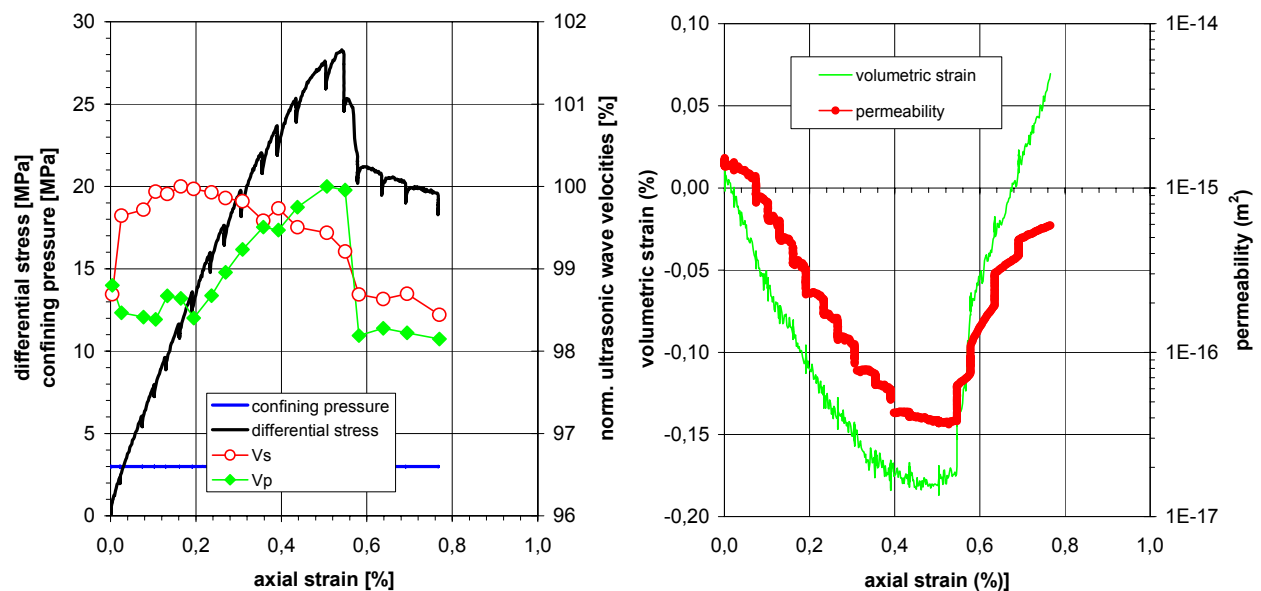


Figure 3-11. Differential loading of Opalinus Clay: exp. 307 / OPA 4 (perpendicular to the bedding) with simultaneous monitoring of V_p with $\sigma_1 \gg \sigma_2 = \sigma_3$. (left) P- and S-wave velocities; differential stress and confining pressure vs. axial strain. (right) pore space parameters (volumetric strain and permeability) vs. axial strain.

As evident from the experiment, the initial stage of deviatoric loading is characterized by a significant increase of P- (and S-wave velocities) respectively compaction as demonstrated by the transport parameters. Further triaxial deformation gives rise to a marked change, e.g. initial crack opening at around 60% of the failure strength, but this is only indicated by the shear wave velocity reacting in the opposite direction with a decrease. In contrast, P-wave velocity show no significant change and increases further indicating obviously overall compaction which is confirmed by the deformation induced decrease of volumetric strain and permeability.

[NF-PRO]



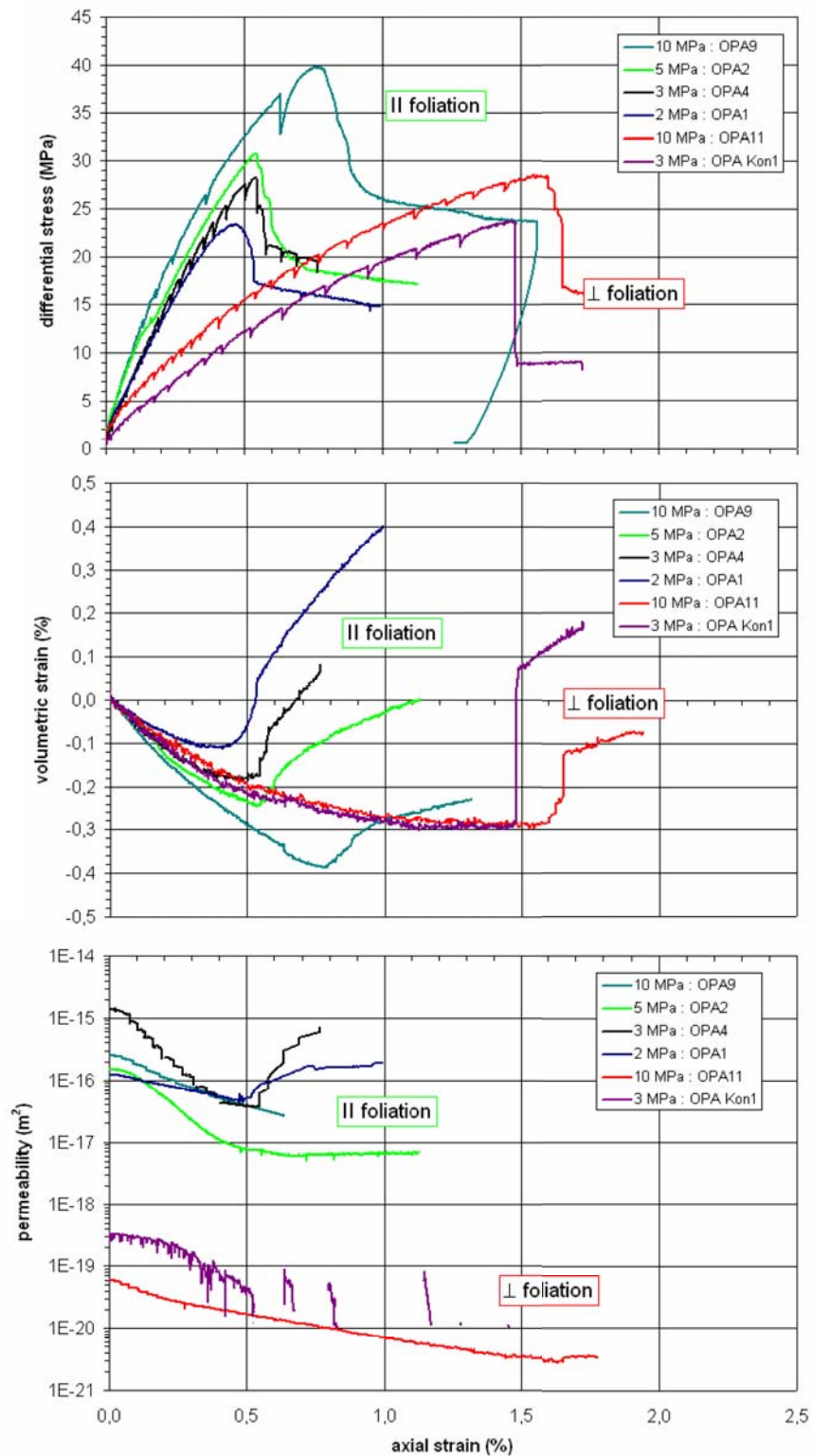


Figure 3-12. Summary of triaxial test results on Opalinus Clay in a confining pressure range between 2 and 10 MPa. Note the differences between both groups of loading direction and the well pronounced effect of increasing confining pressure.

Only directly before the failure also the latter parameters react in the reverse direction, e.g. a velocity drop is accompanied with a steep increase of both permeability and volumetric strain

[NF-PRO]

Report – Deliverable 4.2.15

Dissemination level : PU

Date of issue of this report : 01/10/07

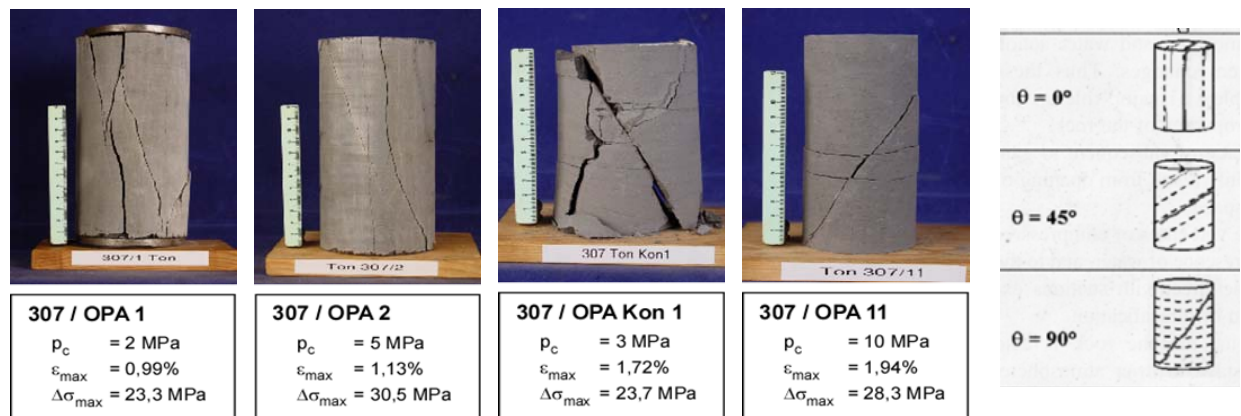


is measured. With further deformation a well distinguished post-failure stress plateau is reached.

These results of brittle deformation of Opalinus Clay were confirmed by the other experiments, whereby significant differences for the various loading directions were observed.

Generally, all experiments show the same physical parameter signature related to the measuring direction with strain: whereas P-wave and volumetric strain resp. permeability may indicate compaction until the failure in some cases shear wave velocities show a weak decrease at stresses in the order of 0.6 – 0.7 of the failure strength. It has to be mentioned that only in two cases it was possible to measure Vs with sufficient reliability due to overlapping damping effects.

The stress-strain curves depicted in Figure 3-12 nicely demonstrate the effect of increasing pressure resulting in higher strength and deformability. Remarkably, compaction effects are more pronounced for samples loaded perpendicular to the bedding, and also the deformability is higher, but the stiffness is lower.



taken from Vales et al , 2005

Loading parallel to foliation ($\theta = 0$) Loading \perp to foliation ($\theta = 90$)

Figure 3-13. Crack patterns of various samples with respect to their loading conditions referred to the bedding. For comparison also schematizations of the failure are included taken from VALES et al. (2004).

Examples of the deformed samples after failure are depicted in Figure 3-13, confirming that orientation of the prominent fracture planes strongly depend on the bedding which was also observed by other authors (e.g. VALES et al., 2004). More details of crack structures of a specimen deformed at $p_c = 3 \text{ MPa}$ with loading direction perpendicular to the bedding are presented in Figure 3-14. In accordance to Figure 2-12 two types of cracks can be distinguished:

- In axial compression a central shear plane is developed by sets of narrow-spaced open cracks which are aligned 45° to the axis of maximum stress. Due to movement along the shear planes en-echelon tension gashes are opened oblique to the shear direction so that local crack opening tends to align preferably parallel to the principal compressive strain axis.

[NF-PRO]



- Opened bedding planes (indicated by horizontal cracks) are due to the general decompaction after unloading the sample.

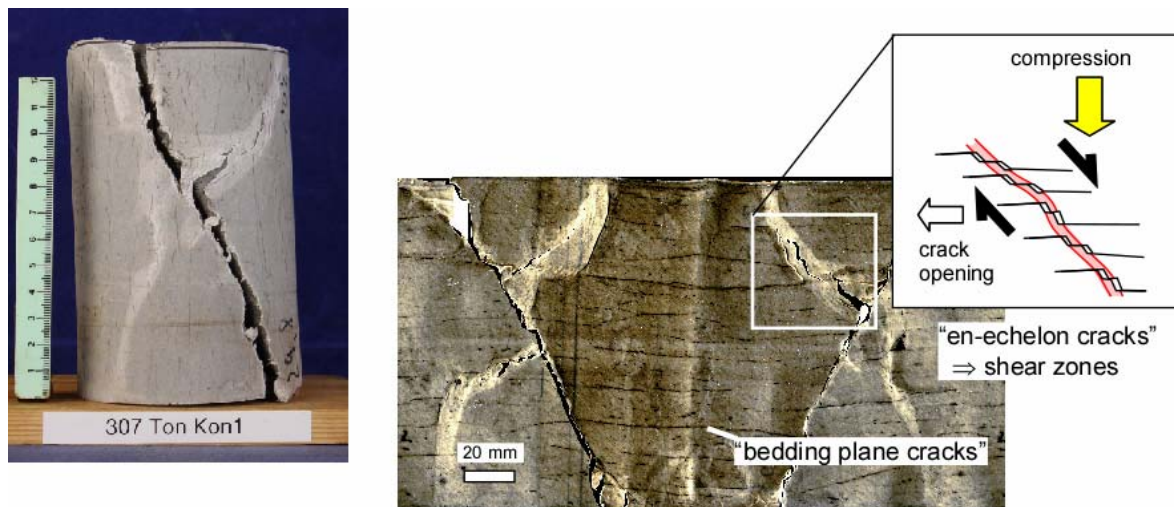


Figure 3-14. Shear failure of specimen 307 / OPA Kon 1: $p_c = 3$ MPa; $\epsilon_{max} = 1.72\%$; $\Delta\sigma_{max} = 23.7$ MPa); (left) sample after failure; (right) acetate peel of the sample surface with an inset of schematic en-echelon tension fractures in the shear zone.

3.3 Evaluation of the permeability / porosity relationship

As already demonstrated in chapter 3.2.3, simultaneous measurements of volumetric strain and permeability during deformation offer a simple estimate of the permeability / porosity relationship. Accordingly, the measured datasets are plotted in Figure 3-15. Due to the competing effects of initial sample disturbance and pressure induced compaction the starting conditions of the pore space in the triaxial tests are difficult to define, and, therefore, the initial porosity was set to be 16 %.

Remarkably two permeability / porosity ranges depending on the measuring directions referred to the foliation of the investigated samples can be discriminated. In addition, corresponding to loading induced compaction or the reverse, shear failure induced pore space opening, two contrasting permeability / porosity trends are obvious. In consequence, we have to conclude that up to now a comprehensive description of the anisotropic hydraulic transport behaviour of Opalinus Clay can not easily derived. Therefore, a simple approximation (e.g. as used by ZHANG & ROTHFUCHS, 2005 for forecast modelling of coupled hydraulical mechanical properties in the ventilation test at Mont Terri), as included in Figure 3-15, has to be treated as a rough estimate deduced from an expert judgement.

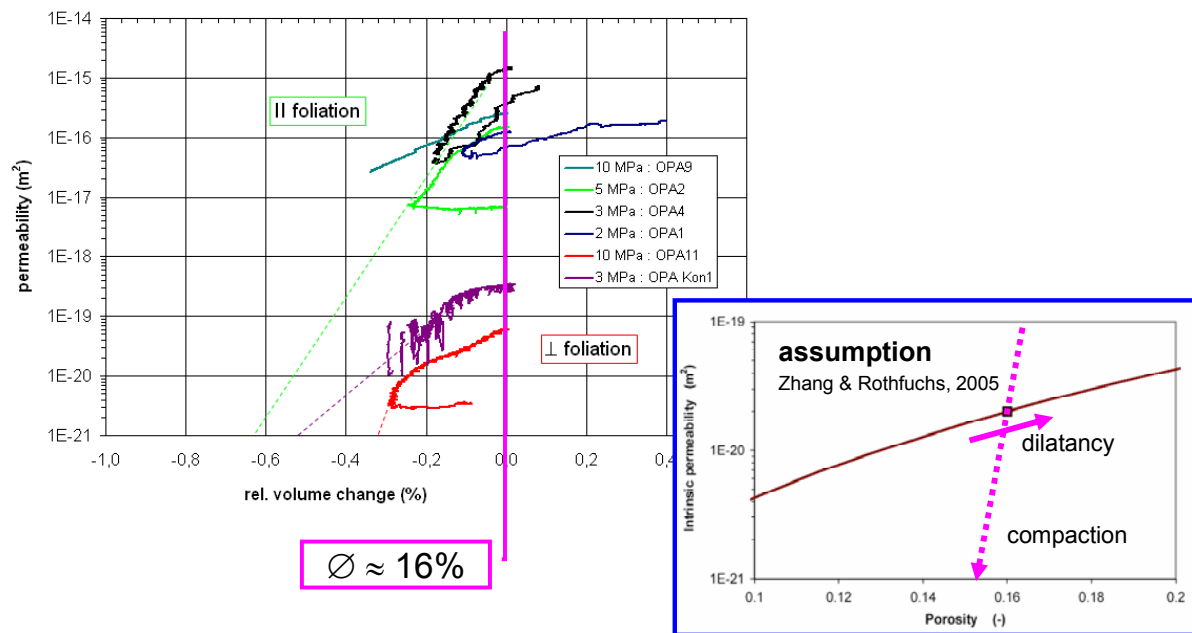


Figure 3-15. Experimental derived permeability / porosity relationships for Opalinus Clay as derived from triaxial strength testing with simultaneous measurements of volumetric strain and gas-permeability. The inset on the right side shows the assumption of Zhang & Rothfuchs (2005) used for pre-modelling of the ventilation test: Note the two different trends for compaction and dilatancy.

3.4 Evaluation of the strength data

Figure 3-16 summarizes data for failure strength and deformation induced changes of V_p and V_s from the various strength tests with different loading directions in comparison to literature results. Remarkable, the strength data sets for Opalinus Clay obtained by various authors (i.e. IfG data resp. taken from LUX et al., 2004) and with different equipments (i.e. deformation tests on cubic specimens: chapter 2.3.2 and cylindrical specimens: chapter 3.1.3) show only some weak scattering which convincible demonstrate the reliability of the test results.

The rock-mechanical test result clearly document that the strength of Opalinus Clay is sensitive to mean stress and the stress direction related to the bedding. When the stress direction is 45° to the bedding the data of LUX et al. (2004) show that the strength is low and only weakly affected by the confinement, but the things become more complicated for loading directions with 0° or 90° , which show a pronounced mean stress dependence:

- Whereas at uniaxial stress conditions failure stresses of samples loaded parallel to the foliation are significantly smaller than those of samples loaded perpendicular to the foliation, as clearly indicated by the UCS-values, the reverse becomes true with increasing confining pressure: $\sigma_{\text{failure} - 0^\circ\text{SS}} > \sigma_{\text{failure} - 90^\circ\text{SS}}$.

This behaviour corresponds nicely to experimental data obtained from the BGR experiments on argillaceous clay from Bure (M. NAUMANN, personal comm., see Figure 3-16). In addition, it's worth to note that the strength of the Bure material is obviously higher than for the Opalinus Clay from the Mont Terri-site.

[NF-PRO]

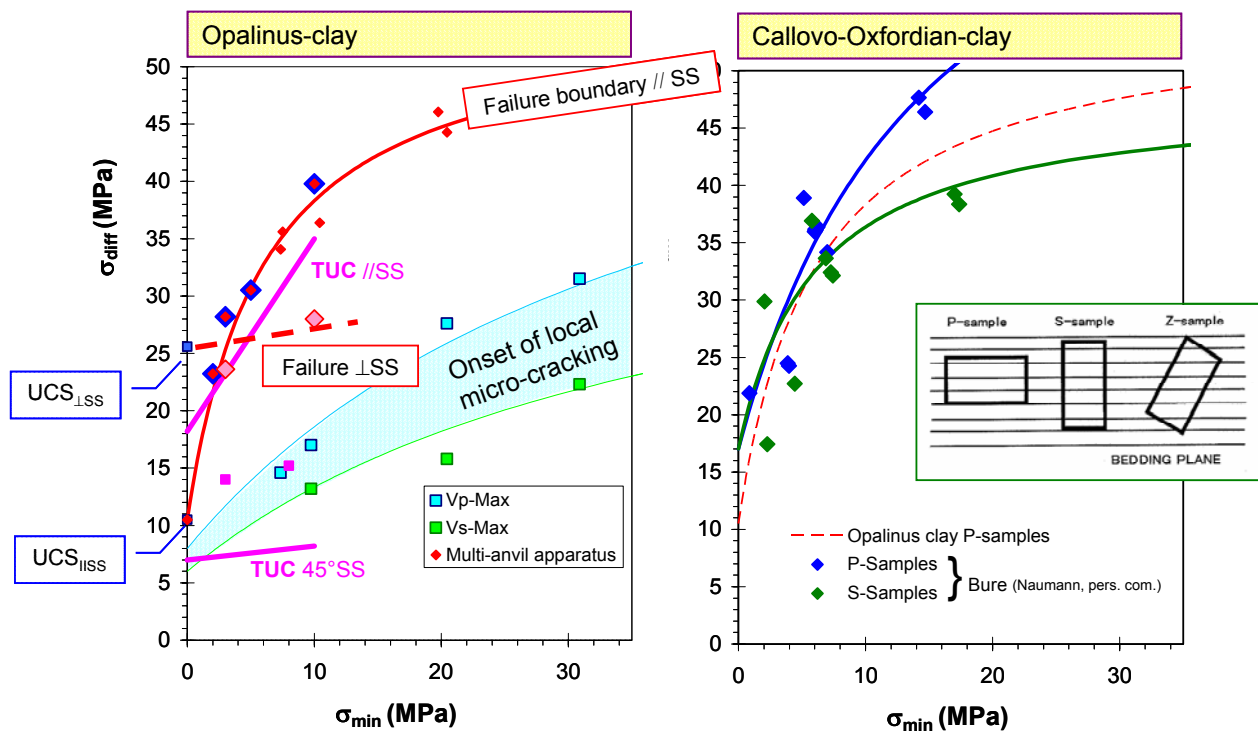


Figure 3-16. Strength and dilatancy boundary data sets for Opalinus Clay (left) and the Callovo-Oxfordian Clay from the Bure site (data from BGR) – Note the schematic orientations to the bedding: //SS = P-sample; 45°SS = Z-Sample; ⊥SS = S-sample.

3.5 Evaluation of the deformation induced-velocity changes

Experimentally derived ultrasonic velocity data during triaxial loading offer an important base for understanding the role of existing bedding planes in argillaceous clay for the overall deformation behaviour and, especially, the onset of micro-fracturing. However, it has to be mentioned that the spatial velocity distribution of p- and s-waves needs to be interpreted by both overlapping effects of primary intrinsic matrix anisotropy and stress induced oriented micro cracks, which is not a simple task.

In the argillaceous clays the shape fabric of clay minerals gives rise to a lattice preferred orientation as is documented by pole figures obtained by the x-ray texture measurements presented in Figure 2-4b. This texture effect results in a pronounced seismic anisotropy whereby velocities measured parallel to the foliation are significantly higher than perpendicular to it, as documented by experimental results measured in the multi-anvil apparatus (see chapter 2.3.2). Shear waves additionally show a pronounced shear wave splitting in the foliation.

Increase of confining pressure results in rock compaction as indicated by an increase of the measured seismic velocities, in particular perpendicular to the foliation due to the closure of bedding plane cracks respectively the lowered stiffness.

Loading in the dilatant stress domain gives rise to the generation and propagation of cracks, which induce a decrease of seismic wave velocities, and to increase of damage with strain. From microstructural investigations, it came out that the generated microcrack patterns are

[NF-PRO]

closely related to the bedding planes and, in addition, to the geometry of the applied stress system (i.e. Figure 3-13). Detailed microstructural analysis of the crack patterns documents the development of shear planes with en-echelon cracks with opening predominantly parallel to the direction of the minimum principal (lateral) stress. This means that the existing velocity anisotropy is overlapped by the complex crack geometry patterns.

Close inspection of the experimentally derived velocity versus strain relations at the initial stage of axial compression gives evidence that s-wave velocities start to decrease first, that is, at lower axial strain than the corresponding p-wave velocities, as documented in the chapters 2.3.2 and 3.2.3.

The differences between V_p and V_s suggest that shear waves are more sensitive to onset of initial flat micro cracks due to localized stress concentrations whereas progressive opening of cracks is required to affect P-waves. This phenomenon is simply due to the differences in wave propagation and particle motion, as illustrated in Figure 3-17.

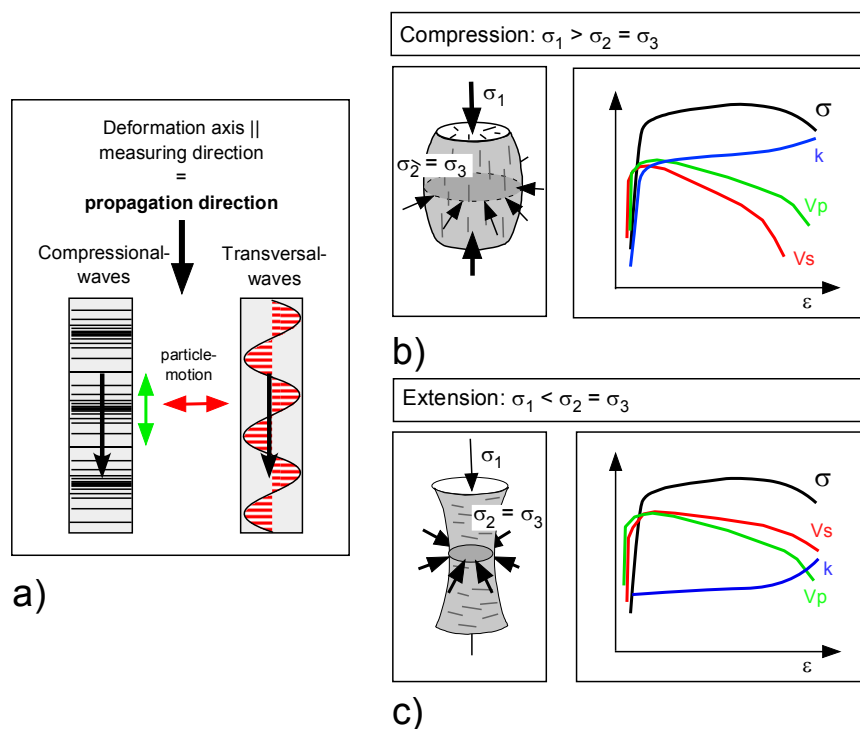


Figure 3-17. Schematic interpretation of crack patterns as indicated by deformation induced variations of V_p resp. V_s particle motion of P- and S-waves with respect to the propagation direction (a) and orientation of microfractures in axial compression (b) and axial extension (c) with respect to the principal strain axis (modified after POPP & KERN, 2000).

At stress conditions in the compression mode the long (low-aspect ratio) cracks are presumably aligned parallel to the unique deformation axis (σ_1). Widening of cracks (i.e. typically for en-echelon cracks as shown in Figure 3-14) is, therefore, parallel to the direction of particle vibration of the axially measured shear waves, whereas the reverse is true for longitudinal waves. In consequence, the sensitivity of shear waves measured parallel to the compressive

deformation axis is higher than longitudinal waves, and also V_s decreases more than V_p with proceeding deformation. The reverse is true for loading in the extension mode, or if the ultrasonic wave velocities are measured perpendiculars to the deformation axis. This has been confirmed by the measurements performed in the true-triaxial deformation apparatus (for details see chapter 2.3.2).

However, it has to be noted that the development of cracks controls the directional dependence of permeability as came out by triaxial tests on rock salt, reported by POPP et al. (2001).

3.6 Application of the dilatancy concept in argillaceous clay - discussion

The determination of the criteria "dilatancy boundary" is of predominant importance for an appraisal of barrier properties of solid rocks, because it could be used as safety criteria. The actual state of knowledge about the stress dependent onset of damage resp. dilatancy boundaries regarding argillaceous clay, mainly based on volumetric strain measurements, was summarized by BLÜMLING during the NF-Pro second training course in Cardiff (2005) as follows:

$\sigma_{\text{dam}} \approx 0.8 - 0.9 * \sigma_{\text{peak}}$	(Opalinus Clay)
$\sigma_{\text{dam}} \approx 0.9 * \sigma_{\text{peak}} - 13 \text{ MPa}$	(Callovo-Oxfordian – Carbonate-rich)
$\sigma_{\text{dam}} \approx 0.6 * \sigma_{\text{peak}} - 2 \text{ MPa}$	(Callovo-Oxfordian – Clay-rich)

However, from our feeling volumetric strain curves (in addition to permeability measurements) are only of limited use for detecting dilatancy in argillaceous clays, because they may be overlapped by the dominating compaction effect parallel to the bedding plane. Fortunately, the pronounced changes in the slopes (inversions) of the velocity versus strain curves at the initial stage of deformation offer an alternative concept for detecting microcracking because they convincingly indicate a strain-related transition from compaction to dilation. The measured stress values as detected by the various physical parameters, V_p or V_s , are plotted in Figure 3-18 in a differential stress versus confining pressure diagram up to pressures of 35 MPa.

Despite the rare data it can be clearly seen, that at stresses significantly lower than the failure strength the acoustic parameters react.

This observation corresponds nicely to the dilatancy concept (CRISTESCU & HUNSCHE, 1998) which represents an synoptic analysis and prediction of the coupled thermal, mechanical, and hydraulic processes in rocks undergoing various states of stresses (Figure 3-19). The so-called dilatancy boundary separates the non-dilatant compaction domain, where mechanical healing is possible from the dilatant domain where damage occurs at stresses significantly below the failure boundary. Depending on the state of stress (deformation at higher deviatoric stresses or reduction of the minimal stress favours the development of damage) rock deformation is associated with an increase of permeability resp. a loss of hydraulic barrier integrity. In consequence, if the dilatancy criterion is fulfilled no critical deformation state can be reached.

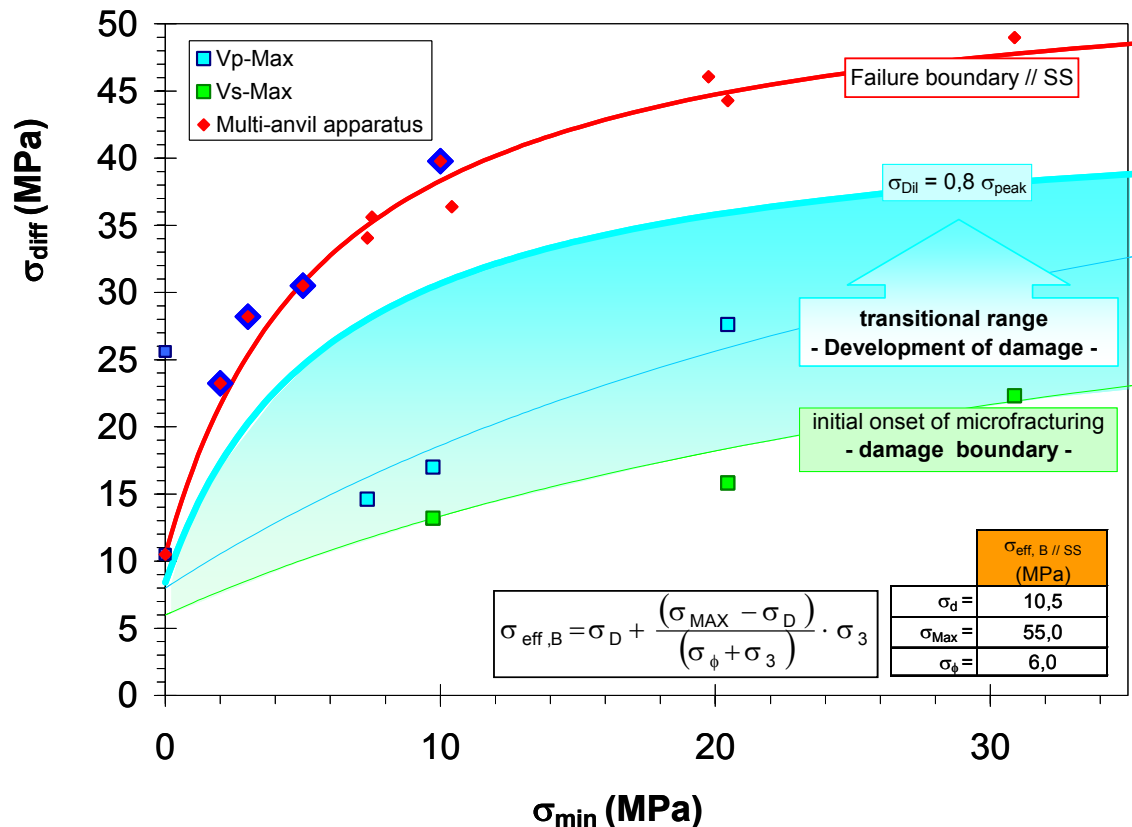


Figure 3-18. Failure and dilatancy resp. damage boundary curves obtained by the characteristic behaviour of various measured parameters: short-term triaxial compression tests on cylindrical and cube shaped Opalinus Clay specimens with various bedding plane orientations.

However, due to fact that onset of micro-cracking and development of macroscopical dilatancy correspond to different stress states the classical dilatancy concept has to be extended by two stress-damage criterions:

- The lower curve of Vs-reversals defines a boundary separating the dilatancy domain from the domain where no micro cracking occurs \Rightarrow **initial damage boundary**.
- The boundary of Vp-reversals lies between the failure and the Vs-boundary indicating a higher stage of damage, which corresponds to the **dilatancy transition field**.

Because of the raw data sets in the current state only a rough estimate the following stress limits can be defined:

$$\begin{aligned} \sigma_{\text{initial damage}} &\approx 0.5 - 0.6 \cdot \sigma_{\text{peak}} && \text{(Opalinus Clay)} \\ \sigma_{\text{dilatancy}} &\approx 0.8 - 0.9 \cdot \sigma_{\text{peak}} && \text{(Opalinus Clay)} \end{aligned}$$

In summary, the validity of the dilatancy concept also in argillaceous rocks has been experimentally confirmed by the associated measurements of p- and s-wave velocities, indicating occurrence of micro cracking at stress levels significantly lower than the failure boundary- However, due to the rock anisotropy it's application is much more complicated and, in addition, as came out by chapter 3.3, a simple coupling between mechanical (i.e. damage) and hydraulic properties is not possible.

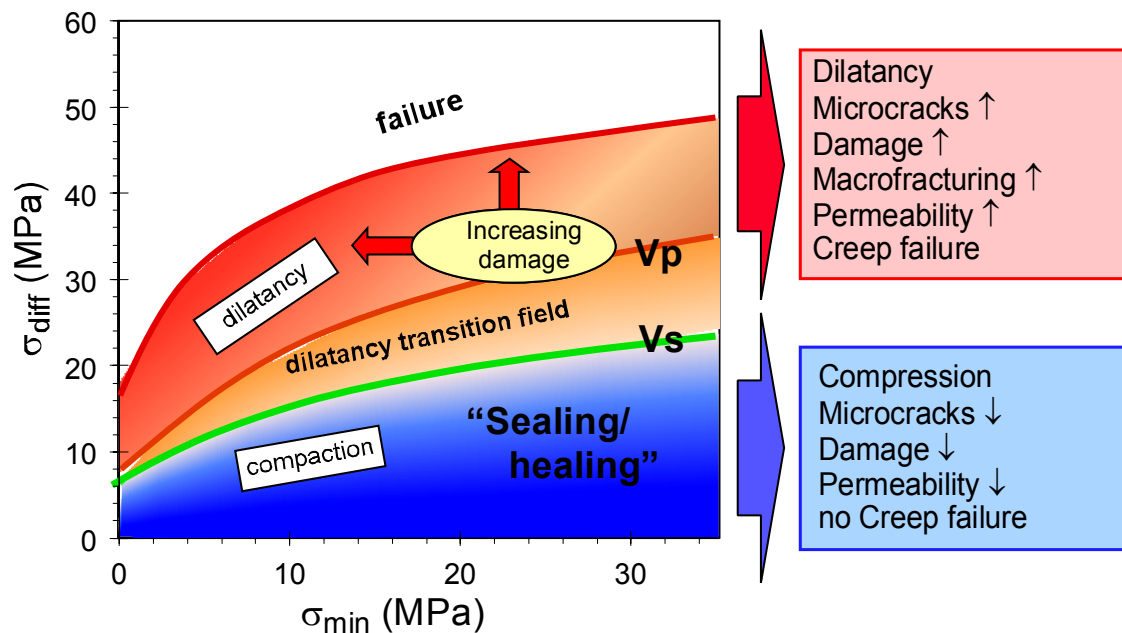


Figure 3-19. The dilatancy concept for Opalinus Clay: schematic diagram (modified after the concept for salt, e.g. Cristescu & Hunsche, 1998). Note the “dilatancy transition field”, which indicates the haziness for detecting the onset of micro crack opening due to the different sensitivity of V_p and V_s .

4 Direct shear tests on bedding planes

Bedding planes in argillaceous rocks are probably, in addition to rock joints and other geomechanical discontinuities, the clearest example of existing interfaces.

For the mechanical behaviour of interfaces the relevant variables are stress traction vector with one normal component and one tangential in a simple 2-dimensional stress field (or two tangential in 3D), and the conjugate "strain" variables are the corresponding relative displacements. However, such stress conditions can be only realized in direct shear tests, which are therefore of urgent need to reproduce slip between various materials. Aiming on a sufficient description of the mechanical bedding strength, at least 15 shear tests have been performed with various orientations referred to the bedding during the course of the NF-Pro. Preliminary results were already summarized in IFG (2005b). Based on additional experimental results the new developed MINKLEY-shear model was applied for describing the strength behaviour.

4.1 Test Arrangement

The slip criterion for a geomaterial (or for a plane of weakness in the strata, e.g. bedding planes), is referred in literature to many different terms: shear strength, failure criterion, yield criterion, or Coulomb criterion. It is expressed often as an equation that stipulates the maximum permissible shear stress along the slip surface being analyzed. The simplest linear form, the linear MOHR-COULOMB criterion, may be written as

[NF-PRO]

$$\tau_{\text{MAX}} = c' + \sigma'_n \cdot \tan \varphi' \quad (4-1)$$

Here, τ_{MAX} = the maximum shear stress that the plane can sustain before slip; c' = the cohesion of the rock; σ'_n = the normal effective stress across the slip plane; and φ' the internal friction angle.

The material parameters c' and φ' are determined empirically from testing.

For realization of required shear tests a modern shear test system is available at the IfG (Figure 4-1). A detailed description of this device is given in BLUEMEL& POETSCH (2003).

The loading frame consists of a two-axle experimental setup with vertical and horizontal stress initiation, a platform for shear test in a shear box, and a servo-hydraulic control unit for two channels (vertical and horizontal). Both can be managed force or displacement controlled. The frontal part (right) is an extremely stiff four-columned test frame for fixing and vertical loading of the two-part shear box by the upper hydraulic cylinder (up to 500 kN axial load).

Horizontal motion is guided by a precision linear bearing, which is designed for low friction and a single degree of freedom (translation only). The horizontal force is generated by a laterally positioned horizontal cylinder (- 250 kN pressure; - 160kN tension). The upper part of the shear box is fixed by a horizontal housing that enables yet a twisting of approx. 2° around the horizontal axes referring to the shear midpoint. While a vertical load acts to the whole shear box the lower box can be horizontally displaced under load.



Figure 4-1. The MTS – shear test system (model 816), available at the IfG.

The LVDT's are positioned at the initial specimen joint shear plane in multiple locations (4 vertical and 2 horizontal LVDT) which guarantees that the dilatancy, the shear displacement and the rotations can accurately be measured.

A sufficiently stiff fixing of the specimens is a prerequisite for an exact determination of shear resistance. Therefore, first of all the specimen is orientated in a position where the line of action of the shear force (τ_T) is on the investigated interface and the line of action of the nor-

[NF-PRO]

Report – Deliverable 4.2.15

Dissemination level : PU

Date of issue of this report : 01/10/07



mal stress (σ_n) is perpendicularly to that plane. Consequently both shear boxes will be filled in succession with high-strength anchor cement mortar resp. hydrostone. Thereby an opening of around 20 mm remains that enables the shear test of the fixed specimen.

Just before the shear test a consolidation (preload) of the test specimens in the shear box is done by a cyclic increasing of the normal stress (σ_n) perpendicular to the interfaces to reduce installation-dependent subsidence.

4.2 Experimental results

Various sample blocks with dimensions of around 100 mm x 100 mm x 200 mm and different orientations to the bedding have been prepared from the Opalinus Clay cores sampled in Mont Terri (see chapter 3.1.1), which were fixed by mortar in the shear box.

At least, 15 multiple-step shear tests along bedding were performed in σ_n -range between 0.25 and 5.5 MPa loaded perpendicular or parallel to the bedding which are summarized in Table 4-1.

Table 4-1. Results from shear testing II to the bedding. Note the different displacement rates of shear tests performed at $\sigma_n = 3$ MPa.

Sample	σ_n (MPa)	τ_{MAX} (MPa)	Displacement rate (mm/s)
307-SV9	0,25	0,62	0,002
307-SV1	0,5	0,94	0,002
307-SV2	1	1,33	0,002
307-SV4	2	1,59	0,002
307-SV5	3	2,01	0,002
307-SV12	3	1,97	0,002
307-SV13	3	2,25	0,002
307-SV8	4	2,71	0,002
307-SV11	5,5	2,90	0,002
307-SV14	3	2,47	0,02
307-SV15	3	1,65	0,00004

Principally, the test realization comprises three steps (as shown exemplary in Figure 4-2):

For characterisation of the mechanical bedding plane behaviour normal stress is applied with certain value, and then kept constant while shear relative displacement is applied to the joint sample. The measured values include shear stress and normal relative displacement, in addition to dilatancy, e.g., compaction or up-gliding corresponding to displacement in the direc-

tion of σ_n . The test is continued in two steps with different values of normal stress focusing on the residual strengt.

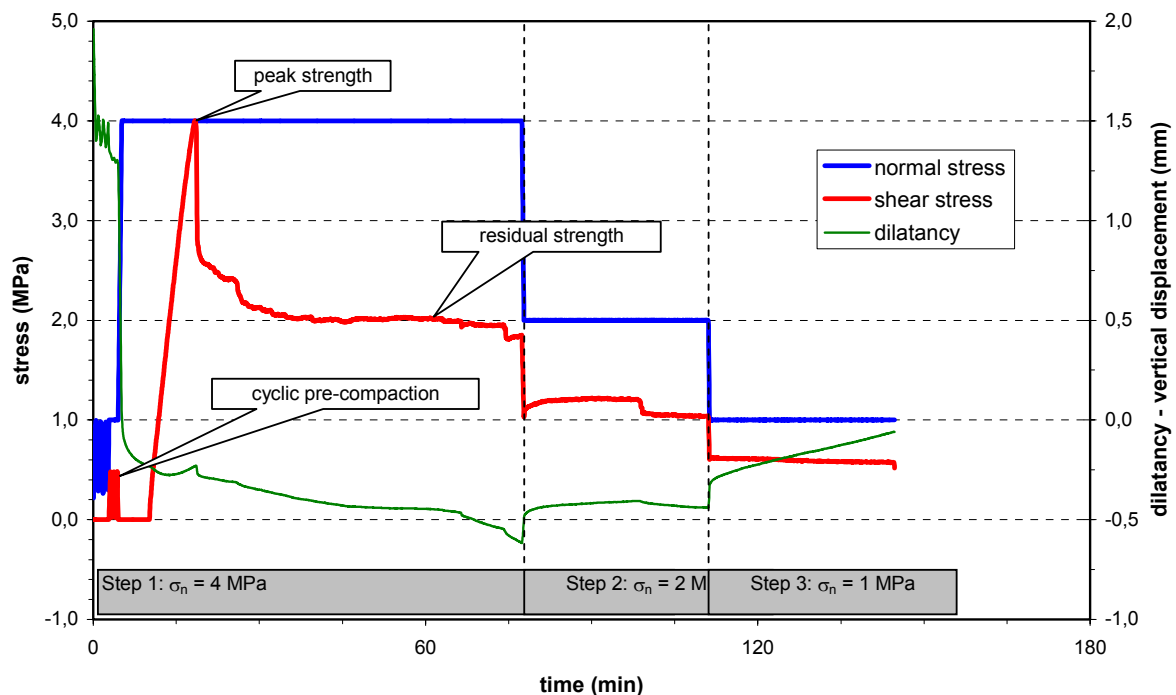


Figure 4-2. Direct shear test on Opalinus Clay sample (OPA 307-SV3: $\sigma_n = 4$ MPa) sheared parallel to the bedding with $\Delta s/\Delta t = 0.002$ mm/s ($\sigma_n: 90^\circ$ to bedding plane).

To illustrate the influence of increasing σ_n results from the various shear tests performed parallel to the bedding are summarized in Figure 4-3 as shear strength and dilatancy diagrams, each plotted vs. lateral displacement. The following results are obtained:

- Shear test curves (Figure 4-3a):

Shear stress usually grows in elastic manner up to a peak and then drops down to a residual value. Peak and residual values coevally become higher with increasing applied normal stresses but the ratio between them decreases. Regarding reliability of the data it has to be mentioned that although 3x repetition of the experiments at $\sigma_n = 3$ MPa only shows some weak scattering (in the order of ± 0.15 MPa) due to the complex morphology of bedding planes, as depicted in Figure 4-4, the experimental results can considerably vary if the bedding planes are not exactly horizontal oriented.

- Dilatancy curves (Figure 4-3b):

Due to the surface roughness and asperities (Figure 4-4), a bedding plane tends to dilate upon shear, although this effect tends to level off after certain amount of prescribed shear displacement, and is lower for higher normal stress. Remarkably, in Opalinus clay dilatancy effects will not only diminish but also disappear at normal stresses $\sigma_n > 5$ MPa, as can be deduced from the inset in Figure 4-3b.

With respect to the in-situ-conditions, additional shear tests were performed at $\sigma_n = 3$ MPa with different displacement rates (i.e. 0,02 – 0,002 – 0,00004). They clearly indicate that the shear properties are reduced if lower shear rates are applied (Figure 4-5).

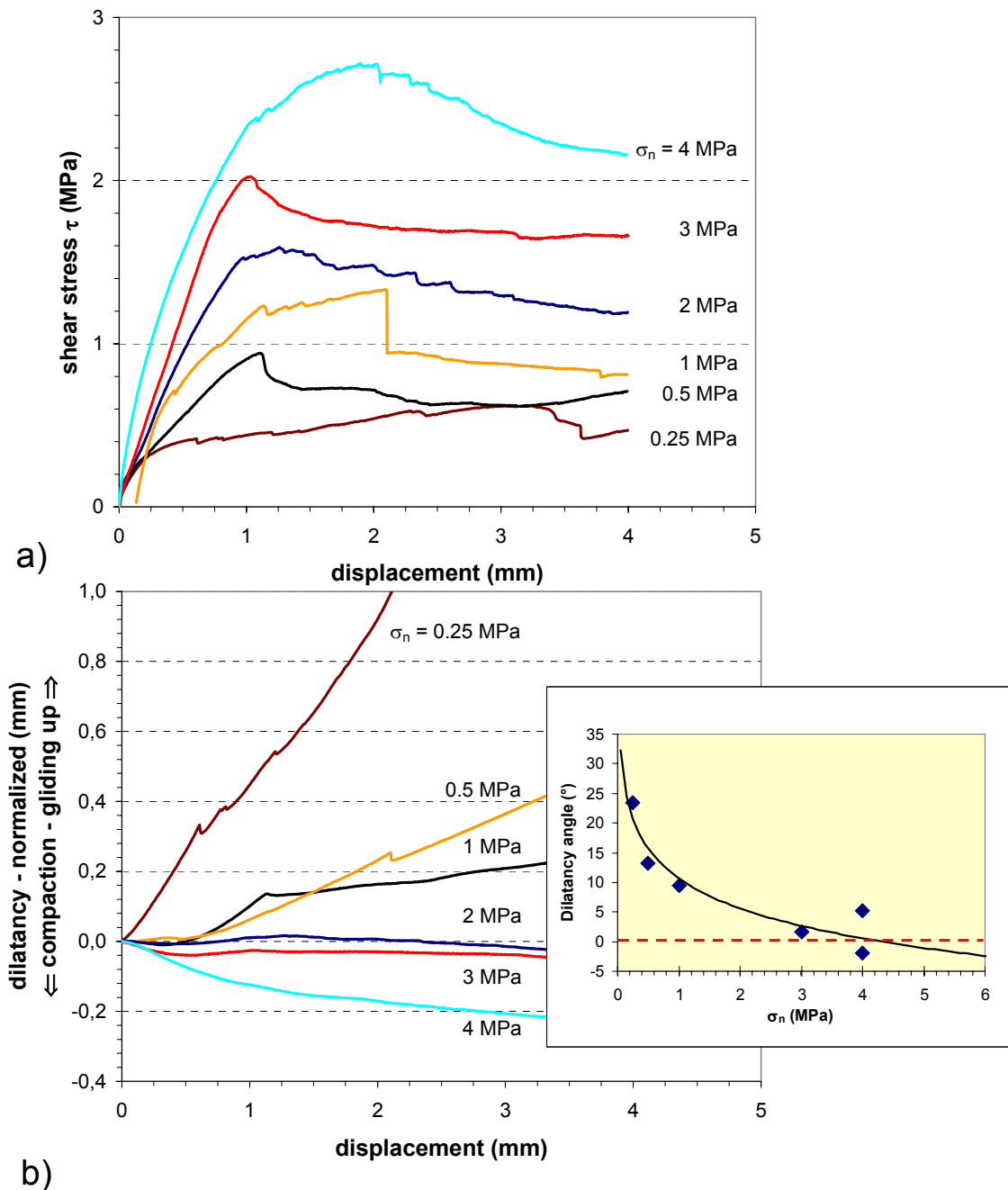


Figure 4-3. Characterisation of the shear strength behaviour of bedding planes in Opalinus Clay for various normal stresses. a) shear stress vs. displacement; b) dilatancy vs. displacement (relative dilatancy, referred to the last dilatancy value before beginning with shearing). The inset shows the variation of the dilatancy angle vs. σ_n , as derived from the respective dilatancy curves in (b).

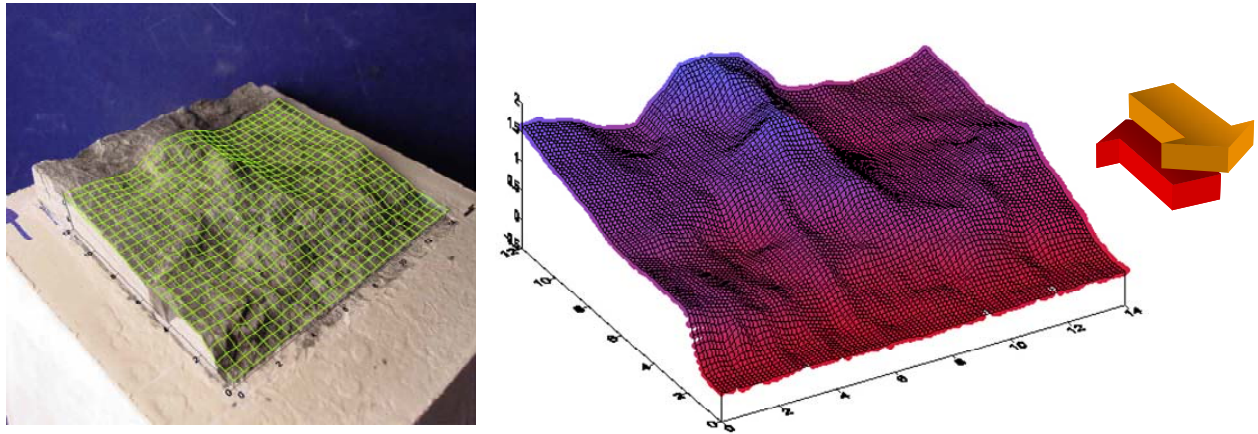


Figure 4-4. Representation of the asperities and roughness of a sheared bedding plane of Opalinus Clay by a 3D-contour model.

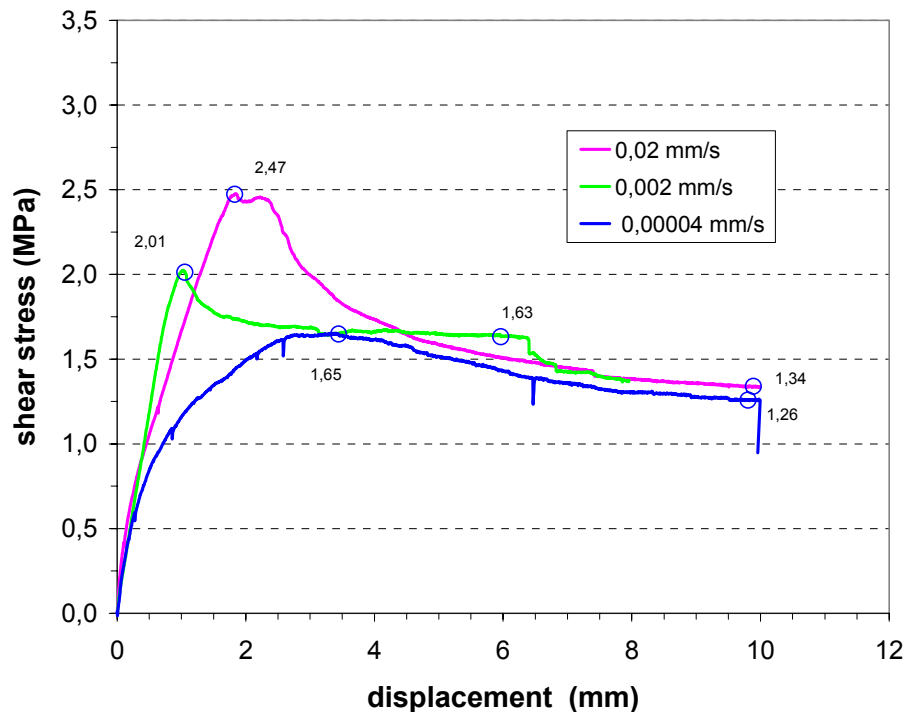


Figure 4-5. Shear strength behaviour of bedding planes in Opalinus Clay for various displacement rates at $\sigma_n = 3$ MPa

4.3 Evaluation of Shear Test Results

In a conventional way, shear stress peaks and residual values of shear stress obtained in single experiments are represented against normal stress, leading to open envelopes of the MOHR-COULOMB type (compare Figure 4-6). As expected, no cohesion exists for samples which are already sheared (residual strength); that means the tangents break through the zero point of the scale (in the bound of accuracy of measurement), whereby, the angle of residual friction is roughly the same. The estimated shear strength data determined via a

[NF-PRO]

regression analysis from the single tests according to equation (4-1) are for $C \approx 1$ MPa and for $\varphi \approx 21^\circ$. They correspond fairly well to data given by BOCK (2001; see Table 4-2).

Table 4-2. MOHR-COULOMB strength parameters of Opalinus Clay for bedding planes, as deduced from laboratory triaxial tests loaded 45° to the bedding (after BOCK, 2001).

n	Type of sample	Failure parameter of bedding planes	References (see Bock, 2001)
22	45° to bedding plane (Z)	$c_z' = 1$ MPa $\varphi_z' = 23^\circ$	TN 98-57 TN 98-55 TN 99-35

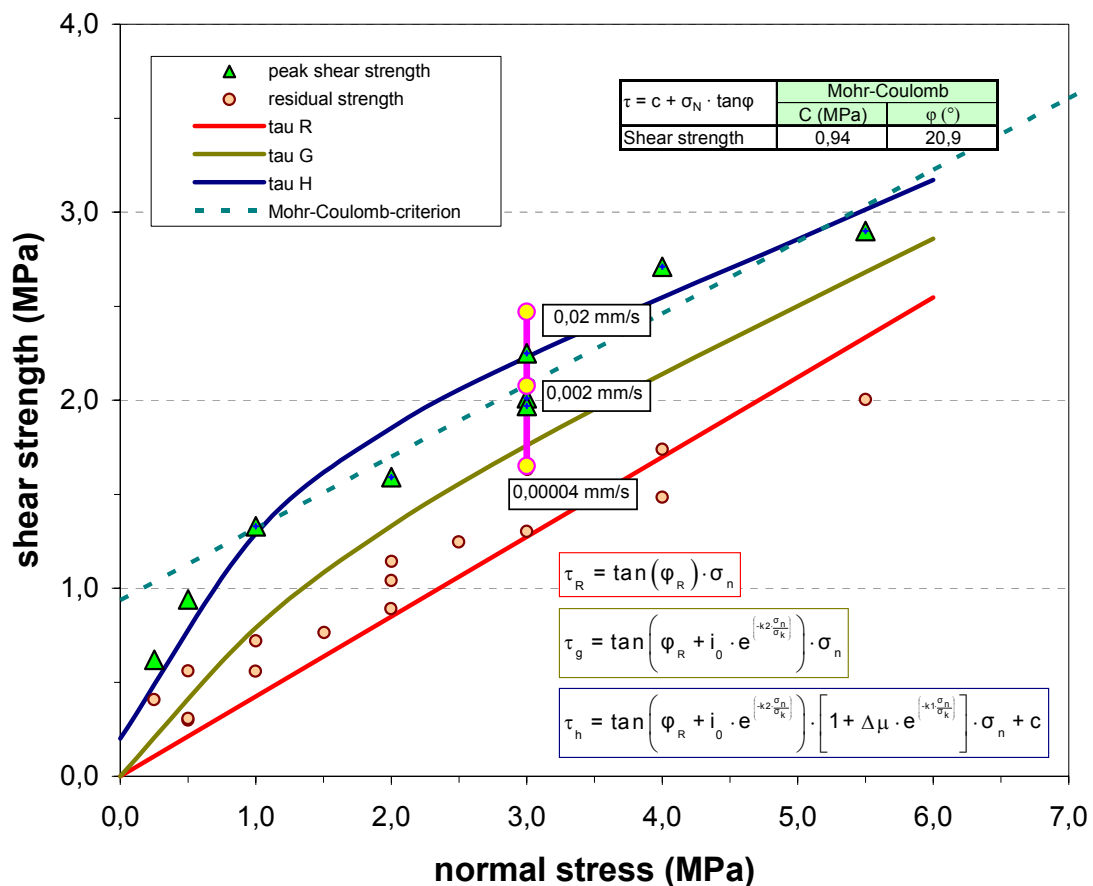


Figure 4-6. Shear strength of Opalinus Clay vs. σ_n . The various model curves of the new MINKLEY-shear model are presented in comparison to a MOHR-COULOMB criterion.

However, it can be seen that loading conditions for $\sigma_n < 1$ MPa are not realistically considered because in this part the curve behaves strongly non-linear. In addition, as documented by Figure 4-5 the shear strength behaviour of Opalinus clay clearly depends on the shear rate. This means that the classical MOHR-COULOMB concept which covers only static loading

may not allow a sufficient representative description of dynamic processes occurring during excavating a drift in clay formations.

Recently, MINKLEY (e.g. MINKLEY & MÜHLBAUER, 2007) developed a new shear model for bedding planes or contact interfaces, which implies the displacement-dependent and the velocity-dependent strength softening. It bases on the concept of CUNDALL & LEMOS (1990). The essential features of the shear model are:

- Dependence of the adhesive friction coefficient on the displacement rate of the shear process;
- The shear stress versus shear displacement curve approaches a “target” shear strength of the bedding or contact plane;
- The “target” shear strength remains constant until the softening region is reached, then it decreases with the progressing shear displacement.

Because this approach is assumed to provide a better understanding and contribution to a wider spectrum of the loading conditions the necessary parameters were derived on the existing database.

4.3.1 The Minkley-shear model

The new developed shear model is graphically represented in Figure 4-7. In the incremental formulation, the shear model can be described as follows. For the relationship between normal loading and normal displacement we use:

$$\Delta\sigma_n = k_n \cdot \Delta u_n \quad (4-2)$$

where k_n is the normal stiffness and Δu_n is the normal displacement between the joint surfaces.

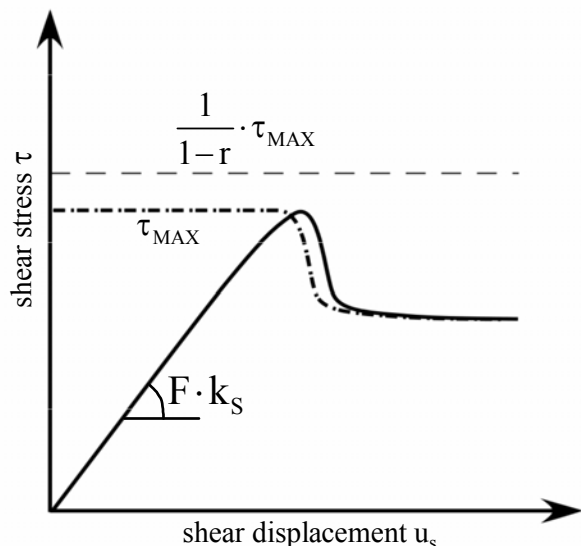


Figure 4-7. Shear model with strength softening.

The model responds to the shear loading with an irreversible non-linear behaviour. The shear stress increment is calculated as follows:

$$\Delta\tau = F \cdot k_s \cdot \Delta u_s \quad (4-3)$$

Here, k_s is the shear stiffness and Δu_s is the shear displacement parallel to the shear plane.

The factor F which reduces the slope is a function of the distance between the current shear stress τ and the peak shear strength τ_{MAX} :

$$F = 1 - \frac{\tau}{\tau_{MAX}} \quad (4-4)$$

When taking into account the adhesive friction which is of essential importance for the bedding planes or contacts, the shear strength is found to be:

$$\tau_{MAX} = \mu \cdot \sigma_n + c \quad (4-5)$$

with the friction coefficient:

$$\mu = \mu_K (1 + \Delta\mu) \quad (4-6)$$

which consists of the coefficient of the kinetic friction:

$$\mu_K = \tan \left(\phi_R + i_0 \cdot e^{-K_2 \frac{\sigma_n}{\sigma_k}} \right) \quad (4-7)$$

and the coefficient of the adhesive friction:

$$\Delta\mu = \Delta\mu_{vel} \cdot e^{-K_1 \frac{\sigma_n}{\sigma_k}} \quad (4-8)$$

Here are: c = cohesion; ϕ_R = angle of residual friction; i_0 = upslide angle; σ_k = compressive strength in the contact area; and k_1, k_2 = curvature parameters.

The effects of the kinetic and the adhesive friction components are proportional to the normal loading σ_n on the bedding plane. The cohesion diminishes only during very quick slide processes, whereas during a quite slow shear process the cohesive forces are maintained due to the specific characteristics of the clay which are covered by the rules of the physics of interfaces.

The dependence of the friction on the velocity v of the active shear process is represented by the following function:

$$f_{vel}(v) = \frac{1}{2} \left(1 + \tanh \left(b_s \cdot \log \frac{v}{v_K} \right) \right) \quad (4-9)$$

Accordingly, the velocity-dependent extent inside the adhesive friction coefficient can be expressed by:

$$\Delta\mu_{vel} = \frac{\mu - \mu_K}{\mu_K} = \Delta\mu_{MAX} \cdot f_{vel} \quad (4-10)$$

Besides the velocity-dependent shear behaviour also a strength softening that depends on the passed shear displacement has been taken into consideration, in the developed shear

model. As soon as the peak shear strength is approached, a reduction of the adhesive friction component occurs which depends on the plastic shear displacement. When the maximum shear strength τ_{MAX} has been approached up to a certain level r which must be preset, shear softening occurs if the following relationship is valid:

$$\tau \geq (1-r) \cdot \tau_{MAX} \quad \text{or} \quad F \leq r \quad (4-11)$$

The reduction of the adhesive friction along the shear displacement in incremental formulation follows the relationship:

$$\Delta\mu_S^p = -\Delta\mu_{vel} \cdot \frac{\Delta u_s^p}{L1} \quad (4-12)$$

where the increment of plastic shear displacement is defined by:

$$\Delta u_s^p = (1-F) \cdot \Delta u_s \quad (4-13)$$

The shear parameter $L1$ determines the steepness of the shear stress drop in the post-failure region. With increasing shear displacement the peak shear strength will be passed, furthermore, the upslide angle i_0 is lowered to reproduce the abrasion process resulting in a reduction of the unevenness between the joint faces and, additionally, mylonitization.

The difference between the present shear strain and the shear strain to reach the residual shear strength plateau of smoothed shear planes by abrasion is described by the parameter $L2$. For the reduction of the upslide angle in incremental form applies:

$$\Delta i = -i_0 \cdot \frac{\Delta u_s^p}{L2} \quad (4-14)$$

The incremental equations correspond to an exponential reduction of the adhesive friction component and the upslide angle during proceeding shear displacements on the bedding or contact plane in the post-failure state.

The effective dilatancy angle i is calculated as follows:

$$i = \arctan \frac{\tau}{\sigma_n} - \arctan \mu_K \quad (4-15)$$

Finally, the residual strength is:

$$\tau_R = \tan(\varphi_R) \cdot \sigma_n \quad (4-16)$$

and the maximum shear strength τ_{MAX} can be expressed with:

$$\tau_{MAX} = \tan \left(\varphi_R + i_0 \cdot e^{\left(\frac{-k2 \cdot \sigma_n}{\sigma_k} \right)} \right) \cdot \left(1 + \Delta\mu \cdot e^{\left(\frac{-k1 \cdot \sigma_n}{\sigma_k} \right)} \right) \cdot \sigma_n + c \quad (4-17)$$

4.3.2 Application to shear strength of bedding planes

The necessary model parameters were deduced from the data evaluation as depicted in Figure 4-6 and are summarised in Table 4-3. For testing the reliability of the new shear model we recalculated experimental shear tests in a simple 3D-geometry according to the shear test arrangement, as schematically depicted in Figure 4-8, using the numerical modelling code *3DEC* of ITASCA.

Figure 4-9 (left part) shows the modelled stress - deformation curve during the whole shear sequence. The modelled curve reveals the main characteristics, which are the nonlinear stress-deformation behaviour during the initial loading phase as well as the significant stress drop during achieving the residual strength. Coevally with increasing normal stresses, the dilatancy (Figure 4-9, right part) is heavily depressed.

Looking in more detail, especially the stress strain curves at $\sigma_n \leq 1$ MPa display some differences, i.e. the simulated strains until the peak strength are significantly lower than measured but the peak strength itself corresponds fairly well. But compared to the measured strength it could be stated, the modelled values reach the same order of magnitude as the measured ones. In addition, it is quite evident, that the strain-hardening behaviour rises with increased normal stresses until the peak strength is reached, and the level of the post-failure stress drop reduces

More difficult is the reproduction of the dilatancy curves because in the lab test we did not observed a clear plateau of residual dilatance as finally approached in the simulations. However, inspection of the sheared samples revealed that mostly a weakly dipped ramp with a complex morphology is developed due to the limited cross section which is sheared (Figure 4-4). Taking such scaling effects and lithological variations of shear planes into account we can conclude that laboratory test results and numeric recalculations are obviously in a good agreement.

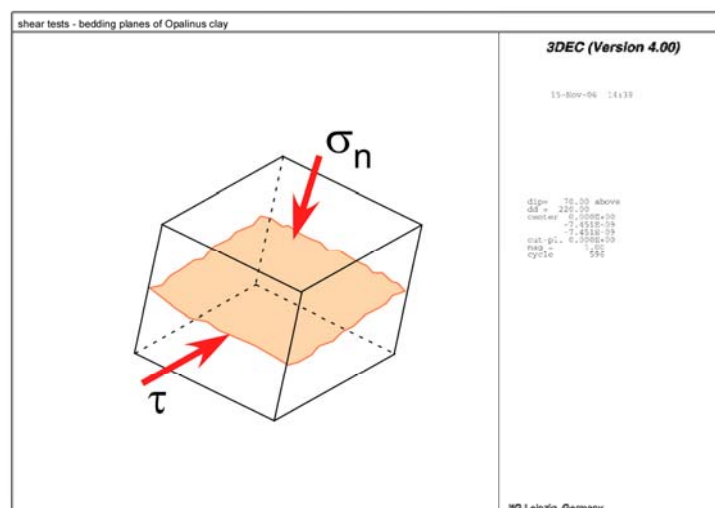


Figure 4-8. Schematics of the *3DEC*-simulation of shear tests on the bedding planes of argillaceous clay.

Table 4-3. Shear model parameters based on the data evaluation depicted in Figure 4-6 for modelling single shear tests on bedding planes of Opalinus Clay.

parameter	symbol	value	unit
residual friction angle	ϕ_R	23	deg
upslide angle	i_0	22	deg
compressive strength contact area	σ_K	2.2	MPa
curvature parameter 1	k1	1.0	
curvature parameter 2	k2	0.8	
cohesion	c	0.2	MPa
maximum adhesive friction coefficient	$\Delta\mu_{MAX}$	0.6	
softening distance 1	L1	0.0005	m
softening distance 2	L2	0.003	m
distance parameter	r	0.08	
velocity factor	b_S	1.2	
critical shear velocity	v_K	0.00001	mm/s
shear stiffness	k_S	10	GPa/m
normal stiffness	K_n	8	GPa/m

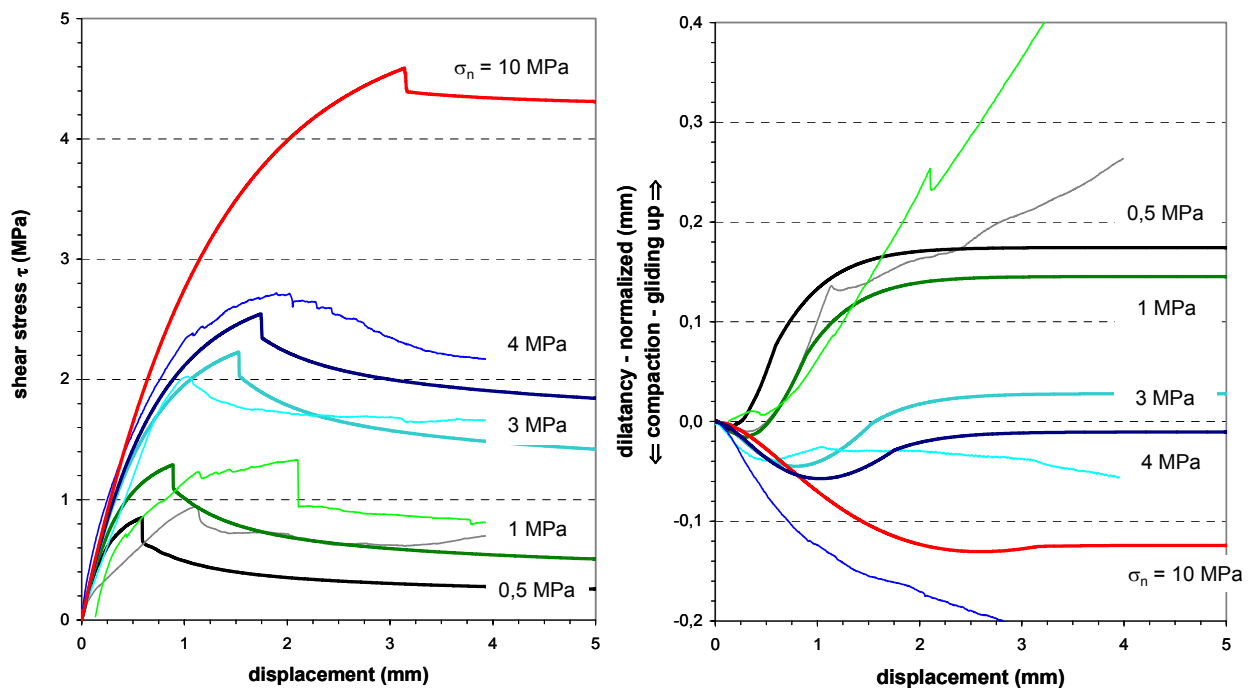


Figure 4-9. Numerical simulations of shear tests on Opalinus Clay at various normal stresses σ_n (using the parameters given in Table 4-3) compared with experimental lab test results in a test range of $\sigma_n = 0.5 - 4$ MPa – deformation rate = 0.002 mm/s. (left) Stress - strain curves. (right) Dilatancy -

strain curves. The weakly coloured and thin curves represent the experimental data. In addition, simulated data at $\sigma_n = 10$ MPa are included.

5 Modelling

5.1 Objectives and modelling concept

This part describes preliminary results of numerical modelling for simulating the development of EDZ during excavating a drift in the Opalinus Clay formation at Mont Terri. The aim is not to reproduce exactly the local conditions at the site but to demonstrate the usefulness of a new approach for the numerical description of the various phenomena observed in the field.

A prognosis of the mechanical evolution of the EDZ is only possible if the relevant processes are captured by the used constitutive models. Exemplarily the various characteristics of the EDZ identified around the Mont Terri New Gallery are schematically depicted in Figure 5-1:

- Extension brittle failure: Extension-induced fractures extend to approximately 0.5 m in the sidewalls
- Bedding plane slip is expected in the floor and roof to extend to less than 1 m
- Swelling and softening: change in moisture content can result in significant swelling pressures resulting in time-dependent deformations (this process is not considered in our investigations).

Due to the obviously different influences of matrix and bedding plane properties our modelling strategy consists of two parts, i.e. of a (visco-)elasto-plastic constitutive model, comprising the hardening/softening behaviour and dilatancy effects of the rock mass, and the new shear friction model representing the bedding, as described in detail in chapter 4.3.1.



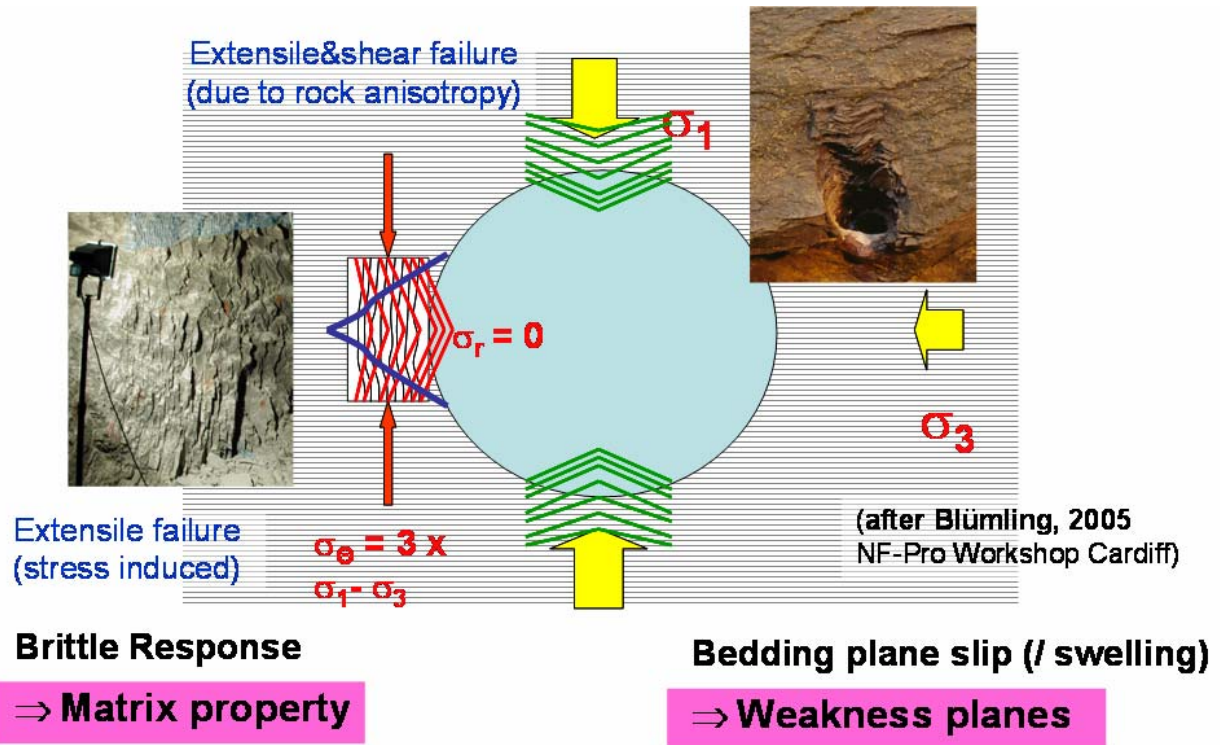
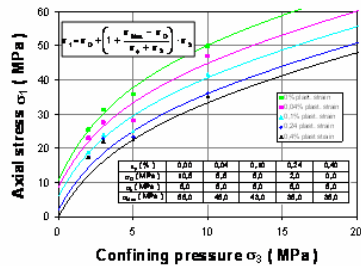


Figure 5-1. Failure mechanism and anisotropy phenomena observed at the Mont Terri site (modified after BLÜMLING, presented during the NF-Pro second training course in Cardiff, 2005)

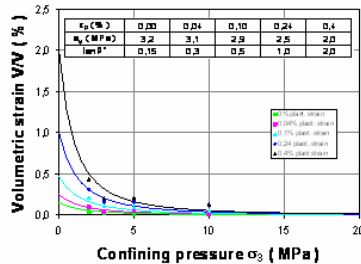
Rock matrix

(Visco)-elasto-plastic model

it describes as a function of elasto/plastic strain :



- hardening
- softening / failure
- dilatancy



Bedding plane properties

Extended Minkley shear model

it describes the behaviour of weakness planes on the basis of:

$$\tau_{adhesion} = \mu_K (1 + \Delta\mu) \cdot \sigma_N + c$$

- μ_K = kinetic friction
- $\Delta\mu$ = adhesive friction
- c = cohesion

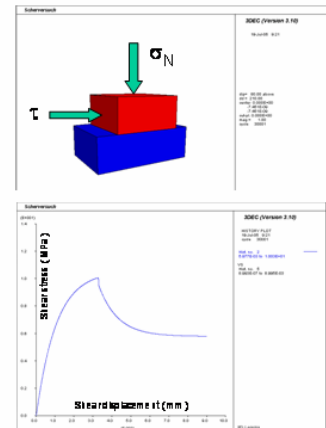
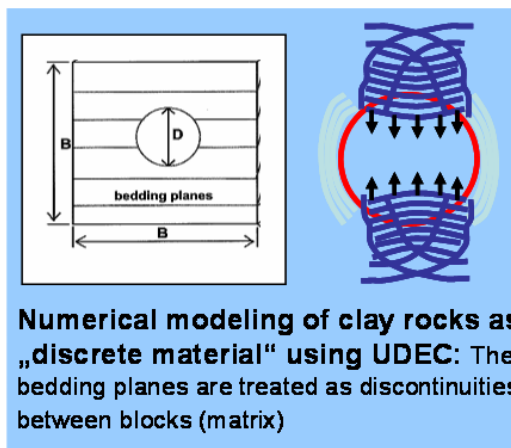


Figure 5-2. The new modelling approach to describe the mechanical evolution of the EDZ based on matrix and bedding plane properties. (centre) the reference case: a specific drift situation at the Mont Terri site with the relevant deformation styles, i.e. extensional failure and bedding plane slip in the roof respectively brittle failure in the wall. (left side) the elasto-plastic constitutive model for the rock matrix (parameter curves of the experimental data); (right side) the new developed shear model for describing bedding plane properties. The inset shows the numerical simulation of a shear test. For details of the used models see MINKLEY & MÜHLBAUER (2007).

[NF-PRO]



In detail, this chapter contains the following subjects:

- Calibration of the constitutive elasto-plastic MINKLEY-law for the Mt. Terri Opalinus clay.
- Modelling of the EDZ due to the tunnel construction in respect to the primary in situ stress field.

5.2 The (visco-)elasto-plastic constitutive MINKLEY-model – derivation of parameters

The constitutive MINKLEY-model has been originally developed for salt rocks (MINKLEY et al., 2001) but is generally useful for all materials which exhibit softening phenomena, as is the case for Opalinus Clay. Softening in this context stands for the decrease of strength of the rock material, when deformation is increasing (strain softening). Under this aspect, in dependence on the rock properties and the loading conditions, different features in their behaviour appear. When an abrupt softening occurs, the phenomenon is called brittle fracture, whereas if gradual softening occurs the material presents yield failure behaviour. So, perfect plastic yield is interpreted as deformation without any softening.

In the physical sense, softening is caused by the generation and accumulation of microcracks and defects within the rock material which progressively develop to macrocracks. During this process, the strength drops to a certain residual level. This residual strength is mainly due to friction processes which run on the formed macroscopic fracture surfaces. Thus, this residual strength is regarded as the lower yield limit of the rock material in the post-failure state.

In the MINKLEY-model, the stress-strain relation is described by two modules consisting of firstly an extended Burgers-model to capture creep phenomena and, in addition of a damage module, which describes the evolution of damage, failure, and the post-failure behaviour by the contribution of the plastic strain ε^p which is modelled on basis of the plastic flow theory.

Thus, the total inelastic strain ε^{inel} consists of the viscous strain ε^v and the plastic strain ε^p :

$$\varepsilon^{inel} = \varepsilon^v + \varepsilon^p \quad (5-1)$$

In our preliminary modelling approach we only focus on the second term of Equation (5-1), that is the plastic strain ε^p which will be illustrated in a very short form based on a comparison of different material laws given by SCHULZE et al. (2007). For the complete description of the model the reader is referred to the extended description given by MINKLEY et al. (2001) respectively by MINKLEY & MÜHLBAUER (2007).

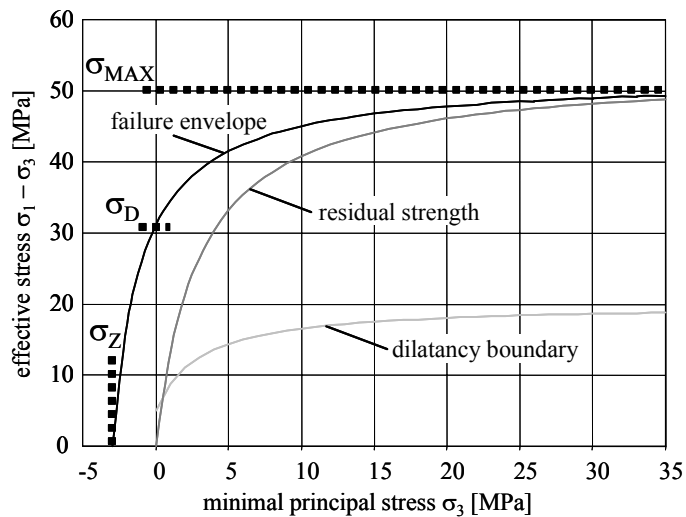


Figure 5-3. Yield points in the visco-elasto-plastic constitutive model.

ε^p results from the sum of strain increments $\Delta\varepsilon^p$ which depend on the evolution of the plastic potential g_s during loading and deformation in the dilatant stress domain and the so-called multiplier λ_s :

$$\Delta\varepsilon^p = \lambda_s \cdot \partial g_s / \partial \sigma \quad (5-2)$$

where the plastic potential g_s is derived from a modified non-linear MOHR-COULOMB criterion representing the stress and strain dependent dilatancy boundary. Of course, equation (5-2) is valid only if the dependence of the plastic strain increments on the plastic potential and the components of the three-dimensional stress field are taken into account.

The multiplier λ_s is a rather complex function. It namely depends on the state of stresses with respect to the strength at failure and the strength at the dilatancy boundary, that is the stress limit for plastic flow. But in the MINKLEY-model the commonly used equation (5-2) is extended, it includes the calculation of the strain hardening in case of a state of stresses beyond the dilatancy boundary and the strain softening if the stress reaches the failure boundary.

In the model, the new deviatoric stress state is computed, assuming stress redistribution by visco-elastic strain increments. If the yield function

$$f_s = \sigma_1 - \sigma_3 + \sigma_D - \frac{\sigma_{MAX} - \sigma_D}{\sigma_\phi - \sigma_3} \cdot \sigma_3 \quad (5-3)$$

results in $f_s < 0$, plastic flow is taking place, and the stresses must be corrected by the impact of an incremental plastic strain before their value is assigned to the new state of stresses. On basis of this procedure, the evolution of the yield function is updated. The hardening or softening lag one time step behind the corresponding plastic deformation. In an explicit code, this error is small, because the steps are small.

In the yield function of equation (5-3) the denoted stresses have the following meaning:

σ_3 = minimum principal stress; σ_1 = maximum principal stress; $\sigma_D(\varepsilon^P)$ = uniaxial strength;
 $\sigma_{MAX}(\varepsilon^P)$ = maximum effective strength; $\sigma_\phi(\varepsilon^P)$ = curvature parameter for strength surface.

For clarification of the function of the respective parameters compare Figure 5-3 where the failure criterion is plotted as $\sigma_1 - \sigma_3 = f(\sigma_3)$.

In case of a continuous, damage affected deformation in the dilatant stress domain, the softening of the strength will converge to the present state of stresses which will lead to the failure and post-failure deformation behaviour, where the flow stress in the post-failure domain is primarily depending on the minimal principle stress.

Again, the elastic modules are expressed in dependence on the damage evolution, i.e. on the progress in the volumetric strain: $K(\varepsilon_{vol}^P)$, $G(\varepsilon_{vol}^P)$, where the volumetric strain ε_{vol} is modelled in dependence on the dilatancy function (which depends on the flow potential g_s) times the plastic flow ε^P .

In summary, using the elasto-plastic constitutive relationship the strength is determined not only at either failure point or at the minimum of the dilatancy curve but also as a set of characteristic strength curves as a function of the plastic deformation ε^P . In an analogue way, the dilatancy behaviour is determined from volumetric deformation values (after first meeting the strength and dilatancy thresholds when $\varepsilon^P = 0$) in discrete deformation steps for $\Delta\varepsilon_1 = 0.1\%$.

After applying the test evaluation procedure on the measured strength and dilatancy data, as depicted in Figure 3-12, a set of curves is obtained corresponding to the dedicated states of plastic deformation. These curves allow a detailed characterization of different deformation states. For the determination of the required parameters, the values of $\tan\beta$ were determined as the slope of dilatancy vs. axial deformation in the dilatancy region and are represented as a function of the confining pressure.

The obtained material parameters of the investigated Opalinus clay are graphically depicted in Figure 5-4 and listed in Table 5-1.

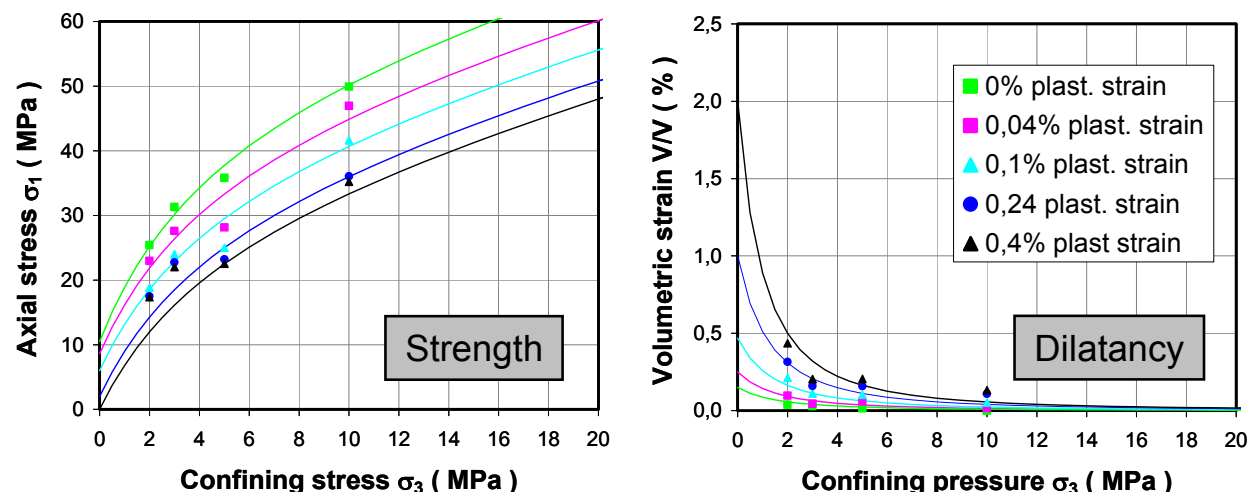


Figure 5-4. Maximum principal strength (left) and volumetric strain (i.e. dilatancy) vs. confining pressure (left) with experimental data and derived modelling curves of the Opalinus Clay.

Table 5-1. Strength (a) and dilatancy parameters (b) as a function of ε_p for the investigated Opalinus clay.

a)

ε_p (%)	0,00	0,04	0,10	0,24	0,40
σ_D (MPa)	10,5	8,6	6,0	2,0	0,0
σ_ϕ (MPa)	5,0	5,0	5,0	5,0	5,0
σ_{Max} (MPa)	55,0	48,0	43,0	38,0	35,0

b)

ε_p (%)	0,00	0,04	0,10	0,24	0,40
σ_w (MPa)	3,2	3,1	2,9	2,5	2,0
$\tan \beta^\circ$	0,15	0,3	0,5	1,0	2,0

5.3 Application

In the actual state the modelling work is still underway; therefore, only preliminary results of 2D-scoping calculations are presented. The calculations are being carried out using the program *UDEC* (i.e. Universal Distinct Element Code of Itasca) in which both above-described constitutive models are available as user-defined models. However, it has to be mentioned that, because the parameter of the new shear-model were not available in the first stage, consideration of the bedding plane properties is only done on the basis of the Mohr-Coulomb criterion.

5.3.1 Model assumptions and parameters

The numerical calculations are oriented on the work performed by BLÜMLING & KONIETZKY (2003). They used a modified MOHR-COULOMB model for numerical predictions with the FLAC code (Itasca) and included multiple couplings:

- Anisotropic Darcy's law for the hydraulic behaviour
- Transversal-isotropic, bi-linear, strain hardening and softening law including a tensile strength cut-off
- Creep law - the modified SALZER creep law which accounts for strain hardening.

Despite the existing model-differences, recalculation of their results for the same random conditions, as schematically depicted in Figure 5-5, offers verification of our model. They report that the maximum convergence detected during excavation was about 25 mm in a horizontal direction and 10 mm in a vertical direction in a tunnel with a diameter of about 3.5 m (overburden 250 - 300 m)

As shown in Figure 5-6, due to geometrical reasons which allow minimizing the calculation time, the 2D-model consists of a half of quadratic cross section perpendicular to a drift with 3.5 m diameter. The model dimensions are:

- height: 30 m
- width: 15 m

[NF-PRO]



Near the tunnel (drift) wall the gridpoint resolution is smallest (0.1 m) at >1.75 m and grows up stepwise from >2.25 m (0.2 m) via >3.25 m (0.4) to >6 m (1 m) until the outer model boundaries.

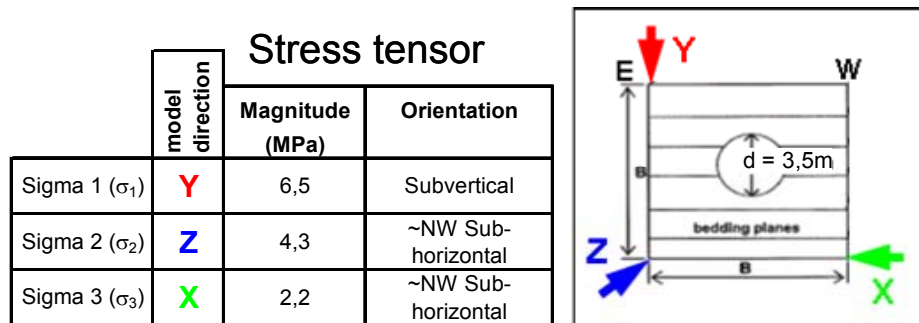


Figure 5-5. Sketch to show the orientation of the bedding planes and the geometrical dimensions (left side) in relation to stress field (right side).

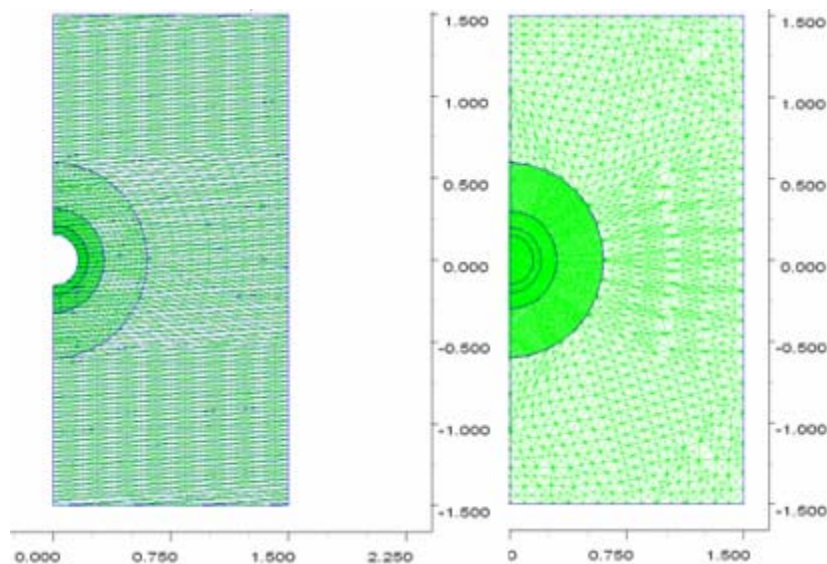


Figure 5-6. Model set up with bedding planes and spatial grid distribution.

Along the left and lower model boundary the normal displacements are fixed to zero. At the upper and right boundary normal stresses according to the virgin stress state including the gravitation induced gradient are applied.

The following parameters were chosen for all model cases:

- Bulk density 2400 kg/m³
- Young's modulus 13200 MPa
- Poisson ratio 0.27
- Tensile strength (rock mass) 1.16 MPa
- Tensile strength (bedding plane) 0.4 MPa
- Stress field see inset Figure 5-5 (right side)

[NF-PRO]

The MOHR-COULOMB-shear parameters used in the preliminary calculations for describing the bedding strength are based on laboratory investigations on the direct shear results as described in chapter 4.2. They are for $c \approx 1$ MPa and for $\varphi \approx 23^\circ$.

The entire clay matrix properties have been modelled using the elasto-plastic constitutive model, as described before. All material parameters are shown in Table 5-1.

5.3.2 Main results from the preliminary model

The calculations were carried out in three steps. First, the 2D-situation around a tunnel drift at the Mont Terri site was calculated only with application of the elasto-plastic approach. Second, the overlapping effect of bedding planes was studied by introducing horizontal oriented bedding planes (dip = 0°), with a vertical distance of 10 respectively 30 cm. Finally, an internal pore fluid pressure was applied.

Figure 5-7 shows the developed damage at the final modelling stage as contour plots of the parameter σ_D , which can be understood as the residual strength at the respective plastic deformation state, and the volumetric strain ε_V , if only the elasto-plastic approach is used. It clearly demonstrates that the development of the plastic regions (EDZ) depends strongly on the relative orientation of the principal stresses and the stress magnitude (mainly the principal stress difference) of the virgin stress field, because only extensional failure is observed at the side walls in the excavation disturbed zone which nicely correspond to the in-situ-stress observations (see Figure 5-5).

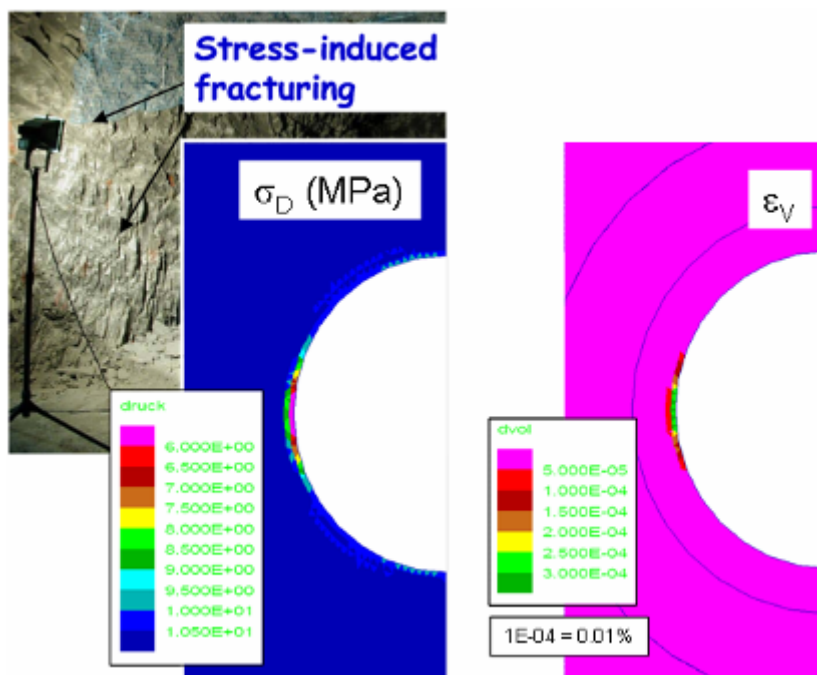


Figure 5-7. Simulation of 2D-situation at the Mont Terri site – elasto-plastic approach. Numerical modelling results, i.e. (left) the development of the damage parameter σ_d and (right) the volumetric strain ε_V . The inset on the left side documents the extensional features as observed in the side walls at Mont Terri (photo taken from BLÜMLING & KONIETZKY, 2003).

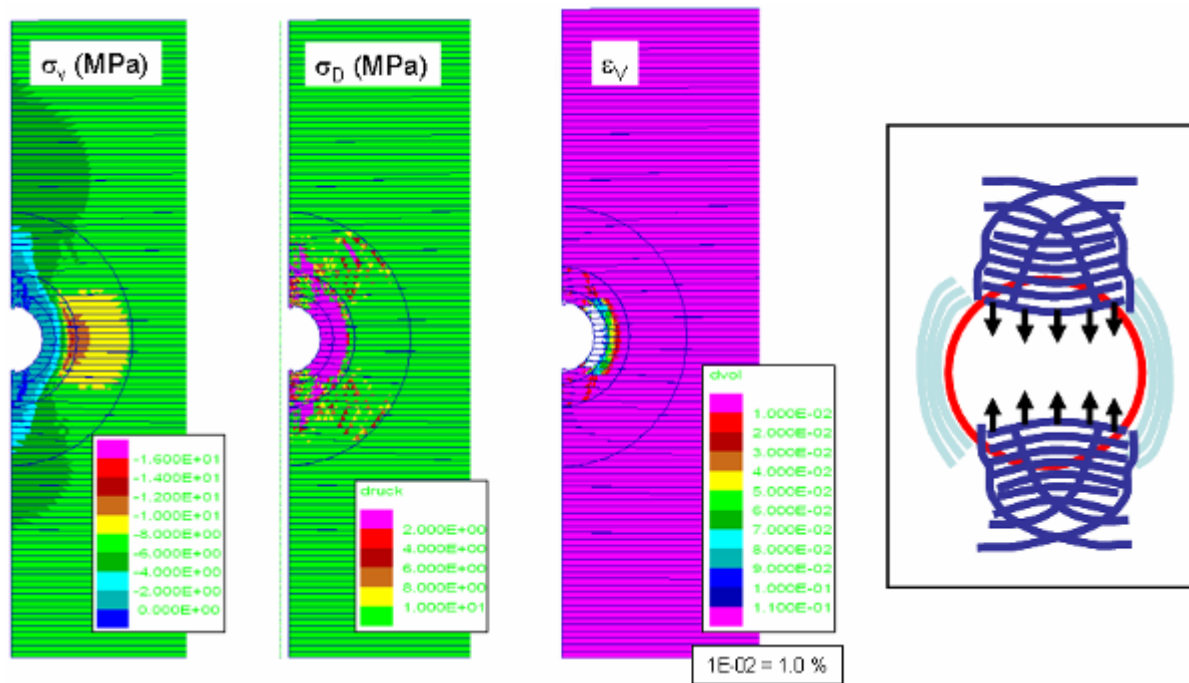


Figure 5-8. Simulation of 2D-situation at the Mont Terri site – combined approach of elasto-plastic description of the rock mass behaviour and simple MOHR-COULOMB-criterion for the reduced shear strength in the bedding – stiffness of bedding planes:1 GPa/m. Numerical modelling results, i.e. (left) Vertical stress distribution; (middle) the development of the damage parameter σ_D and (right) the volumetric strain ε_v . The inset on the right side documents the schematic failure patterns, as deduced from the Mont Terri site.

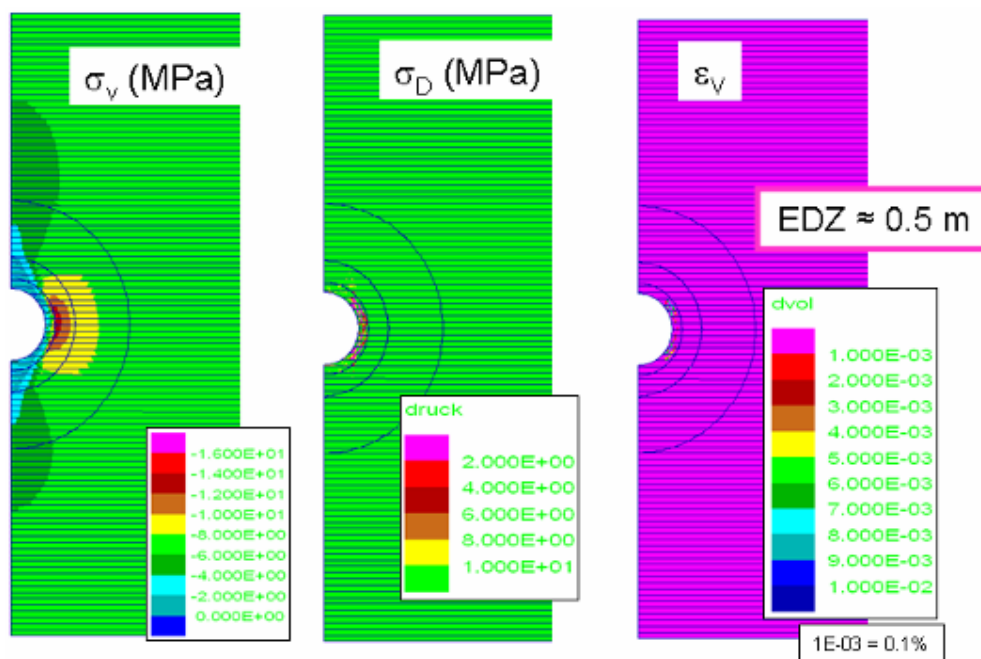


Figure 5-9. Simulation of 2D-situation at the Mont Terri site – combined approach of elasto-plastic description of the rock mass behavior and simple MOHR-COULOMB-criterion for the reduced shear strength in the bedding – stiffness of bedding planes: 1000 GPa/m. Numerical modelling results, i.e. (left) Vertical stress distribution; (middle) the development of the damage parameter σ_D and (right) the volumetric strain ε_v .

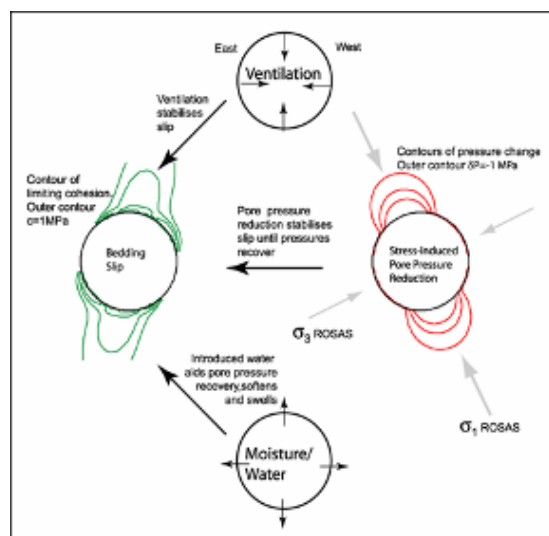
[NF-PRO]

Introducing the effect of bedding planes the results in Figure 5-8 indicate that in addition to the main features of extensional failure in the wall the well known failure patterns in anisotropic rocks, i.e. shear failure in the roof and bottom, are reproduced.

The EDZ in the roof and floor is bounded by bands of enhanced shear deformation (Figure 5-8). Inside the area bounded by these shear zones, mainly tensile failure of the bedding plane is observed. Obviously, the observed failure pattern is caused by the anisotropy of the material parameters rather than the stress field. However, although the deformation features are qualitatively well reproduced by the performed modelling the calculated volumetric strain data are in the order of several percent of dilatancy which seems to be too high, and also the extent of the damage zone is in the order of more than 1.5 m.

Increasing the stiffness of the bedding planes up to 1000 GPa/m drastically reduces the observed shear failure phenomena, but the general failure patterns are preserved with a significantly reduced damage level. Nevertheless, an extent of the EDZ in the order of 0.5m is calculated, which corresponds fairly well with in-situ-observations.

In the last step, a pore pressure of 1 MPa was applied, but the numerical calculations results in total failure of the tunnel which is absolutely unrealistic for the in-situ-situation. As explanation, in UDEC no drainage exists which reduces the pore pressure in the wall during the excavation. Therefore, because $p_p > \sigma_{t\text{-bedding}}$ the loss of cohesion between the bedding planes results in a dramatic failure.



Mont Terri TR 2001-01

- Bedding plane strength depends on the dynamics of excavation
- Pore pressure
 - reduction would result in an increase of effective pressure
 - > **matrix hardening**
 - pore pressures would result in a destabilisation of bedding planes
 - > **HM-coupling not understood**
- Ventilation, which may cause:
 - drying, associated with shrinking
 - > **matrix hardening ↔ reduced stiffness of bedding planes?**
 - wetting, associated with swelling
 - > **matrix softening; partial pore pressure recovery?**

Figure 5-10. Time and humidity dependent processes associated with bedding slip and matrix properties.

5.3.3 Summary

According to BLÜMLING & KONIETZKY (2003) we can conclude that the excavation disturbed zone (EDZ) at the Mont Terri site is mainly influenced by the anisotropy of the rock and the in situ stress field. In the roof and floor, the EDZ is controlled by tensile and shear fractures of

[NF-PRO]

Report – Deliverable 4.2.15

Dissemination level : PU

Date of issue of this report : 01/10/07



the bedding, whereas in the sidewalls there will be predominately tensile fractures through intact rock (Figure 5-8).

However, there remains a lot of uncertainty about not only the general role of humidity but also the role of pore pressures and effective stress, which is not covered by our model, as schematically depicted in Figure 5-10. In addition, time dependent needs to be addressed which is principal possible with the visco-elasto-plastic MINKLEY-law.

6 Summary and Conclusions

Because bedding planes can act as preferential flow paths and mechanical weakness planes, both overlapping effects are particularly important during rock stress redistribution in the EDZ. Focusing on these topics the work is divided in a laboratory part and numerical modelling, based on the obtained experimental results.

The laboratory part comprises conduction and evaluation of deformations tests in a multi-anvil pressure apparatus and in a conventional triaxial cell of the Kármán-type. During the tests relevant information about the stress-dependent development of dilatancy was obtained by measuring the 3-dimensional change of ultrasonic velocities respectively by simultaneous monitoring of V_p , V_s and permeability, in addition to the volumetric strain, representing a wide range of loading conditions. In addition, direct shear tests were performed, which allow quantification of shear strength and dilatancy behaviour of the bedding.

The obtained results cover a wide range of applied normal stresses and displacement rates and delivered a reliable estimate of shear properties (i.e. strength and dilatancy angle) which is an important base of latter rock mechanical modelling.

Finally, with respect of a prognosis of the EDZ a new modelling approach has been developed based on the separate constitutive description of matrix and bedding plane properties. Using UDEC and under application of the site-specific material parameters, the relevant EDZ phenomena for a local drift situation in the Mont Terri lab (e.g. tensile fractures at the wall respectively shear slip and tensile fractures in the roof, could be nicely simulated. Also the spatial extent of the EDZ corresponds fairly well to the in-situ observations.

According to the outline of our study the main results are summarized in three sections.

6.1 Initial sample state and transport properties

Regarding the initial sample state, both, seismic monitoring and permeability measurements clearly indicate pre-damage of the investigated core samples, and, in addition, only partial saturation due to sample disturbances during sample recovery and preparation whereby the relation to the bedding is apparent.

Increase of confining stress contributes largely to compaction whereby sealing is most efficient perpendicular to the bedding.

- Gas transport in Opalinus clay is affected by 2-phase flow processes:

[NF-PRO]

Report – Deliverable 4.2.15

Dissemination level : PU

Date of issue of this report : 01/10/07



- Discontinuous gas transport
- The capillary gas threshold pressure is a function of permeability.

Deviatoric loading is initially accompanied by a permeability decrease up to 80 - 90% of the failure stress. Only if localized shear failure takes place a pressure dependent permeability increase is observed. Therefore, a simple coupling between mechanical (i.e. damage) and hydraulic properties seems to be unlikely.

6.2 Deformation behaviour and dilatancy boundary concept:

The strength behaviour is strongly anisotropic and depends on:

- Orientation to the bedding: bedding = weakness plane
- Minimal stress: With increasing σ_{\min} the rock strength non-linear increases, whereby $\sigma_{\text{failure}} // \text{ss} > \sigma_{\text{failure}} \perp \text{ss}$. It has to be mentioned that the reverse is true under uniaxial stress.

It has been convincible shown, that detection of „dilatancy“ depends on the sensitivity of the measured physical parameter and the measuring direction:

- Although no macroscopic dilatancy is measured micocracking occurs, as indicated by the reversal of Vs. This inconsistency is simply explained by the overlaying effect of weak matrix compaction. At higher stresses a transitional range exists where also macroscopically damage occurs resulting in development of measurable dilatancy:

- $\sigma_{\text{initial-damage}} \approx 0.5 - 0.6 * \sigma_{\text{peak}}$ (ultrasonic monitoring)
- $\sigma_{\text{dilatancy}} \approx 0.8 - 0.9 * \sigma_{\text{peak}}$ (Opalinus Clay, BLÜMLING 2005)

Therefore, the reliability of the term „dilatancy“ regarding its importance for the EDZ in indurated clays should be discussed. However, the dilatancy concept seems to be valid also in clay rocks, but due to the rock anisotropy it's application is much more difficult.

6.3 Modelling of failure modes and EDZ-structures:

As well known by the long-lasting work on argillaceous clays and as confirmed by our work the general failure mechanisms during excavating underground openings in indurated clays are:

- brittle fracturing - caused by the high deviatoric stresses;
- bedding slip caused by the anisotropic stresses and strength;
- structurally controlled failure on bedding planes;
- strength loss through hydration (i.e. humidity induced softening), but strengthening is attributed to drying (not considered in the modelling)

Focusing on the two overlapping effects of rock mass and bedding behaviour the new developed modelling approach consists of two parts:

- a (visco-)elasto-plastic constitutive model comprising the hardening/softening behaviour and dilatancy effects of the rock mass and

- a specific shear friction model, which describes displacement- and velocity-dependent shear strength softening for the bedding planes.

Based on the experimental data the necessary parameter sets of the different constitutive models were derived.

The 2D-simulation of the EDZ around a tunnel under the site specific conditions of the Mont Terri Site demonstrated the capability of the new approach. As came out by the modelling results, the geometry of the EDZ during excavation is mainly controlled by the instantaneous reaction of the rock mass on the anisotropic stress regime (elasto-plastic behaviour \Rightarrow stress induced tensile failures at the wall) and by the overlapping bedding plane weakness (\Rightarrow tensile and shear fractures).

So far, we can conclude that high sophisticated rock-mechanical constitutive models are available to model the development of the EDZ from a mechanical point of view. But looking on the real in-situ-conditions it becomes obvious that more understanding of the complex effects of humidity and pore pressures is required for their numerical implementation into the existing constitutive models. Nevertheless consideration of the time-dependent effect, i.e. creep, can be easily done by determining the necessary parameters for the viscous part of the MINKLEY-law. But from our feeling it remains questionable if the observed time dependent convergence behaviour is real creep? As recommendation for future work we have to conclude that more experimental lab and field investigation are necessary to describe the complex THMC-behaviour of argillaceous clays.

Literature

- Birch, F., 1960. The velocities of compressional waves up to 10 kbars, Part 1, J. Geophys. Res., 65, 1083-1102.
- BOCK, H., 2001. RA-Experiment Rock Mechanics Analysis and Synthesis: Conceptual Model of Opalinus Clay, TR 2001-3, Mont Terri Project.
- BLUEMEL, M., POETSCH, M., 2003. Direct shear testing system. International Symposium on GeoTechnical Measurements and Modelling, Karlsruhe, 327 – 331.
- BLÜMLING, P. & KONIETZKY, H. (2003) Development of an excavation disturbed zone in claystone (Opalinus Clay). Geotechnical measurements and modelling: Proceedings of the international symposium, 23-25 September 2003, Karlsruhe, Germany; Natau O., Fecker, E., Pimentel E. (eds.); Lisse [et al.]: A.A.Balkema Publishers, 127-132.
- BRAUN, G., 1994. Multi-channel X-ray measurements of textures with a standard texture goniometer. In: H.J. BUNGE, S. SIEGSMUND, W. SKROTZKI and K. WEBER, Textures of geological materials. DGM Informationsgesellschaft. 61-82.
- CRISTESCU, N., & U. HUNSCHKE, 1998. Time Effects in Rock Mechanics, John Wiley, New York.
- CUNDALL, P.A. & LEMOS, J.V. (1990): Numerical simulation of fault instabilities with a continuously-yield joint model. In C. Fairhurst (ed.), Proc. 2nd Int. Symp. on Rockbursts and Seismicity in Mines, Minneapolis, 8-10 June 1990: 147-152. Rotterdam: Balkema.
- HUNSCHKE, U, WALTER, F., SCHNIER, H., 2004. Evolution and failure of the Opalinus Clay: relationship between deformation and damage, experimental results and constitutive equation. Applied Clay Science, 26, 403-411.
- HILDENBRAND, A., 2003. Fluid Transport Process in Mudstones. PhD TH Aachen, ISBN: 3-86130-087-7.
- IFG, 2005a. Influence of Bedding Planes. State of the Art Report / Test plan (D4.2.2.). NF-PRO RTD4, WP 4.2 (EDZ Initial phase characterization and modelling). Institut für Gebirgsmechanik GmbH, Leipzig, January 15, 2005. 40 pp.
- IFG, 2005b. Influence of Bedding Planes. 1. Report: Triaxial deformation tests in a multi-anvil apparatus with ultrasonic monitoring. 2. Milestones: Sampling and rock preparation; adaptation of laboratory techniques (D4.2.6). NF-PRO RTD4, WP 4.2 (EDZ Initial phase characterization and modelling). Institut für Gebirgsmechanik GmbH, Leipzig, January 15, 2005. 34 pp..
- IFG, 2006. Influence of Bedding Planes. 1. Report: Triaxial deformation tests in a multi-anvil apparatus with ultrasonic monitoring. 2. Milestones: Sampling and rock preparation; adaptation of laboratory techniques

[NF-PRO]

Report – Deliverable 4.2.15

Dissemination level : PU

Date of issue of this report : 01/10/07



- (D4.2.8). NF-PRO RTD4, WP 4.2 (EDZ Initial phase characterization and modelling). Institut für Gebirgsmechanik GmbH, Leipzig, February 10, 2006. 39 pp. (2006-02-10).
- KÁRMÁN, Th. v., 1911. Festigkeitsversuche unter allseitigem Druck, Ztschr. Vereines Deutscher Ingen., 55, 1749 – 1757.
- KERN, H., 1982. P and S wave velocities in crustal and mantle rocks under the simultaneous action of high confining pressure and high temperature and the effect of the rock microstructure, in "High Pressure Researches in Geoscience", edited by W. Schreyer, pp. 15-45, Schweizerbart, Stuttgart, Germany.
- KERN, H., LIU, B. & POPP, T., 1997. Relationship between anisotropy of P and S wave velocities and anisotropy of attenuation in serpentinite and amphibolite. *J. Geophys. Res.*, 102, 3051 - 3065.
- KERN, H. & POPP, T., 2001. Messung und Beschreibung der zeitlichen Entwicklung von Porosität und Permeabilität von Salzgestein aus dem Salzstock Gorleben. Abschlußber. zum Forschungsauftrag 2-803 286, 117 S.
- LUX, K.-H., Czaikowski, O., Düsterloh, U., Hou, Z., 2004. Report on short-term laboratory tests on indurated clay to determine short-term strength, damage boundary and healing boundary. NF-Pro RTDC4, WP 4.4: EDZ long term evolution, Technical University Clausthal.
- MARSCHALL, P., HORSEMAN, S. & T. GIMMI, 2005. Characterisation of Gas Transport Properties of the Opalinus Clay, a Potential Host Rock Formation for Radioactive Waste Disposal. *Oil & Gas Science and Technology – Rev. IFP*, Vol. 60, No. 1, pp. 121-139.
- MARTIN C.D., LANYON G.W., BLÜMLING P., and MAYOR J.C., 2003. The excavation disturbed zone around a test tunnel in the Opalinus Clay. In: *Impact of Excavation Disturbed or Damaged Zone (EDZ) on the Performance of Radioactive Waste Geological Repositories*. Proceedings of a European Commission CLUSTER Conference, Luxembourg, November 3–5, 2003.
- MINKLEY, W., MENZEL, W., KONIETZKY, H & te KAMP, L., 2001. A visco-elasto-plastic softening model and its application for solving static and dynamic stability problems in potash mining. In Billaux et al. (eds.), *FLAC and Numerical Modelling in Geomechanics; Proc 2. Inter. FLAC-Symp.*, Napoli, 29-31 Oct. 2001. Rotterdam: Balkema, 21-27.
- MINKLEY, W. & MÜHLBAUER, J., 2007. Constitutive models to describe the mechanical behaviour of salt rocks and the imbedded weakness planes. In *Proc. 6th Conference on the Mechanical Behaviour of Salt*, Hannover, 22-25 May 2007, Rotterdam: Balkema, 119-127.
- MONT TERRI PROJECT, 2004. Work Programme, Phase 10. 15 October 2004.
- O'BRIEN, N. R. & SLATT, R. M., 1990. *Argillaceous rock atlas*. – 141 p., New York (Springer).
- PEACH, C. J., & C.J. Spiers, Influence of crystal plastic deformation on dilatancy and permeability development in synthetic salt rock, *Tectonophysics*, 256, 101-128, 1996.
- POPP, T. & KERN, H., 2000. Monitoring the state of microfracturing in rock salt during deformation by combined measurements of permeability and P-and S-wave velocities *J. Phys. Chem. Earth*, Vol. 25, Part A, No.2., 149 - 154.
- POPP, T., KERN, H. & O. SCHULZE, 2001. The evolution of dilatancy and permeability in rock salt during hydrostatic compaction and triaxial deformation.- *J. Geophys. Res.* 106 , No. B3, 4061-4078.
- SCHULZE, O. & POPP, T., 2002. Untersuchungen zum Dilatanzkriterium und zum Laugendruckkriterium für die Beurteilung der Integrität eines Endlagerbergwerkes in einer Steinsalzformation. *Z. angew. Geol.*, 2/2002, 16 – 22.
- SCHULZE, O., POPP, T. & KERN, H., 2001. Development of damage and permeability in rock salt undergoing deformation. In: *Proceedings of the EUG 10 - Conference*, 28th March - 1st April 1999, Strasbourg, France, Symposium J3 - Radioactive Waste Disposal, M. Langer et al. (Eds.). - *Engineering Geology*, 61, 163-180.
- SCHULZE, O., HEEMANN, U., ZETSCHKE, F., HAMPPEL, A., PUDEWILLS, A., GÜNTHER, R.-M., MINKLEY, W., SALZER, K., HOU, Z., WOLTERS, R., ROKAHR, R. & D. ZAPF., 2007. Comparison of advanced constitutive models for the mechanical behaviour of rock salt - results from a joint research project – I. Modelling of deformation processes and benchmark calculations. In *Proc. 6th Conference on the Mechanical Behaviour of Salt*, Hannover, 22-25 May 2007, Rotterdam: Balkema, 77-88.
- VALES, F., NGUYEN MINH, D., GHARBI, H. & REJEB, A., 2004. Experimental study of the influence of the degree of saturation on physical and mechanical properties in Tournemire shale (France), *Applied Clay Science*, 26, 197 – 207.
- WANG, J.A. & PARK, H.D., 2002. Fluid permeability of sedimentary rocks in a complete stress-strain process. *Engineering Geology*, 63, 291 -300.
- WASHBURN, E.W., 1921: Note on a method of determining the distribution of pore sizes in a porous material, *Proceedings of the National Academy of Science*, 115-116. *Bulletin*, 63, 723-760.
- ZHANG, C.-L. & ROTHFUCHS, T., 2005. Determination of material parameters for the Opalinus Clay. NF-Pro RTDC4 – WP 4.3: EDZ long term evolution. Deliverable 4.3.4. GRS Braunschweig.

